THE DEVELOPMENT AND CHARACTERIZATION OF STIMULI-RESPONSIVE SYSTEMS FOR PERFORMANCE MATERIALS

by

Melissa B. Gordon

A dissertation submitted to the Faculty of the University of Delaware in partial fulfillment of the requirements for the degree of Doctor of Philosophy in Chemical Engineering

Winter 2017

THE DEVELOPMENT AND CHARACTERIZATION OF STIMULI-RESPONSIVE SYSTEMS FOR PERFORMANCE MATERIALS

by

Melissa B. Gordon

Approved: _____

Abraham M. Lenhoff, Ph.D.
Chair of the Department of Chemical and Biomolecular Engineering

Approved: _____

Babatunde A. Ogunnaike, Ph.D.
Dean of the College of Engineering

Approved: _____

Ann L. Ardis, Ph.D.
Senior Vice Provost for Graduate and Professional Education

I certify that I have read this dissertation and that in my opinion it meets the academic and professional standard required by the University as a dissertation for the degree of Doctor of Philosophy.

Signed: _____

Norman J. Wagner, Ph.D.
Professor in charge of dissertation

I certify that I have read this dissertation and that in my opinion it meets the academic and professional standard required by the University as a dissertation for the degree of Doctor of Philosophy.

Signed: _____

Christopher J. Kloxin, Ph.D.
Professor in charge of dissertation

I certify that I have read this dissertation and that in my opinion it meets the academic and professional standard required by the University as a dissertation for the degree of Doctor of Philosophy.

Signed: _____

April M. Kloxin, Ph.D.
Member of dissertation committee

I certify that I have read this dissertation and that in my opinion it meets the academic and professional standard required by the University as a dissertation for the degree of Doctor of Philosophy.

Signed: _____

Michael E. Mackay, Ph.D.
Member of dissertation committee

I certify that I have read this dissertation and that in my opinion it meets the academic and professional standard required by the University as a dissertation for the degree of Doctor of Philosophy.

Signed: _____

Debora F. Massouda, Ph.D.
Member of dissertation committee

ACKNOWLEDGMENTS

I am very thankful for all of the support and guidance that I received during my PhD. Most importantly, I would like to thank my advisors, Dr. Christopher Kloxin and Dr. Norman Wagner, for being great role models to me and for always telling me it was going to be okay even when I did not believe them. I am especially appreciative of their kindness, support, advice and willingness to share their knowledge with me. Over the past four years, I have learned a tremendous amount from them, and I am forever grateful.

I was very fortunate to work with helpful and supportive labmates who became my good friends. I would like to thank Stephen Ma, Kaleigh Reno, Bassil El-Zaatari, Abhishek Shete, Andrew Tibbits, Ben Carberry, Justin Paloni, Laura Mumper, Shea Cole, Tom Cristiani and Bryan Sutherland for all of their assistance, kindness and support over the last four years. Moreover, I want to especially thank Dr. Jonathan French for always believing in me. He assisted me with a lot of the chemistry techniques contained in the thesis and I am tremendously grateful for all of his professional and personal advice, both when he was at Delaware and years later. I would also like to thank three undergraduate students, Samantha Mannino, Jonathan Galarraga and Grant Knappe, who helped with a lot of the work in this thesis and made working in lab a lot more enjoyable for me. Additionally, I am grateful to everyone in the Wagner group for their assistance throughout the years, especially Ryan Murphy, Kevin Whitcomb, Michelle Calabrese, Ru Chen, Simon Rogers, Jingsi Gao, Jannat Nayem, Julie Hipp and Jeff Richards. Moreover, I would like to acknowledge Dr. Steve Bai for his help with

NMR experiments as well as Dr. Yun Liu and Dr. Paul Butler for their assistance with the Rheo-SANS experiments. I am also grateful for the assistance of Dr. Shu Wang and Dr. Thomas Epps on the mechanochemistry project. I would also like to thank my committee members, Dr. April Kloxin, Dr. Debora Massouda and Dr. Michael Mackay, for their suggestions and Kathie Young for all of her help.

I am forever grateful to my professors at Lafayette College and, especially to my undergraduate advisor, Dr. James Ferri, for convincing me to switch my major to chemical engineering during my freshman year of college and for being a constant source of guidance and support throughout my undergraduate and graduate education.

Last, but not least, I would like to thank my parents, grandmother, Sarah and Robert for their support and love.

TABLE OF CONTENTS

LIST OF TABLES

LIST OF FIGURES

ABSTRACT

In nature, living organisms adjust to their surroundings by responding to environmental cues, such as light, temperature or force. Stimuli-triggered processes, such as the contraction of eyes in response to bright light or wound healing in skin after a cut, motivate the design of "smart" materials which are designed to respond to environmental stimuli. Responsive materials are used as self-healing materials, shape memory polymers and responsive coatings; moreover, responsive materials may also be employed as model systems, which enhance understanding of complex behavior.

The overall goal of this work is to design a material that offers self-healing functionality, which will allow for self-repair following material fatigue or failure, and increased strength in response to ballistic or puncture threats through the incorporation of colloidal particles. The target application for this material is as a protective barrier in extreme environments, such as outer space. Towards this end, the dissertation is focused on the development and characterization of each component of the protective material by (1) designing and testing novel light- and force-sensitive polymers for self-healing applications and (2) examining and characterizing long-time behavior (i.e., aging) in model thermoreversible colloidal gels and glasses.

Towards the development of novel stimuli-responsive materials, a photo-responsive polymer network is developed in which a dynamic bond is incorporated into the network architecture to enable a light-triggered, secondary polymerization, which increases the modulus by two orders of magnitude while strengthening the network by over 100%. Unlike traditional two-stage polymerization systems, in which the

secondary polymerization is triggered by a leachable photoinitiator, the dynamic nature is imparted by the material itself via the dissociation of its own crosslinks to become stronger in response to light. Several attributes of the photo-responsive network are shown including: (1) photo-induced healing and strengthening of a specimen after it has been severed, (2) photopatterning for effecting spatially confined property changes on demand, and (3) locking in the film's 3D geometry using light after reshaping. The utility of the photo-responsive dynamic bond is enhanced by demonstrating that it is also responsive to mechanical force. Force-responsive materials are activated by the energy from the damage event itself, thereby enabling healing without human intervention. Specifically, selective cleavage of a polymer containing a dynamic trithiocarbonate group initiates a force-driven radical polymerization, thus enabling the material to constructively respond to force via gelation on an experimentally relevant timescale.

To enhance the stress response of the self-healing materials described above, a protective material composed of colloidal particles is proposed. Toward this goal, the second half of this dissertation investigates the microstructural basis of rheological aging in colloidal gels and glasses using a model thermoreversible colloidal dispersion. In this work, rheological aging is quantitatively related to microstructural aging in glasses and gels by simultaneously measuring the bulk properties and sample microstructure using rheometry and small angle neutron scattering (Rheo-SANS), respectively. A one-to-one correspondence between the evolution in storage modulus and microstructure as the sample ages is observed, which is investigated as a function of thermal and shear history. The microstructural measurements are consistent with the hypothesis of aging as a trajectory in a free energy landscape, which combined with

analysis with mode coupling theory, support local particle rearrangements as the mechanism of aging. Moreover, by using a system that is fully rejuvenated by thermal cycling, the effectiveness of shear as a rejuvenation method is investigated by directly comparing microstructure and bulk properties following thermal and mechanical rejuvenation. The conclusions of this study may be industrially relevant to products that age on commercial timescales, such as pharmaceuticals, applicable to other dynamically arrested systems, such as metallic glasses, and provide pathways to advanced composite materials such as those envisioned in this work.

Chapter 1

INTRODUCTION

The overall goal of this work is to design an advanced material that offers self-healing functionality, which will allow for self-repair following material fatigue or failure, and increased strength in response to ballistic or puncture threats through the incorporation of colloidal particles. The envisioned material is lightweight and flexible, yet provides enhanced durability and increased strength in response to damage. The target application for this material is as a protective barrier in extreme environments, such as outer space, where material integrity translates into survival or death. Towards this end, the dissertation is focused on the development and characterization of each component of the protective material by (1) designing and testing novel light- and force-sensitive polymers for self-healing applications and (2) examining and characterizing long-time behavior (i.e., aging) in model thermoreversible colloidal gels and glasses. The development of such a protective material has tremendous potential to improve material safety and reliability.

1.1 Motivation for Healing Materials

Much of the work contained in this dissertation is inspired by nature. Living organisms display a variety of incredible responses to environmental stimuli, such as the contraction of pupils in response to bright light, wound healing of skin after a cut or camouflaging when threatened. Unlike biological systems, most synthetic materials are incapable of constructively responding to environmental stimuli. These examples from

nature motivate the design of stimuli-responsive materials, which are capable of responding to environmental cues by altering their properties to meet the demands of a changing environment.

Stimuli-responsive materials are designed to respond to one or more external triggers, such as light, temperature, force or pH, which initiate a chemical or conformational change in the material [1]. Responsive materials are used as shape memory polymers, responsive coatings, and puncture-resistant protective garments as well as in self-healing and controlled drug delivery applications. Due to the wide and far-reaching impact of stimuli-responsive materials, there has been increasing interest in this area and a ten-fold increase in publications within the last decade [2].

In particular, self-healing materials have the capacity to recover their functionality after damage, reducing waste and improving the environmental sustainability of the material [3]. For these reasons, self-healing materials were first proposed three decades ago and have remained a significant research target for investigation [4]. Generally, self-healing materials can be divided into two main groups based on the healing strategy employed: (1) structural (e.g., capsule-based or vascular), and (2) intrinsic. Within these categories, each particular approach has distinct advantages and disadvantages with respect to healing efficacy, time, and 'healing' repeatability [5].

1.2 Structural-based Healing

Structural self-healing schemes involve composite material systems composed of separate components, which subsequently react when combined as a result of damage, constituting a 'healing' response. An early approach in 2001 involved a microencapsulated healing agent (monomer) that was embedded in an epoxy matrix

containing an initiator. Once the microcapsules ruptured due to material damage, the monomer would be exposed to the initiator, triggering a 'healing' polymerization reaction [6]. Unfortunately, capsule-based structural healing schemes are typically limited by the catalyst shelf-life and are susceptible to multiple damage events (i.e., a ruptured capsule cannot undergo a second healing event). Further, these capsules are defects, which add bulk and weight to the material while reducing its strength. Biologically-inspired structural self-healing schemes based on vascular architectures have also been reported. These vascular systems are composed of channels through which healing agent (monomer) flows until a rupture event (material failure) activates the release of healing agent that triggers healing. One of the most important developments in this area involves construction of a three-dimensional microvascular network capable of undergoing repeat healing events [7]. This strategy has similar disadvantages as the previous approach; additionally, the healed region remains a vulnerable area in the material.

1.3 Intrinsic Healing via Dynamic Covalent Bonds

In contrast to the structural approaches discussed above, intrinsic healing leverages the inherent ability of the material to repair itself. To develop responsive materials, dynamic bonds are built into the network architecture, which undergo bond rearrangements that impart desirable macroscopic properties such as the ability to relieve stress, reconfigure, reshape and heal [8, 9]. Often, these molecular rearrangements are activated by an external stimulus such as light or heat. The properties of the resultant network are highly dependent on the particular dynamic linkages used and the network topology. A summary of the dynamic linkages discussed in this chapter is shown in Figure 1.1.

Network rearrangement is dependent on the type of dynamic crosslink, which is categorized as either reversible exchange reactions or reversible addition reactions [8]. These two types of dynamic crosslinks differ in the mechanism of molecular rearrangement—reversible exchange reactions maintain the connectivity of the network while reversible addition reactions temporarily disrupt the connectivity. One well-studied example of reversible exchange reactions is the transesterification reaction (Figure 1.1), which was successfully implemented into a covalent polymer network by Montarnal and coworkers in 2011 to impart self-healing functionality [10]. Another approach towards imparting dynamic nature to polymer networks utilizes cycloaddition reactions, such as the [2+4] cycloaddition or Diels-Alder reaction, which is a widely-used type of reversible addition reaction (Figure 1.1). For example, in 2002, Chen et al. reported utilizing the Diels-Alder reaction to create a crosslinked polymer network, which reformed after fracture via the retro Diels-Alder reaction at 120-150°C [11]. The authors report an average mending efficiency of 50% at 150°C and 41% at 120°C.

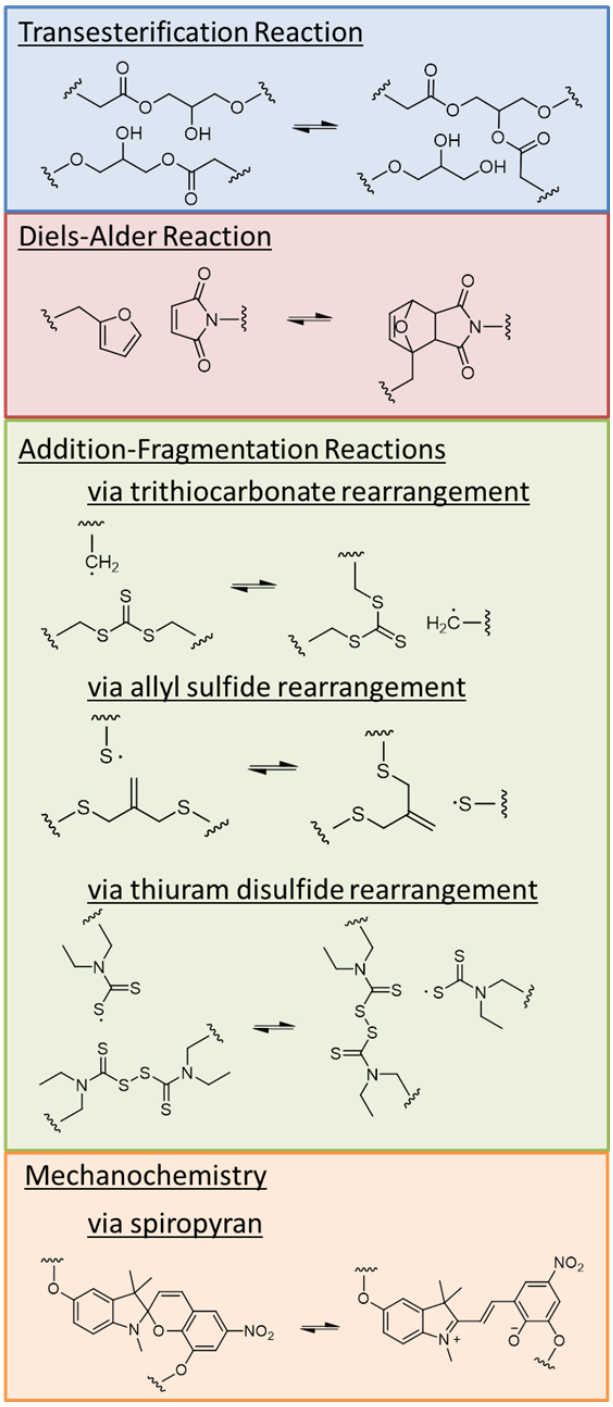

Figure 1.1: Summary of dynamic chemistries discussed in the introductory chapter.

While the aforementioned studies applied heat to initiate network rearrangement and healing, light has also been used to effectively trigger network reorganization. The advantages of using light as a stimulus include simplicity, low-cost and spatiotemporal control of the healing reaction [12]. Several research groups have successfully employed reversible photo-crosslinking reactions for macroscopic self-healing by utilizing photoreactive moieties such as cinnamoyl and coumarin, which are capable of undergoing reversible dimerization via cycloaddition and dissociation under different wavelengths of UV light [13, 14]. When damage occurs, the cyclic ring is preferentially cleaved due to its low bond strength and irradiation heals the network via a cycloaddition reaction. Alternatively, light can generate radicals in polymer systems that contain dynamic covalent bonds in which damage is repaired through recombination and rearrangement, provided that there is sufficient chain mobility in the network [12]. One approach towards developing dynamic networks of this type involves incorporating reversible-addition chain transfer (RAFT) units into the network backbone. For instance, in 2011, Amamoto and coworkers introduced trithiocarbonate units (Figure 1.1) into a covalently crosslinked polymer system and demonstrated repeatable photo-triggered healing via the reshuffling of the trithiocarbonate groups under light [15]. This approach required the healing to be conducted under a nitrogen atmosphere to avoid the quenching of the carbon radical intermediates. A year later, the same group reported healing in air by utilizing a different chemical moiety. In particular, they demonstrated a self-healing scheme based on the reversible dissociation of chemical bonds in thiuram disulfide (Figure 1.1) under visible light in air and at room temperature [16]. Another approach towards developing radical-based dynamic networks was introduced in 2005 by Scott and coworkers [17]. In this system, the

dynamic nature is imparted by an allyl sulfide group (Figure 1.1), which is incorporated into a rubbery thiol-ene polymer network to impart photo-activated stress relaxation and plasticity. Further, Kloxin et al. demonstrated mechanophotopatterning of a thiol-ene elastomer containing allyl sulfide groups to enable changes in the network shape and surface topography post-cure [18].

Importantly, not all intrinsic healing schemes rely on heat or light to activate the healing response. An alternative approach utilizes mechanochemical reactions, which comprise a class of reactions that are triggered by a mechanical deformation, which subsequently initiates the healing response [19, 20]. In addition to its use in self-healing schemes, mechanical energy has been shown to bias reaction pathways to produce products not attainable using light or heat through incorporation of mechanically-sensitive groups called mechanophores [21]. Some mechanically-sensitive groups, such as spiropyran (Figure 1.1), change color when force is applied, which allowed the mechanochemistry to be studied directly [22]. Recently, it has been shown that when stress is applied to a mechanophore in a polymer chain, self-strengthening occurred via nucleophilic displacement reactions [23]. Some mechanically-active systems have also been shown to photo-heal. Urban and coworkers developed a system based on colorless spironaphthoxazine which ring-opens to its red, merocyanine form when force is applied [24]. After application of light or heat, the damaged sample returned to its colorless form with a modulus similar to that of the original material. This approach, in conjunction the methods outlined in this section, demonstrates the successful implementation of force-responsive and photo-responsive chemistries into polymer networks to trigger macroscopic healing.

1.4 Motivation for Studying Colloidal Suspensions

Colloidal dispersions are found in a wide variety of consumer products such as paints, foods and pharmaceuticals. Despite their extensive use, the behavior of these systems is often highly complex and further study of colloidal dispersions is vital to optimize processing conditions as well as to determine and predict stability and shelf-life, which enhances product efficacy and safety. Furthermore, colloidal particles can be used to further the understanding of other systems. Specifically, due to their larger size scale, which allows for direct measurement of bulk properties, and tunable interactions, colloids can be used to study atomic and molecular systems [25, 26]. For example, Nobel Laureate Jean Perrin calculated Avogadro's number from measurements of the motion of a colloidal particle to prove the atomic theory of matter. Most importantly, colloidal particles may also be added to polymer networks, resulting in composite materials with enhanced strength and reduced cost. Further, some colloidal systems have been shown to offer superior protection to stab and puncture threats, and such functionality will be incorporated in the material envisioned in this work. Thus, the study of colloidal suspensions can further the understanding of complex condensed matter systems and aid in the design of new materials.

1.5 Colloidal Systems with Attractive Interactions

Many consumer products and naturally-occurring systems, including certain paints and blood, aggregate due to attractive interactions between the colloidal particles. The attractive interaction can be represented mathematically by the square-well potential, which consists of a hard sphere potential (in which there is no interaction between the particles until they come into contact with each other at which point the potential becomes completely repulsive) with an attractive well as shown in equation 1:

$$\phi^{sq}(r) = \begin{cases} \infty & 0 < r < 2a \\ -\epsilon & 2a < r < 2(a+\Delta) \\ 0 & r > 2(a+\Delta) \end{cases} \quad (1)$$

where a is the particle radius and the attractive well has a well depth ε and well width 2Δ. The square well potential simplifies to the sticky hard sphere potential in the limit that Δ becomes infinitesimally thin, which is typically used to quantify the interactions between particles with short-ranged attractions called "sticky" spheres or adhesive spheres. The sticky hard sphere model (or Baxter model) is characterized by the Baxter parameter, τ_B, which quantifies the strength of attraction between particles. The Baxter parameter can be calculated using parameters from the square-well potential as follows:

$$\tau_B{}^{-1} = 4\left(e^{\frac{\epsilon}{k_B T}} - 1\right)\left[\left(\frac{a+\Delta}{a}\right)^3 - 1\right] \quad (2)$$

Moreover, as the Baxter parameter quantifies the strength of interaction, it can be used to generate a phase diagram [27]. In this representation, the Baxter parameter represents an effective temperature, which is used to delineate phase behavior as a function of volume fraction, as shown in Figure 1.2. In the limit as the Baxter parameter approaches infinity, the hard sphere potential is recovered. Note that as the Baxter parameter decreases, the strength of interaction increases as the suspension transitions from a liquid to a gel or glass. These results were obtained using a model colloidal suspension consisting of octadecyl-coated nanoparticles dispersed in tetradecane (which is described fully in the next section), and therefore, describe transitions to form homogeneous gels and glasses. In particular, the green triangles represent data points from dispersions of different concentrations, where the Baxter parameter was extracted from small angle neutron scattering (SANS) data. The Baxter parameter is related to the volume fraction at the gel point by the following equation, which is shown as the dashed line in Figure 1.2:

$$\tau_B = \frac{19\phi^2 - 2\phi + 1}{12(1-\phi)^2} \tag{3}$$

Importantly, the dispersions studied in this dissertation all lay outside the two phase region and are, therefore, homogeneous dispersions.

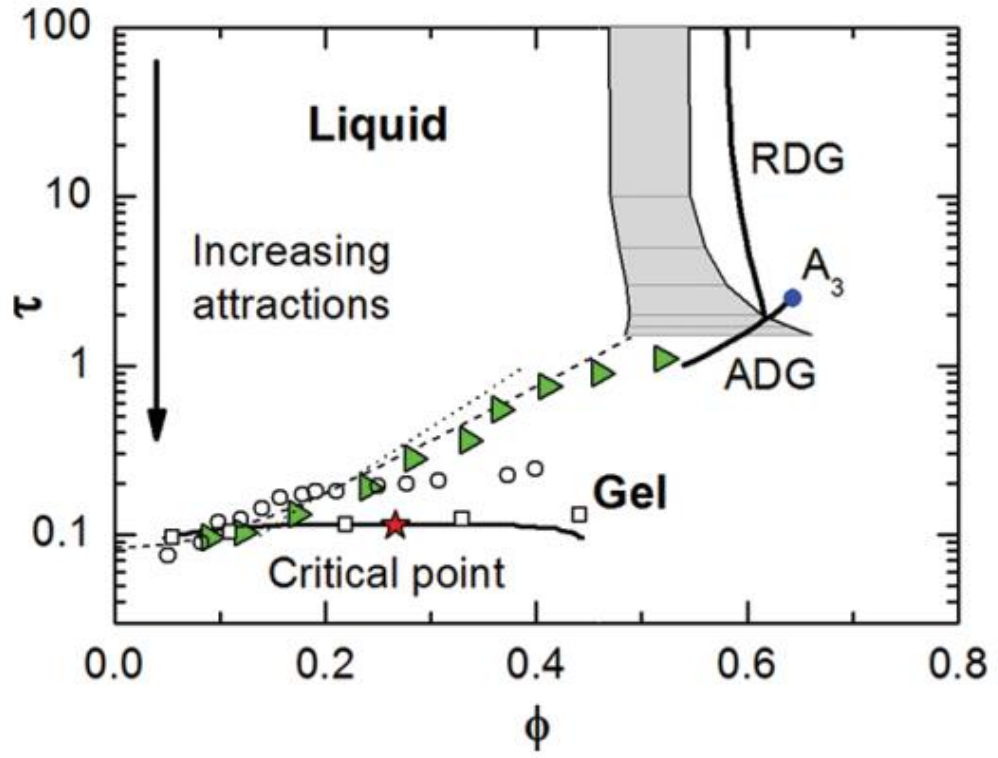

Figure 1.2: Phase diagram for adhesive hard spheres (AHS). The green triangles represent data points from AHS dispersions of octadecyl-coated silica nanoparticles dispersed in tetradecane at different concentrations, where the Baxter parameter was extracted from small angle neutron scattering (SANS) data. All samples contained in the dissertation are above the two-phase region. Reprinted with permission from reference [27]. Copyright 2012 American Chemical Society.

1.6 Thermoreversible Adhesive Hard Spheres

A common model system is the thermoreversible adhesive hard sphere (AHS) system, which consists of silica nanoparticles grafted with an octadecyl brush dispersed in an organic solvent [27-38] and is used to investigate aging behavior in this dissertation. In this system, gelation is triggered either by altering the solvent quality

or temperature. Specifically, switching from a solvent in which the particles are highly soluble to one in which they are poorly soluble will hinder the stability of the grafted brush layer and cause gelation. Alternatively, if certain solvents (such as tetradecane) are used, adjusting the temperature will induce a phase change in the brush, which will also result in gelation (Figure 1.3). Thus, by lowering the temperature, the octadecyl brush undergoes a liquid-to-solid phase change, thereby conveniently allowing the attractions between particles to be tuned by temperature [39].

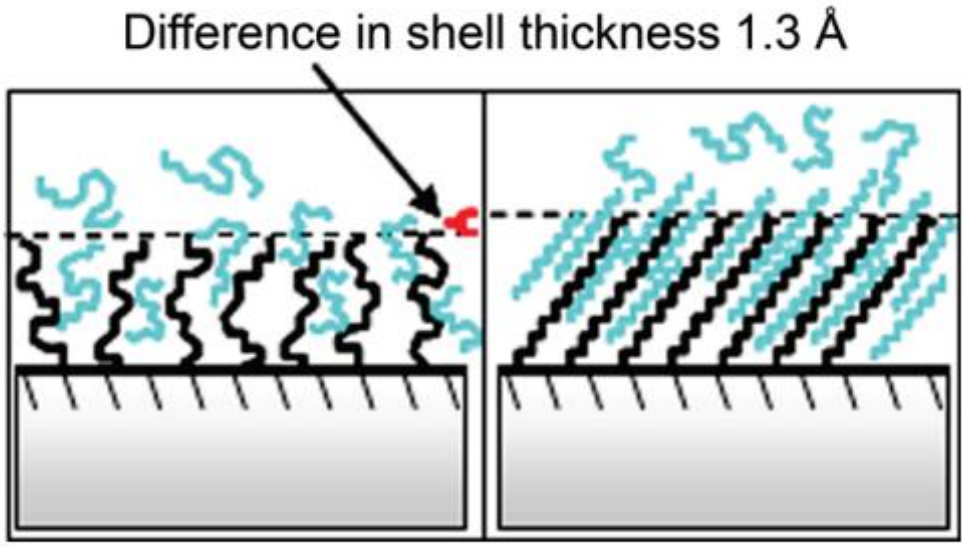

Figure 1.3: The octadecyl brush undergoes a liquid-to-solid phase change as the temperature is decreased. As the temperature is lowered, the brush height and solvent (blue) quantity are increased, as indicated on the figure by the straightening of the chains and the interdigitation of the solvent between the chains. Reprinted with permission from reference [39]. Copyright 2010 American Chemical Society.

Using neutron reflectometry and SANS, Eberle et al. measured the conformation change of the octadecyl brush grafted to silicon wafer and silica nanoparticles, respectively [39]. The experiments showed that as the temperature is decreased, the

chains transition from a fluidized state to a crystalline state as shown in Figure 1.3. In particular, during the phase transition, the brush height and solvent quantity increased, indicating the straightening of the chains and the interdigitation of the solvent between the chains. These results are consistent with the liquid-like behavior observed at high temperatures and gelation upon cooling. Importantly, this system can be thermally rejuvenated; when sheared in the liquid state, the structural history is completely erased, thus allowing a single sample to repeatedly tested and reused.

1.7 Aging Behavior and the Potential Energy Landscape

The properties of colloidal dispersions are known to change with gel age, yet the process and mechanism by which aging occurs is not yet well understood. Colloidal gels and glasses are in dynamically arrested states, and their limited mobility prevents them from reaching thermodynamic equilibrium on an experimental timescale. This results in aging behavior in which the bulk properties are a function of when the sample was first quenched and change with gel age [40-42]. This time-dependent behavior complicates the measurement and prediction of macroscopic behavior in these systems, which can negatively impact the efficacy and reliability of colloidal-based products, such as pharmaceuticals and food.

The mechanism that underlies aging phenomena is not known, yet it is proposed that colloidal gels are governed by their free energy landscape [43]. From this perspective, the thermodynamic equilibrium state is located in the deepest well but other potential energy minima exist (Figure 1.4). The system can only sample local potential energy minima via thermal motion and does not reach equilibrium on the timescale of the experiment. The system continually samples lower and lower energy states as it approaches thermodynamic equilibrium, which results in time-dependent bulk

properties. Aging in homogeneous gels is presumed to occur through small particle rearrangements occurring throughout the sample.

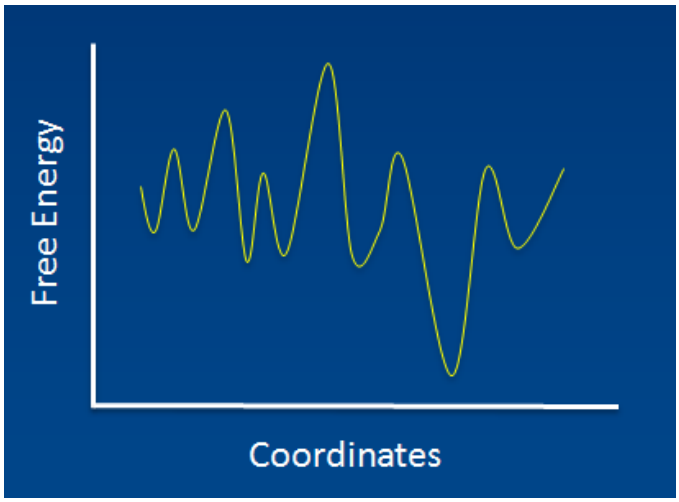

Figure 1.4: Cartoon depiction of a free energy landscape. From this perspective, the thermodynamic equilibrium state is located in the deepest well but other free energy minima exist. The system continually samples lower and lower energy states as it approaches thermodynamic equilibrium.

Due to its fundamental significance and industrial applicability, the microstructural basis of aging in homogenous gels and glasses is investigated in this dissertation using a well-characterized, model adhesive hard sphere (AHS) system, consisting of silica nanoparticles grafted with an octadecyl brush dispersed in tetradecane as described above. It is important to distinguish this homogenous system from phase-separating systems, such as the polymer-colloid system, which age due to coarsening and sedimentation [44], as described in Chapter 4.

1.8 Thesis Organization and Goals

This dissertation is focused on the development and characterization of stimuli-responsive systems for performance materials by (1) designing and testing novel light- and force-sensitive polymers for self-healing applications and (2) examining and characterizing the aging process in thermoreversible colloidal gels and glasses. In Chapter 2, we describe the design, synthesis and characterization of a novel photo-initiated polymer network. In particular, we hypothesize that by incorporating a dynamic bond into the network architecture, the material will be capable of undergoing a light-triggered, secondary polymerization that increases the modulus by several orders of magnitude while simultaneous strengthening the network. In contrast to conventional two-tiered polymerization systems, which impart dynamic behavior to the network through the use of a diffusible photoinitiator, the goal of this work is to develop a polymer network where the dynamic nature is inherent to the network itself. Moreover, we further hypothesize that such a network will be capable of undergoing photo-induced healing, reforming and strengthening after the sample has been severed. As the network is designed to respond to light, the properties of such a network can be controlled in time and space. In Chapter 3, the utility of the dynamic bond is extended by developing an experimental methodology to test whether the dynamic bond is also responsive to mechanical force in addition to light. Specifically, we incorporate a weak trithiocarbonate group into the center of poly(n-butyl acrylate) and test its utility as a mechanophore, or mechanically-active unit, via sonication experiments in solution. In contrast to other mechanophores, which require extensive synthetic procedures, the polymers described here can be synthesized in a single step via a reversible addition-fragmentation chain-transfer (RAFT) polymerization. Moreover, we aim to show that the proposed force-induced bond cleavage of the polymer chain at the mechanophore

initiates a force-driven radical polymerization, thus enabling the material to constructively respond to force on an experimentally relevant timescale.

In Chapters 4 and 5, we develop an experimental protocol to test whether aging in homogeneous, thermoreversible gels and glasses can be directly and quantitatively related to local, microstructural aging. Unlike phase-separated gels, which age due to gel coarsening or sedimentation, this model system is homogeneous and does not phase-separate or sediment, exhibiting a fundamentally distinct and previously unknown mechanism of aging. By simultaneously measuring the bulk properties and gel microstructure using rheometry and small angle neutron scattering (Rheo-SANS), respectively, we investigate the relationship between the time-dependent storage modulus and the underlying microstructure as the sample ages. The influence of the thermal and shear history on the aging process is also examined. Moreover, by using a thermally-responsive model system, we investigate the effects of shear on the aging process, as the system is fully rejuvenated via thermal cycling, and these results are directly compared to the effect of mechanical rejuvenation, which may appear to rejuvenate mechanical properties, but not fully restore the gel structure. Overall, the rheological and microstructural results for the colloidal gels and glasses examined in this work are analyzed from the free energy landscape viewpoint of colloidal aging. Finally, Chapter 6 summarizes the conclusions from the research contained in the dissertation and provides suggestions for future work.

Chapter 2

INCORPORATING DYNAMIC BONDS FOR LIGHT-RESPONSIVE, HEALABLE POLYMER NETWORKS

This chapter contains results that were published in *Advanced Materials* in 2015 [45].

2.1 Introduction

The ability to respond to environmental cues is a shared feature of all living organisms. As mentioned in the introductory chapter, there are many examples of stimuli-triggered processes found in nature ranging from the contraction of our pupils as a reaction to bright light to healing of wounds after a cut. These examples from the natural world inspire the rational design of synthetic responsive materials as a type of "smart material," which responds to environmental cues such as light, temperature, pressure and pH [1]. Such bioinspired engineered materials find application as self-healing polymers [1, 3, 12, 46], responsive coatings [1, 47], and shape memory materials [12, 48, 49].

To design for a macroscopic stimulus response, specific chemical units are typically built into the material at the molecular level [8, 9, 50]. The stimulus disrupts or alters the responsive chemical units incorporated in the material which causes a change in its macroscopic properties such as stability, strength, and processability [8]. Using light as a stimulus is advantageous because it is simple, inexpensive, and provides spatiotemporal control over the material's response while permitting the response to be triggered remotely [12, 46, 51]. As discussed in the introductory chapter, several groups

have successfully demonstrated photoreactive moieties such as cinnamates, coumarins, and anthracenes impart dynamic nature to the material because they are capable of undergoing reversible dimerization via cycloaddition and subsequent retro-cycloaddition under different wavelengths of UV light, which allow for light-triggered macroscopic self-healing of the network [13, 14, 52-56].

One approach toward responsive polymers utilizes macroinitiators, which are polymer chains that contain labile bonds that break upon application of a particular stimulus, such as light or heat. The resultant radical fragments initiate further polymerization to form distinct polymer architectures and morphologies [57]. Dynamic polymer networks can be engineered by incorporating macro-iniferter groups into the network architecture. Iniferters are chemical units that serve as an initiatior, transfer agent and terminator in radical polymerizations [58]. As discussed more fully in the introductory chapter, Matyjaszewski and coworkers demonstrated a self-healing material based on the reversible dissociation of chemical bonds in thiuram disulfide (TDS) under visible light in air and at room temperature [16]. Another novel use of iniferter chemistry to create dynamic polymer networks was shown by Zhou and Johnson, who incorporated trithiocarbonates (TTCs) to grow polymer chains via a photo-controlled radical polymerization [59]. The photo-growth was quantified by gel permeation chromatography (GPC) after selective cleavage of the TTC. These examples demonstrate how the incorporation of iniferter units enables responsive behavior in polymer networks through radical recombination and photo-growth.

In the work presented here, we introduce a novel class of materials that incorporate a photo-active monomer containing a dithiocarbamate iniferter into a polyurethane network to create a light-triggered dynamic network that can significantly

heal and strengthen on demand [45]. In particular, we show the ability of this new iniferter to function as a macroinitiator by initiating a light-triggered, radical-based polymerization that increases the network modulus by at least two orders of magnitude while simultaneously healing the material after damage. Unlike photoinitiators that eventually terminate after irradiation, the radicals produced in our system reversibly recombine, allowing radical generation within the network to be continuously triggered using light. The novelty of our approach lies in our ability to incorporate a labile bond with distinct chemical functionality into the crosslinks of a network such that it can initiate a secondary polymerization via the light-triggered dissociation of its own crosslinks, which is differs from conventional two-tiered polymerization systems which rely on the presence of a leachable photoinitiator [60, 61]. Furthermore, this approach enables spatiotemporal control over the bulk modulus, which is demonstrated by photopatterning the material. Finally, the secondary polymerization is leveraged to permanently effect a shape change in the network.

2.2 Experimental Methods

2.2.1 Monomer Synthesis

The monomer shown in Figure 2.5 was required to impart dynamic nature to the network and is referred to as the labile bond crosslinker (LBCL). The synthesis of the LBCL is shown in Figure 2.1. The salt was first synthesized by analogy to an established procedure [62]. In brief, 2-(ethylamino)ethanol (8.9 g, 0.1 mol) was dissolved in acetone (100 mL) and stirred for 10 minutes at room temperature and then submerged in an ice bath. Carbon disulfide (7.6 g, 0.1 mol) was added in a dropwise fashion to ensure that the reaction maintained a temperature of 0°C. Addition of the CS_2 caused the mixture to turn yellow. The solution reacted for an additional 10 minutes after all of the CS_2 was added. An off-white precipitate was formed by quenching with an aqueous sodium hydroxide solution (4.0 g NaOH in 7.95 mL water). The solvents were evaporated, leaving behind an off-white salt. The salt was then dissolved in a minimal volume of ethanol to which a solution of α,α'-dichloro-p-xylene (7.0 g, 0.04 mol) in 150 mL THF was carefully added. The reaction continued overnight at room temperature. The solvents were removed by rotary evaporation and the resulting solid was dissolved in dichloromethane and washed three times with water. The dichloromethane was evaporated and the product was purified by column chromatography (Silica gel, gradient elution of 1:4 to 4:1 ethyl acetate in hexane, v/v) to afford an off-white liquid in 70% yield which solidified upon standing. R_f 0.57 (4:1) ethyl acetate in hexanes. ^{1}H NMR (400 MHz, $CDCl_3$, δ): 7.33 (s, 4H, ArH), 4.50 (s, 4H; SCH_2), 4.19 (m, 4H; NCH_2), 4.04-3.76 (m, 8H; NCH_2CH_2), 1.29 (t, 6H; CH_3); ^{13}C NMR (100 MHz, $CDCl_3$, δ): 198.4 (C=S), 135.5 (Ar**C**CH_2), 130.1 (ArC), 61.4 (N**C**H_2CH_2), 56.6 (NCH_2**C**H_2), 49.2 (N**C**H_2CH_3), 42.4 (SCH_2), 12.6 (CH_3) ; HRMS

(LIFDI) *m*/*z* [M]: calcd for $C_{18}H_{28}N_2O_2S_4$, 432.1034; found, 432.1046. NMR spectra are shown in Appendix A (Figures A.2 and A.3).

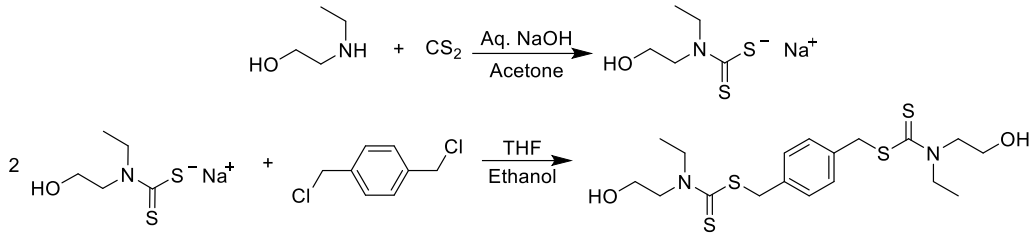

Figure 2.1: Synthetic procedure for the formation of the labile bond crosslinker (LBCL).

2.2.2 Network Formation

LBCL (0.389 g, 0.9 mmol) was dissolved in DMF (2.1 g) and stirred with triethanolamine (TEA, 0.276 g, 1.85 mmol) and ethylene glycol dimethacrylate (EGDMA, 0.595 g, 3 mmol) in a 20 mL scintillation vial. The solution was heated to 50°C while stirring to reduce the solubility of gas in the solution and prevent bubble formation in the films. The solution was cooled to 35 °C and two drops of dibutyltin dilaurate (DBTDL) were carefully added. The solution was stirred and added to hexamethylene diisocyanate (HDI, 0.505 g, 3 mmol) in a scintillation vial (Figure 2.2). The solution was mixed and cast between two glass slides separated by a 1/32nd or 1/16th inch spacer held with binder clips. It polymerized overnight to yield a transparent, non-tacky, rubbery network as shown in Figure 2.3.

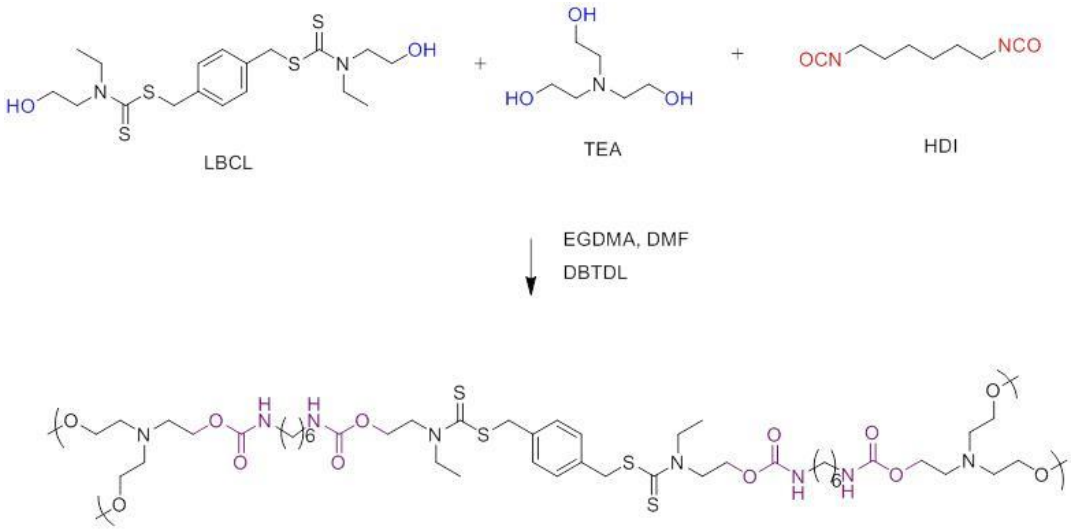

Figure 2.2: Formation of the polyurethane network. The network was formed with LBCL, TEA, HDI, EGDMA in DMF with DBTDL. Scheme adapted from Matyjaszewski and coworkers [16].

Figure 2.3: The resulting polymer film containing LBCL was transparent, rubbery and non-tacky.

2.2.3 Measurements

2.2.3.1 UV-Vis Spectroscopy

UV-Vis measurements of the LBCL diol (1 mg/mL) were conducted using a NanoDrop 2000 Spectrophotometer from Thermo Scientific. A 10 mm quartz cuvette

was used for the measurement displayed in Figure A.1 (see Appendix). The UV-Vis spectrum shows that the LBCL strongly absorbs 320-380 nm light. All experiments were conducted under controllable conditions—8 mW cm^{-2} of 365 nm UV light. Polymer films containing the LBCL are stable to indoor ambient light. The monomer can be stored at room temperature for months; however, storing the network for longer than two days is not recommended as it results in solvent evaporation.

2.2.3.2 NMR Spectroscopy

NMR spectra were obtained from a Bruker AV 400 NMR Spectrometer. All NMR spectra are provided in Appendix A.

2.2.3.3 Fourier Transform Infrared Spectroscopy (FTIR)

FTIR experiments were conducted using a Nicolet iS50 FT-IR from Thermo Scientific equipped with a box to horizontally place films and hold the light guide. Series experiments were performed using a DTGS KBr detector and white light source. Films were placed between glass slides and solutions for the model system study were injected between two glass slides separated by a $1/32^{nd}$ inch spacer and held together with binder clips. All samples were irradiated using a high pressure mercury lamp (Exfo, Omnicure Series 2000) equipped with a 365 nm interference filter at 8 mW cm^{-2}. Data was analyzed with Omnic software (Nicolet). The peak between 6250-6100 cm^{-1} corresponds to the first overtone of the carbon-hydrogen stretch (CH_2=) on the methacrylate and its disappearance was monitored to determine the conversion of the dimethacrylate. Conversion was determined from peak areas at each time point (conversion=1-(peak area/initial peak area)) for samples in which a flat baseline existed. All samples went to nearly full conversion as shown in Figure A.4. The baseline in the

spectra was corrected using the Omnic Software for the range shown in Figure A.4 (Appendix A). All conversion data was obtained using films that were formed the day prior to measurement.

2.2.3.4 Dynamic Mechanical Analysis (DMA)

DMA measurements were performed on a Q800 dynamic mechanical analyzer from TA Instruments equipped with an Air Chiller System 3 cooling accessory. All experiments were conducted in tensile mode at room temperature. Samples were measured at 0.15% strain at 1 Hz. Table 2.1 contains averaged data of dynamic modulus values from three different samples, which were prepared separately.

2.2.4 Healing Experiments

Networks containing EGDMA (30 wt%) were cast between two glass slides separated by a 1.6 mm spacer held with binder clips. The modulus and strain at break were determined for each sample. The two separated pieces were then rejoined and placed between two glass slides with four binder clips to ensure contact between ruptured surfaces during irradiation. The samples were irradiated for two hours and post-irradiation modulus and strain at break values were measured.

2.2.5 Shape Change

Networks containing EGDMA (30 wt%) were cast between two glass slides separated by a 1.6 mm spacer held with binder clips. The network was held in a specific shape using double-sided tape and irradiated for two hours. When the tape was removed, the network remained in the desired configuration.

2.3 Results and Discussion

The design of a network capable of light-triggered modulus enhancement is achieved by incorporating a labile carbon-dithiocarbamate bond into the network backbone (designated as LBCL and shown in Figure 2.4). It is hypothesized that this bond will homolytically cleave under low intensity UV light, generating a radical that will initiate a free radical polymerization reaction with dimethacrylate monomers incorporated into the network prior to formation. This secondary polymerization increases the crosslink density, thereby enhancing the modulus, and ultimately, the strength of the material. The labile functionality of the carbon-sulfur bond is due to the presence of the dithiocarbamate functional group, which is an iniferter unit (shown in green in Figure 2.5). The dithiocarbamate is placed adjacent to a paraxylene group (shown in blue in Figure 2.5) to promote the formation of an initiating carbon-centered radical upon irradiation. Alcohol end groups (shown in purple in Figure 2.5) were selected to form a polyurethane network via alcohol-isocyanate chemistry, which is chemically orthogonal to the radical-based secondary polymerization. This orthogonal strategy is a two-stage polymerization that implements a macroinitiator [60].

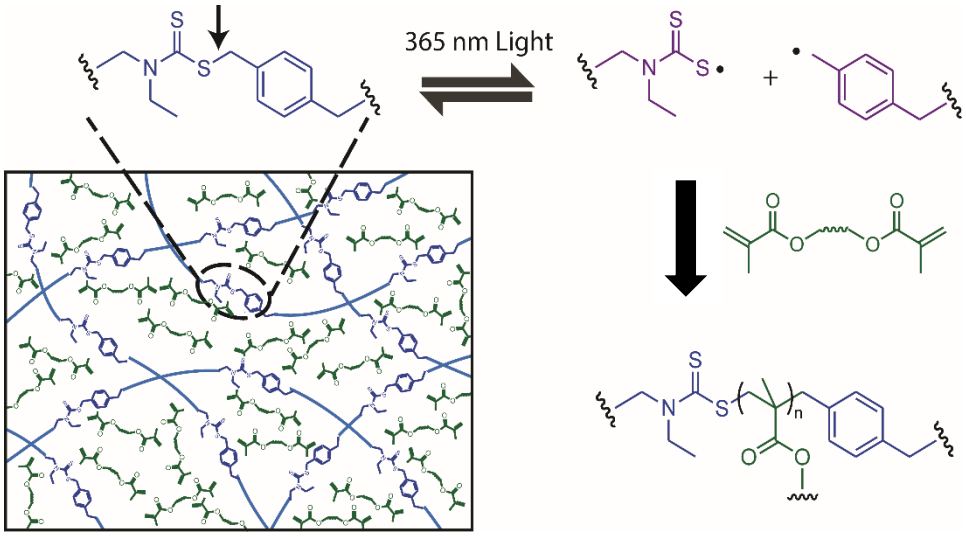

Figure 2.4: The overall strategy is shown. The LBCL is built into the network architecture and initiates a photo-triggered methacrylate polymerization.

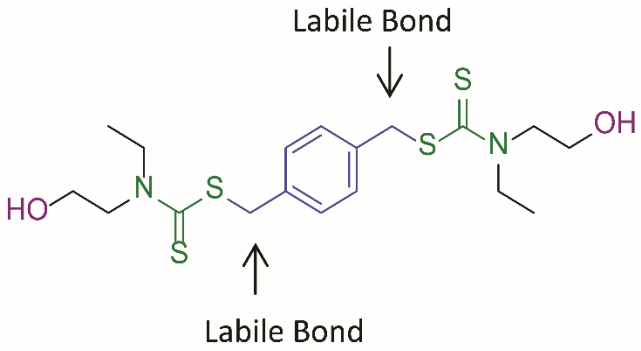

Figure 2.5: The final monomer design for the labile bond crosslinker (LBCL) is shown. The labile functionality of the carbon-sulfur bond is due to the presence of the dithiocarbamate functional group, which is an iniferter unit (green). The dithiocarbamate is placed adjacent to a paraxylene group (blue) to promote the formation of an initiating carbon-centered radical upon irradiation. Alcohol end groups (purple) were selected to form a polyurethane network via alcohol-isocyanate chemistry, which is chemically orthogonal to the radical-based secondary polymerization.

A model system was examined to verify that the labile carbon-dithiocarbamate bond photocleaves under weak UV light and initiates a polymerization in solution. The LBCL (10 wt%) was dissolved in DMF and ethylene glycol dimethacrylate (EGDMA, 15 wt%) and exposed to 8 mW cm^{-2} of 365 nm light. Polymerization commenced immediately upon irradiation (light on at 10 minutes) and continued to near full conversion (Figure 2.6A) as monitored with Fourier transform infrared spectroscopy (FTIR). The same study was repeated without (1) LBCL and (2) light as controls, revealing no significant conversion (Figure 2.6A). This model study demonstrates that LBCL and light are both required to initiate polymerization under low intensity UV light.

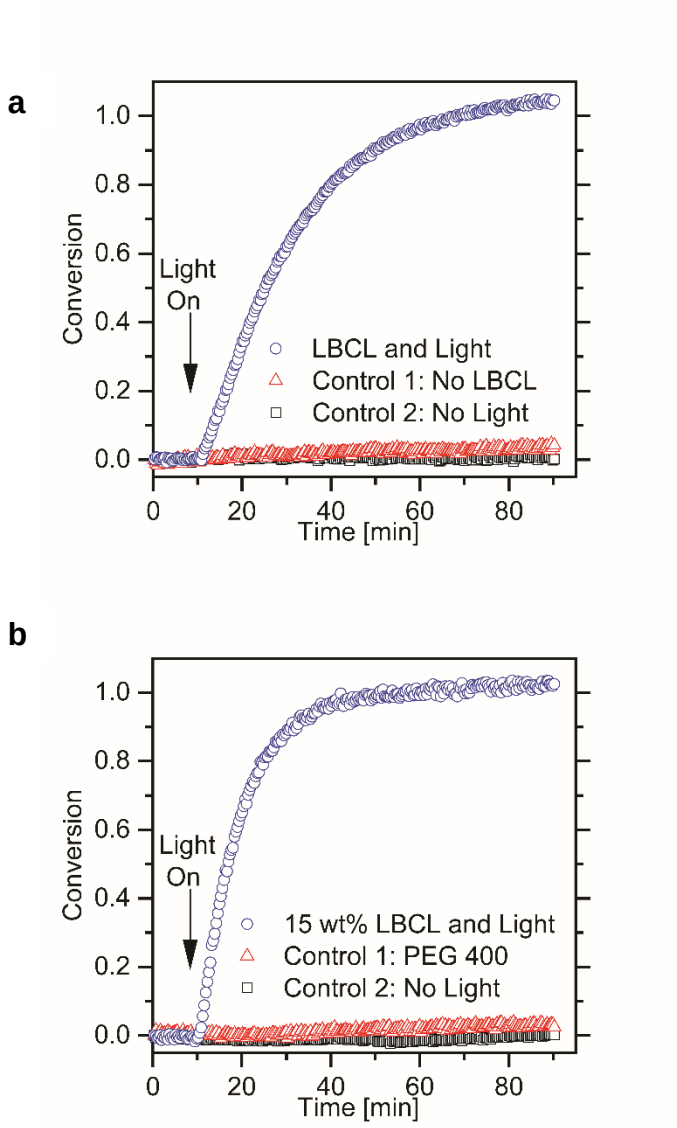

Figure 2.6: The labile bond crosslinker (LBCL) initiates a radical polymerization in both a solution-based model system and when incorporated into a polyurethane network. **A.** Conversion of dimethacrylate in a solution-based model system containing the dimethacrylate and DMF as measured by FTIR. Control 1 does not include LBCL while Control 2 does not use light. **B.** Light initiates a secondary polymerization in a polyurethane network. Control 1 replaces LBCL with PEG 400 to retain the molecular weight between crosslinks while Control 2 uses no light. In both conversion studies, the samples were irradiated beginning at 10 minutes using 365 nm light at an intensity of 8 mW cm^{-2}.

As described in section 2.2.2, the photo-triggered strengthening networks were formed with LBCL, triethanolamine (TEA) as a trifunctional crosslinker, and hexamethylene diisocyanate (HDI) in DMF with dibutyltin dilaurate (DBTDL) as the catalyst and in the presence of ethylene glycol dimethacrylate (EGDMA)—a network design adapted from Matyjaszewski and coworkers [21]. The polymerization proceeded overnight to yield a transparent, non-tacky, rubbery crosslinked network. The secondary photopolymerization within the network was triggered by light and quantified using FTIR. Immediately after irradiation (365 nm at an intensity of 8 mW cm^{-2}), the materials undergo polymerization and proceed to nearly full conversion (Figure 2.6B, also see Appendix A). Furthermore, two control experiments were performed where LBCL was replaced with PEG 400 which retains the molecular weight between crosslinks and where the LBCL films were not irradiated. These experiments demonstrate that both LBCL and light must be present for the materials to exhibit a photochemical response. While these samples were continuously irradiated, the conversion of the secondary polymerization plateaus when the light is turned off and proceeds when the light is turned on, thus enabling temporal control of the secondary polymerization in the network (Figure 2.7).

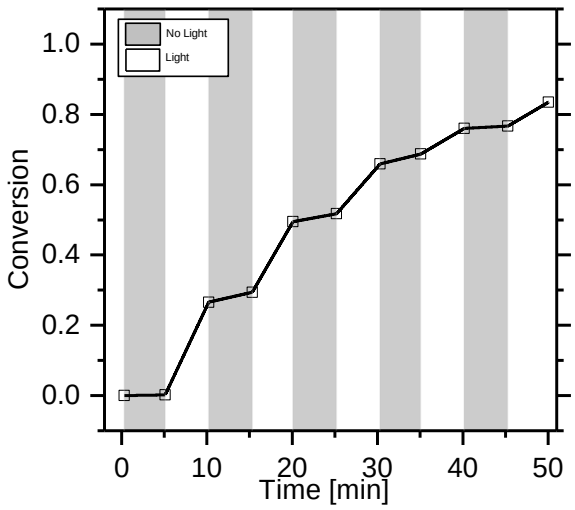

Figure 2.7: Temporal control of secondary polymerization. The sample was exposed to 8 mW cm^{-2} of 365 nm light in five minute intervals.

As displayed in Table 2.1, the modulus can increase by orders of magnitude after two hours of irradiation. These bulk property changes are attributed to an increase in crosslink density. All films have similar initial moduli before irradiation, but exhibit significant increases owing to secondary crosslinking, which are directly related to the initial EGDMA concentration. Therefore, the final modulus can be precisely tuned for a particular application through the selection of the initial EGDMA concentration.

Table 2.1: Crosslinked networks with varying amounts of EGDMA and the corresponding changes in storage modulus before and after two hours of irradiation (365 nm at 8 mW cm^{-2}). The total weight of each formulation was kept constant by adjusting the amount of DMF in the sample.

EGDMA [wt %]	**Before Irradiation Modulus [MPa]**	**After Irradiation Modulus [MPa]**	**Ratio: Final Modulus/ Initial Modulus**
7.5	0.13±0.06	0.4±0.1	3.5±0.6
15	0.4±0.1	4±1	11±3
22.5	0.3±0.2	16±1	60±30
30	0.3±0.1	50±10	180±50

One such application of this material is light-triggered healing. To our knowledge, the material presented here was the first demonstration of a polymer network that uses a macroinitiator for simultaneous photo-healing and photo-strengthening. A specimen was severed, as shown in Figure 2.8A, and then held in contact using glass slides with binder clips under 365 nm light at 8 mW cm^{-2} for two hours, to yield a single, reformed material, as displayed in Figure 2.8B. The healing is quantified by measuring the modulus and strain at break before and after irradiation (Table 2.2). Not only does the secondary polymerization result in healing, but also a two orders of magnitude increase in modulus. While the healed samples exhibit lower failure strains, their strength can increase by over 100%. Furthermore, after the methacrylates are depleted, the network repeatedly photo-heals via iniferter rearrangement, thus highlighting the added functionality imparted by iniferter unit built into the network backbone (Figure 2.9).

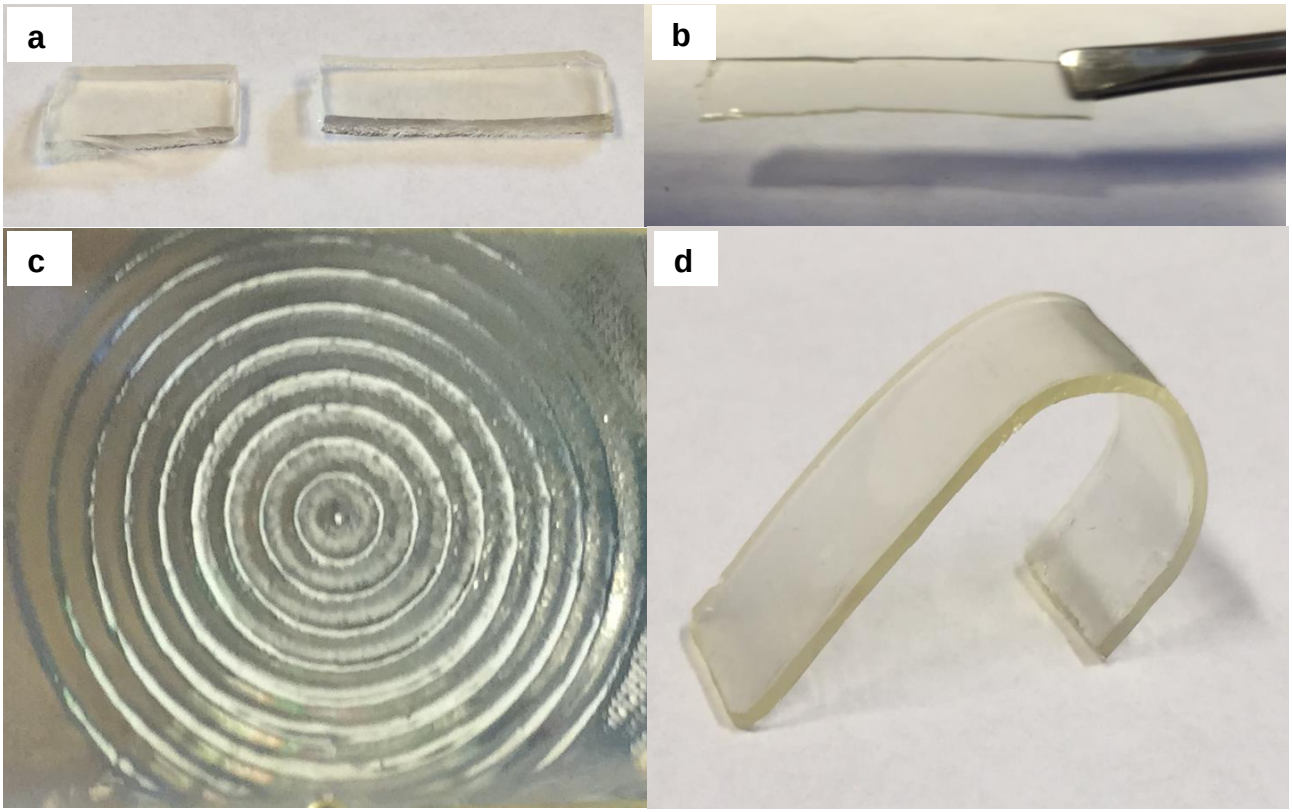

Figure 2.8: Demonstrations using the photo-activated strengthening network. **A.** The damaged material prior to irradiation. The original sample was approximately 20 mm long, 4.3 mm wide and 1.2 mm thick. **B.** The material undergoes light-triggered self-repair while strengthening after damage. The sample can be reformed as a single piece. The arrow points to rejoined region after healing. **C.** Our approach allows us to exert spatial control over bulk properties changes by overlaying a photomask with concentric circles (inset). Patterning is due to polymer shrinkage and, likely, refractive index changes. The photomask is 2 cm across. **D.** The material's modulus increases drastically during irradation, thus locking it into a specific configuration post-irradiation. The original film dimensions were approximately 5.7 cm long, 2 cm wide and 1.2 mm thick. All demonstrations were conducted using 30 wt% EGDMA samples and irradiated with 8 mW cm^{-2} of 365 nm light.

Table 2.2: Moduli, strain at break and strength measurements before and after light-triggered healing.

	Before Irradiation			After Irradiation		
EGDMA [wt %]	Modulus [MPa]	Strain at Break [%]	Strength [MPa]	Modulus [MPa]	Strain at Break [%]	Strength [MPa]
15	0.3±.1	20±10	0.06±0.03	2.0±0.3	10±10	0.10±0.05
30	0.5±.4	28±9	0.10±0.03	50±20	1.3±0.6	0.4±0.3

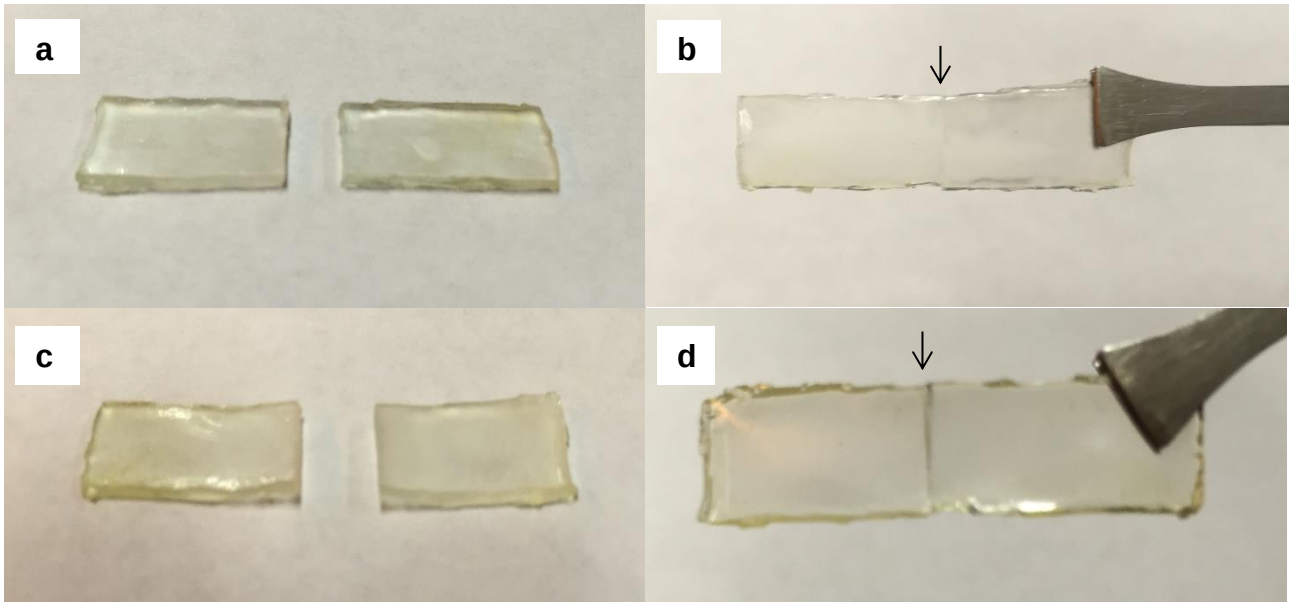

Figure 2.9: Repeated photo-healing of the same sample after full photo-polymerization of the methacrylate groups. **A.** The damaged sample prior to irradiation. **B.** UV light (8 mW cm^{-2} of 365 nm light for 1.5 hours) heals the previously severed sample and the healed specimen is held as a single unit. **C.** The sample is severed along the original incision. **D.** UV light (same conditions as above) remends the sample. This highlights the ability of our system to photo-heal using two distinct mechanisms: (1) a radical-based methacrylate polymerization and (2) rearrangement via iniferter reshuffling.

Since the secondary healing and strengthening polymerization reaction is photo-triggered, bulk property changes can be photopatterned. By overlaying a photomask prior to irradiation (365 nm light at 8 mW cm^{-2}), areas of the film that are subsequently exposed to light undergo modulus enhancement while the covered areas remain unchanged. Figure 2.8C shows that the concentric pattern from the photomask was transferred directly onto the film with excellent fidelity, thus enabling spatial control over the bulk properties. Furthermore, the spatial control exhibited by photopatterning can be leveraged to confine healing to a specific region.

Finally, we exploit the significant mechanical property changes evident upon photopolymerization to permanently alter the material's shape using light. A 30 wt% EGDMA sample was held in a specific configuration and exposed to 8 mW cm^{-2} of 365 nm light for two hours. The light triggers the secondary methacrylate polymerization, thus increasing the number of crosslinks and 'locking' the material in the desired configuration post-irradiation, as displayed in Figure 2.8D. This result enables the creation of 3D materials which can be additionally photo-welded (i.e., photo-healed) to fabricate complex objects.

2.4 Summary and Conclusions

In summary, we have developed a light-triggered dynamic network that significantly strengthens on demand. By incorporating a new photo-active monomer containing a dithiocarbamate iniferter unit with a dimethacrylate monomer within a polyurethane network, the material's modulus can increase by over two orders of magnitude after long-wavelength UV irradiation. We show that the acquired increase in modulus is controlled by the initial concentration of EGDMA, thus allowing the final modulus of the material to be tuned a priori for a particular application. We show the

first demonstration of a polymer network capable of simultaneously strengthening and healing after damage using a macroinitiator. Furthermore, our approach allows us to spatially control where these changes take place and permanently alter the shape of the material. In addition to its use as a strengthening and healable material, the formulation may be modified for other applications that require a secondary polymerization, such as wrinkling [61] and surface functionalization.

Chapter 3

FORCE-INDUCED CLEAVAGE OFA LABILE BOND FOR MECHANOCHEMICAL CROSSLINKING

3.1 Introduction

Biological systems display a wide range of remarkable responses to mechanical stimuli, including hearing, muscle contraction, wound healing and bone strengthening [63-65]. However, to date, most synthetic polymers are incapable of constructively responding to mechanical stimuli. Stress typically leads to material fatigue and failure, which reduces the efficacy of the product and/or compromises user safety. Examples from nature motivate the design of force-responsive materials, which constructively respond to mechanical stimuli by adjusting their properties to meet the demands of a changing environment.

One approach for designing such a force-responsive material incorporates mechanophores, or mechanically-sensitive chemical groups, into polymer chains [19, 20]. The unselective cleavage of polymers in response to forces generated during sonication was first reported in the 1930s [66], but only recently have polymers been designed for selective scission at a specific unit in the polymer chain (i.e., using a mechanophore) [67]. Mechanophores are typically embedded in the center of polymer chains to propagate enough force along the polymer backbone to activate the mechanophore (Figure 3.1). To date, several cyclic molecules have been identified as mechanophores including β-lactam [68], 1,2-dioxetane [69], dicyano-substituted cyclobutane [70], bicyclo[4.2.0]octane [71], 1,2-disubstituted benzocyclobutene [72]

and gem-difluorocyclopropane [73], thus demonstrating the successful implementation of mechanophores into polymer chains to actively and selectively respond to a traditionally degradative stimulus.

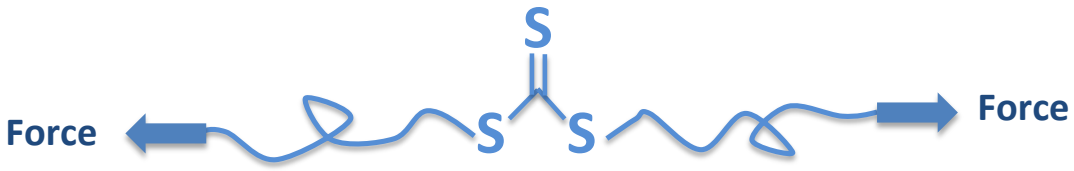

Figure 3.1: The mechanophore (trithiocarbonate moiety) is located in the center of the polymer chain. In the presence of sonicating energy, force propagates along the backbone and activates the trithiocarbonate mechanophore.

Of particular interest to this work is leveraging mechanically-induced chemical transformations to impart additional capability to the material. For example, mechanophores, such as spiropyran, change color when force is applied, providing a visual warning that the material may fail [22]. Moreover, Ramirez et al. coupled the mechanical activation of dibromocyclopropane mechanophores with nucleophilic displacement crosslinking reactions to impart enhanced strength to the polymer, resulting in a crosslinked gel sixteen hours after force was applied [23]. These significant advances in mechanochemistry demonstrate the broad utility of force-sensitive materials while highlighting the importance of determining novel mechanophores for designing advanced, responsive materials.

Towards the design of new mechanophores, Lee and coworkers quantified the mechanical strength of polymers containing known weak bonds. In particular, the carbon-sulfur bond of a thioester was determined to be 71-74 kcal mol^{-1} by conducting

pulsed sonication studies [74]. These results complement our previous work in which a labile carbon-sulfur bond of a dithiocarbamate was incorporated into the crosslinks of a polymer network and selectively cleaved in response to light, thus enabling macroscopic healing and strengthening of the material [45]. Based on these studies, we hypothesized that the labile carbon-sulfur bond of a thiocarbonylthio group would selectively cleave in response to force.

In the work presented here, we demonstrate the dual functionality of a thiocarbonylthio group, serving as (1) a chain transfer agent, which is used to synthesize the initial polymer, and (2) a mechanophore, which can initiate a force-driven radical polymerization. The introduction of this mechanophore enables the material to respond to force on an experimentally relevant timescale. In contrast to other mechanophores, which require extensive synthetic procedures, these polymers are synthesized in a single step via a reversible addition-fragmentation chain-transfer (RAFT) polymerization. Moreover, the cleavage of this mechanophore is coupled to a subsequent radical polymerization, which initiates within minutes of the initial application of force. Furthermore, the utility and versatility of this force-responsive polymer is illustrated by demonstrating its stress-induced scission initiates various crosslinking chemistries.

3.2 Experimental Methods

Sonication Experiments: All solutions (10 mL) were prepared using BHT-free THF. The tetraethylene glycol diacrylate was passed through a basic alumina plug to remove inhibitor. The solutions were kept in an ice bath and continuously sonicated using a 13 mm diameter probe and Model W-225R sonicator from Heating Systems Ultrasonics, Inc operating at 20 kHz. Nitrogen was bubbled through the solution throughout the duration of the experiment.

Radical Trap Experiments: Solutions (10 mL) containing a TEMPO radical trap and the mechanically-sensitive polymer were prepared using BHT-free THF. The solutions were kept in an ice bath and continuously sonicated using the same sonicator and probe as described above. Solutions were pulsed for 15 minutes (5 seconds on, 5 seconds off) and then sonicated continuously for 15 minutes. Nitrogen was bubbled through the solution throughout the duration of the experiment.

Polymer Synthesis: Dibenzyl trithiocarbonate was purchased from Sigma Aldrich and used as received. N-butyl acrylate was also purchased from Sigma Aldrich and passed through a basic alumina column to remove the inhibitor. AIBN was purchased from Sigma Aldrich and recrystallized twice from methanol before use. N-butyl acrylate, AIBN and dibenzyl trithiocarbonate were dissolved in an anisole solution containing 5 wt% DMF at the concentrations given in Table 3.1. The mixture was poured into a Schlenk tube equipped with a stir bar and stopcock, which was degassed by three freeze-thaw-pump cycles. The Schlenk tube was filled with argon (3-4 psig) and heated in an oil bath at 72°C for the time indicated in the table. The reaction mixture was diluted with THF (2 fold dilution) and precipitated in a methanol/water (60/40, v/v) mixture (10 fold dilution). The upper clear layer of solution was decanted and the polymer was collected and dried under vacuum for 2 days. The molecular weights of the polymers were determined by gel permeation chromatography (GPC) in THF using polystyrene standards.

Table 3.1: Concentrations and reaction conditions for RAFT polymerization with corresponding polymer properties. (M: monomer, CTA: chain transfer agent, S: solvent; $M_{n,\,calc}$: molecular weight calculated based on conversion (determined by NMR), Đ: dispersity)

Polymer	**$[M]_0/[CTA]_0/[AIBN]_0$ (mol/mol/mol)**	**$[S]/[M]_0$ (wt/wt)**	**Time (h)**	**Conv**	**$M_{n,calc}$ (kDa)**	**$M_{n,SEC}$ (kDa)**	**$M_{w,SEC}$ (kDa)**	**Đ**
54 kDa	506/1/0.12	0.5/1	5	95%	62.0	54.1	62.0	1.15
107 kDa	1086/1/0.11	0.5/1	4.5	89%	123.8	107.3	119.4	1.11
132 kDa	1696/1/0.10	1/1	9	89%	193.8	131.8	167.9	1.27

3.3 Results and Discussion

The mechanically-active polymer containing a trithiocarbonate mechanophore was synthesized by a one-step RAFT polymerization (described above). As a result of the polymerization with a difunctional trithiocarbonate RAFT agent (i.e., dibenzyl trithiocarbonate), the mechanophore is located at the center of the polymer chain (see Figure 3.1). A molecular weight of approximately 130 kDa was targeted so that the polymer is able to propagate sufficient force along the backbone and activate the trithiocarbonate mechanophore. It is hypothesized that this bond will homolytically cleave when activated by force, generating polymerization-initiating radicals (Figure 3.2.).

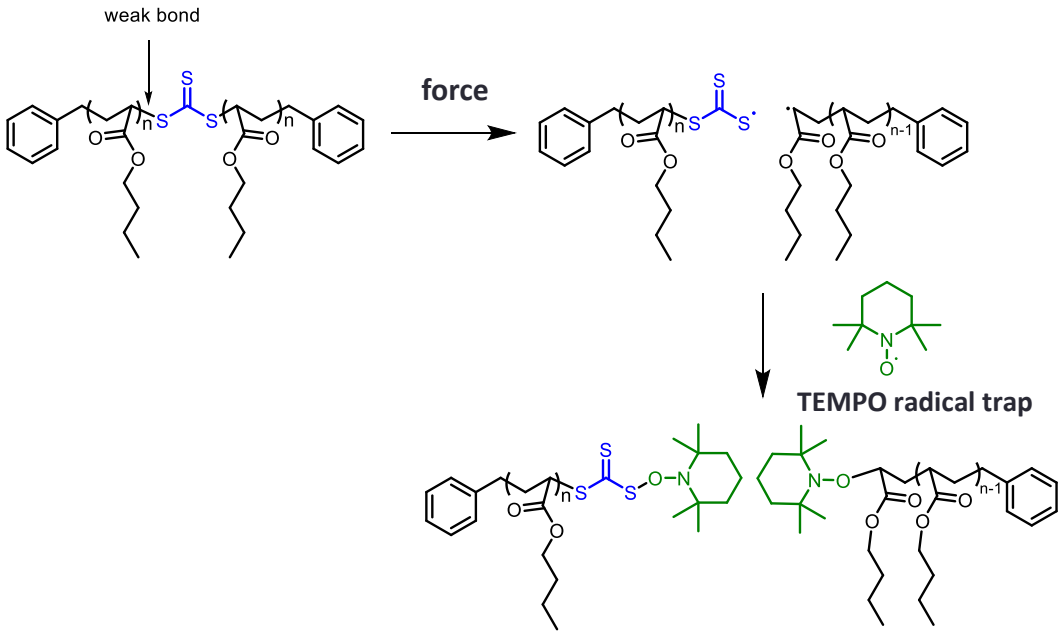

Figure 3.2: The trithiocarbonate mechanophore is incorporated into the center of poly(n-butyl acrylate). During sonication, the polymer is expected to cleave, generating radicals which will subsequently react with the radical trap (i.e., TEMPO), as shown. Note that the polymer is symmetric and the polymer may cleave at either carbon-trithiocarbonate bond.

The selective scission of the polymer in response to force was determined via radical trapping experiments (Figure 3.2). In the presence of sonicating energy, the polymer is expected to cleave homolytically at the carbon-trithiocarbonate bond and thereby produce radicals, which can then be trapped. In particular, a TEMPO radical trap was dissolved in a BHT-free THF solution containing n-poly(butyl acrylate) with trithiocarbonate functionality (0.5 wt%). A control solution containing a TEMPO radical trap in BHT-free THF was prepared containing 0.5 wt% n-poly(butyl acrylate) standard (without a trithiocarbonate mechanophore) of similar molecular weight (M_w = 168 kDa). Polymer solutions were sonicated in an ice bath, a process typically used in mechanochemical studies in which sonic energy is used to produce small

bubbles that subsequently collapse, to generate large enough forces to cleave the polymer chains. Gel permeation chromatography (GPC) traces of the resulting solutions are shown in Figure 3.3A and Figure 3.3B, respectively. In particular, Figure 3.3A displays the GPC trace of synthesized polymer containing trithiocarbonate functionality (black line) in addition to the GPC traces of polymer solutions exposed to light (purple line) and sonication (blue, dashed line). As expected (see Chapter 2), applying light to the polymer led to the cleavage of the trithiocarbonate group, as indicated by the decrease in molecular weight shown in Figure 3.3A. Importantly, the resultant GPC trace of the polymer following sonication also shows a similar decrease in the molecular weight, signifying that the trithiocarbonate moiety functions as a mechanophore. Given the large molecular weight of the polymer, some unselective cleavage of a polymer not containing the mechanophore is expected, as shown in Figure 3.3B; however, the cleavage of the polymer containing the mechanophore was notably enhanced.

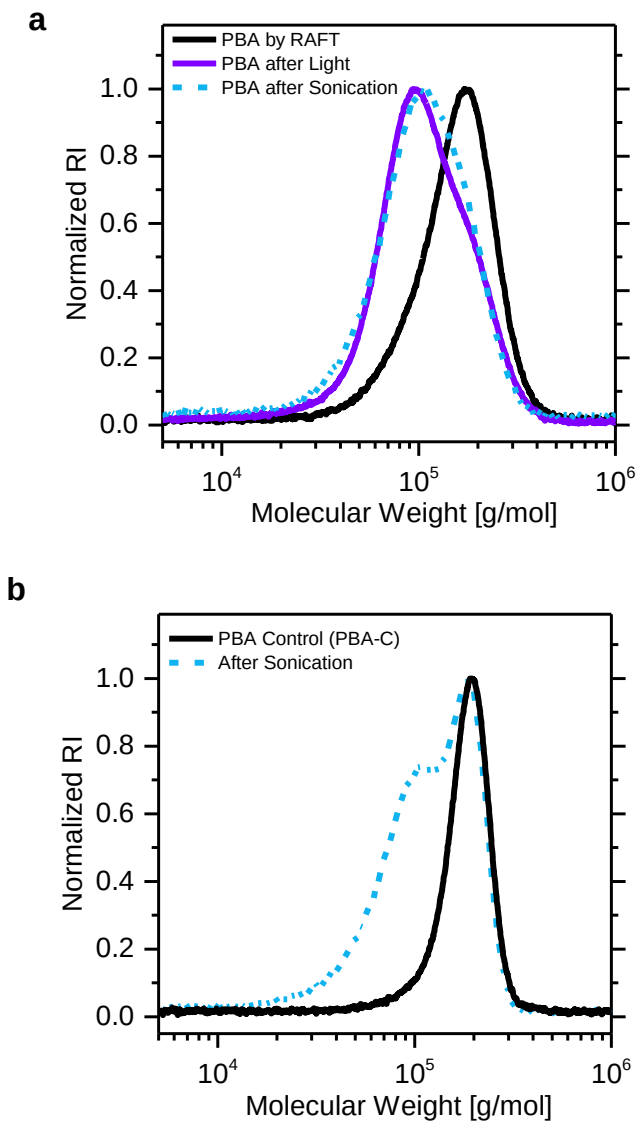

Figure 3.3: **A.** GPC traces for the polymer containing the trithiocarbonate mechanophore after exposure to no stimulus, light and sonication in the presence of a radical trap. **B.** GPC traces for the control poly(n-butyl acrylate) without the mechanophore after exposure to no stimulus and after sonication in the presence of a radical tap. A comparison of the results in **A** and **B** indicate enhanced, selective cleavage at the trithiocarbonate mechanophore.

Further experiments demonstrate that a molecular weight of approximately 100 kDa was necessary for sonication-induced cleavage. The GPC trace of the mechanophore-containing polymer (107 kDa) showed force-induced cleavage following 30 minutes of sonication (Figure 3.6A), yet the control polymer of similar molecular weight (101 kDa) showed little to no significant changes in response to the same sonication conditions (Figure 3.6B). Interestingly, a mechanophore-containing polymer of lower molecular weight (54 kDa) showed little to no force-induced cleavage under the same sonication conditions (Figure 3.5), placing a lower bound on the molecular weight required to activate the trithiocarbonate mechanophore.

The time evolution of the force-induced cleavage in the 107 kDa polymer is shown in Figure 3.6. The evolution in molecular weight in response to sonication forces was evaluated by fitting a Gaussian function to each GPC trace. Following this analysis, the molecular weight after two hours of sonication was exactly one half of the starting molecular weight, indicating that two hours of sonication is sufficient to fully cleave the chains at the mechanophore. Applying force to the cleaved polymer chains in excess of two hours of sonication led to continued breakage of the chains (likely higher molecular weight chains at the high end of the distribution). Overall, these results suggest that a molecular weight of approximately 100 kDa is required to activate the thiocarbonylthio mechanophore, which cleaves within two hours in response to continuous sonication.

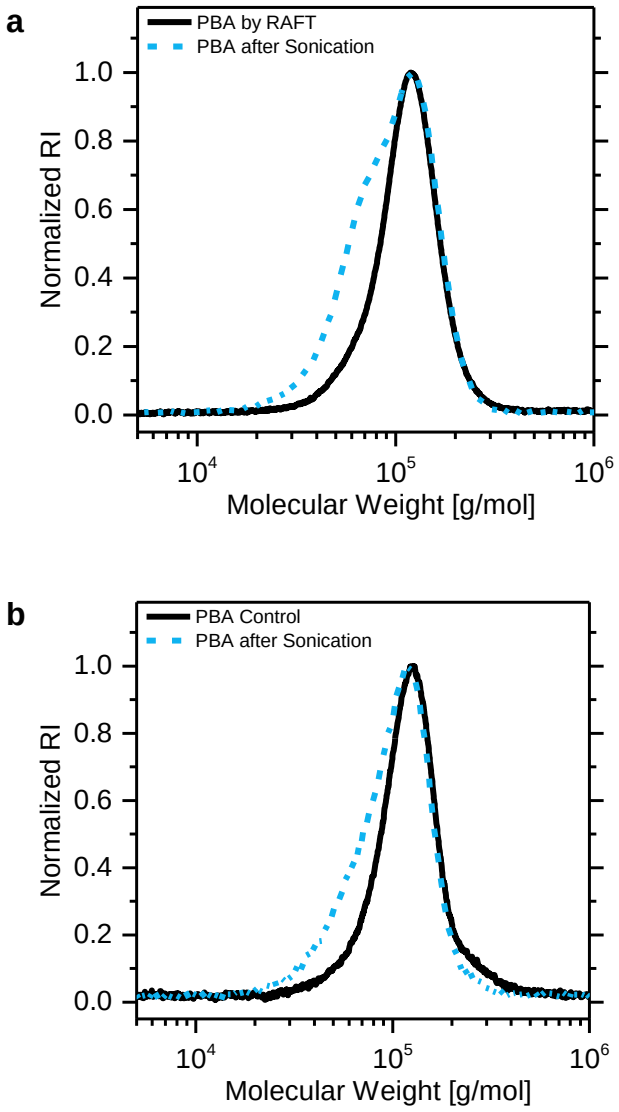

Figure 3.4: **A.** The GPC trace of the mechanophore-containing polymer (107 kDa) showed force-induced cleavage following sonication. **B.** Under the same conditions, the control polymer of similar molecular weight (101 kDa) showed little to no significant changes in response to sonication.

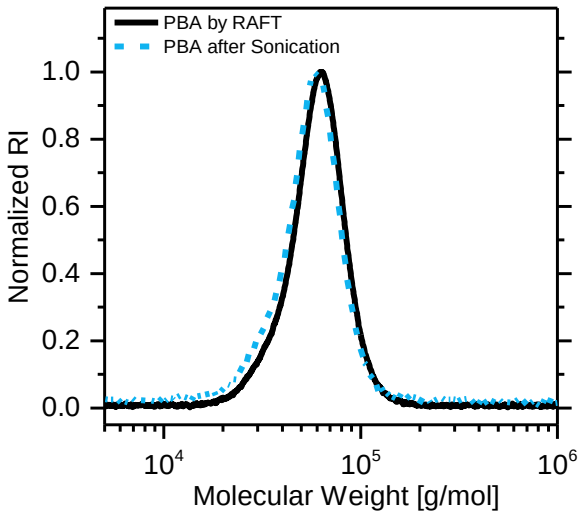

Figure 3.5: A mechanophore-containing polymer of lower molecular weight (54 kDa) showed little to no force-induced cleavage, suggesting that a molecular weight of approximately 100 kDa is required to activate the trithiocarbonate mechanophore.

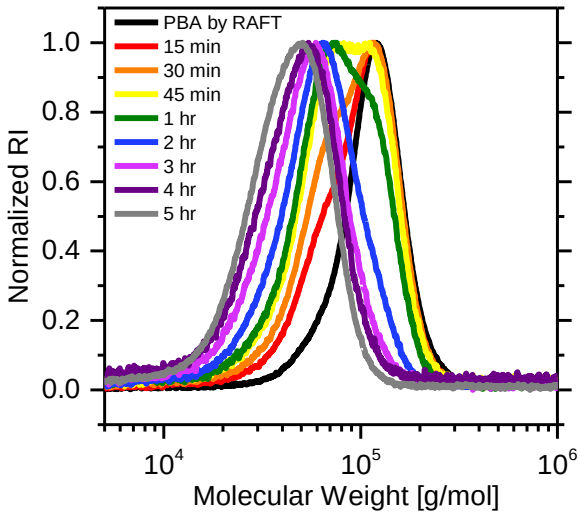

Figure 3.6: Time-evolution of the force-induced cleavage of the mechanophore-containing polymer.

To engineer a healing, responsive material system, the cleavage of the mechanophore is coupled to a subsequent polymerization reaction to significantly alter the bulk properties of the material. This was accomplished by incorporating diacrylates into the polymer solution, which are capable of reacting with the resultant radicals to form a crosslinked network. Polymer solutions containing tetraethylene glycol diacrylate (TEGDA, 20 wt%) were sonicated on ice under continuous nitrogen flow, which triggered gel formation within ten minutes following the initial application of stress (Figure 3.7). Moreover, it should be noted that since this mechanophore responds by generating radicals, it can potentially initiate any radical-based polymerization reaction. For example, incorporating the stress-responsive polymer in solution with divinyl ether (triethylene glycol divinyl ether, TEGDVE) and tetra-thiol (pentaerythritol tetra (3-mercaptopropionate), PETMP) monomers, results in gelation via a thiol-ene polymerization after sonication. Overall, these experiments demonstrate the ability of the trithiocarbonate mechanophore to respond constructively to force on an experimentally relevant timescale and using varied radical-based chemistries.

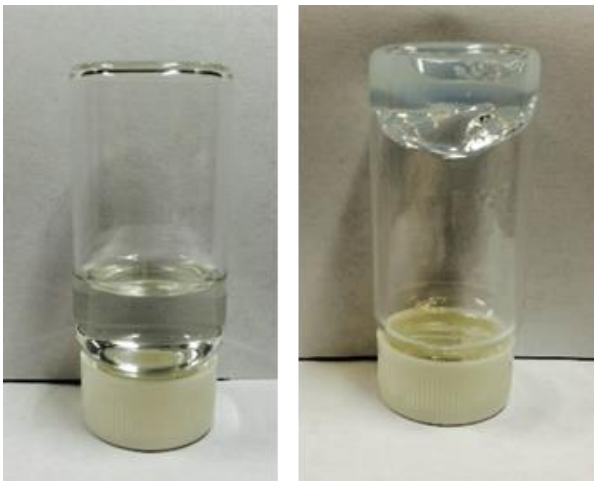

Figure 3.7: The force-induced cleavage of the mechanophore-containing polymer was coupled to a radical polymerization by incorporating tetraethylene glycol diacrylate (20 wt%) in a 10 mL solution of THF containing the polymer (0.5 wt%). Gel formation occurred within 10 minutes from the onset of sonication.

3.4 Summary and Conclusions

In conclusion, we have introduced a novel class of force-responsive polymers containing thiocarbonylthio-based mechanophores. Under the conditions studied here, a molecular weight of 100 kDa is required to cleave the mechanophore. These force-sensitive polymers are capable of initiating a crosslinking, healing polymerization upon application of force on an experimentally relevant timescale. The design of the mechanophore allows for the initiation of any radical-based polymerization reaction, including acrylate and thiol-ene polymerizations. Due to its ease of preparation, this polymer system is readily translated to a variety of self-healing applications, leading to more durable materials.

Chapter 4

THE RHEOLOGY AND MICROSTRUCTURE OF AN AGING THERMOREVERSIBLE COLLOIDAL GEL

This chapter contains results that were accepted for publication in the January 2017 issue of *Journal of Rheology* [75].

4.1 Introduction

Understanding the molecular mechanisms underlying macroscopic bulk property changes in colloidal systems provides fundamental insights that transcend many material systems. While this understanding can be exploited to design new advanced materials, it has direct implications on the stability of a wide variety of colloidal-based consumer products, such as pharmaceuticals, food and personal care items. Macroscopic property changes in non-reacting systems result from external triggers to the system (e.g., stress, temperature, gravity) or from the internal dynamical evolution of the system (e.g., aging). Colloidal gels, in particular, exhibit highly complex behavior arising from their fundamentally disordered microscopic structure. These systems are dynamically arrested and have significantly reduced mobility, which prevent the gel from reaching thermodynamic equilibrium on an experimental timescale [40-42]. This non-equilibrium state often gives rise to aging behavior in which the bulk properties are a function of when the material was first quenched (e.g., via temperature or concentration) and change with gel age [40-42]. As a result, macroscopic properties in aging systems are challenging to measure and predict, but are necessary to determine product shelf-life as well as long-term efficacy and safety.

The process and mechanism by which aging occurs is not well understood; however, it is generally accepted that the aging of colloidal gels is governed by their free energy landscape [43, 76]. The free energy landscape directly corresponds to the microstructure of the system such that measurements of structural evolution during aging can be used to validate simulations [77]. From this perspective, the thermodynamic equilibrium state is located in the deepest well, but other free energy minima do exist. The system samples a reduced set of the available configurational space via thermal motion on the timescale of the experiment, which results in time-dependent bulk properties. As the system continues to evolve, it samples lower and lower free energy minima, approaching the global thermodynamic equilibrium. Here, we explore this view of gel aging as a trajectory in a free energy landscape by examining gel microstructure simultaneous with rheology using advanced Rheo-SANS methods [78].

The phenomenon of aging is of both fundamental importance and industrial relevance. As such, it has been investigated in numerous model systems yet, based on this work, it is important to differentiate between aging in homogeneous gels versus phase-separated gels [35]. (For a comprehensive review of colloidal gels, see reference [79].) One such homogeneous model system is the well-studied adhesive hard sphere (AHS) system, which is employed in this study, and consists of silica nanoparticles grafted with an octadecyl brush dispersed in an organic solvent [27-38]. In this system, particle interactions associated with the steric repulsion of the octadecyl brush are tuned by temperature [39]. This system can be fully rejuvenated by thermal cycling; the gel is heated to its liquid state and sheared using a well-established pre-shear protocol to completely erase its structural history. Indeed, Negi et al. studied the

gelation of similar systems after shear fluidization and shear cessation, but did not measure microstructural evolution [80]. Eberle et al. observed rheological aging in a homogenous AHS gel consisting of octadecyl-coated silica nanoparticles dispersed in tetradecane; the authors reported a steady increase in the storage modulus in time during a constant frequency, small amplitude oscillatory shear (SAOS) experiment and postulated that this may be due to the interdigitation of the octadecyl chains [27]. Similarly, Guo and co-workers observed rheological aging and dynamical heterogeneity in a system composed of octadecyl-grafted silica nanoparticles suspended in decalin [41]. They described late stages of aging with a power law relationship between the storage modulus and waiting time, t_w, ($G' \sim t_w^{0.4}$). Importantly, they observed a time-evolving microstructure as measured by x-ray scattering while the gel formed and subsequently aged, but did not quantitatively connect the structural aging to that of the bulk rheological properties.

A fundamentally distinct model system often employed in aging studies is the colloid-polymer depletion gel. In depletion gels, polymer colloids (e.g., polymethylmethacrylate) are dispersed in an organic solvent and a non-adsorbing polymer is added (e.g., polystyrene), which promotes interparticle attraction through depletion forces [81]. Experimental and simulation work suggest that these phase-separated gels coarsen over time, thereby resulting in colloid-rich regions and colloid-poor voids [44, 82-84]. The phase separation results in time-dependent phenomena, such as the 'delayed sedimentation' that Poon and coworkers observed using dark-field imaging of gels composed of PMMA particles and polystyrene [82]. Similarly, delayed collapse due to continuous coarsening was further quantified in the work of Buscall et al. [83]. Verhaegh et al. argued through small angle light scattering measurements and

optical microscopy that the gelation was driven by spinodal decomposition of the gel [85]. However, the gel continues to restructure over all lengths scales, which leads to continued phase separation that eventually causes the collapse of the gel. Additionally, Zhang and co-workers investigated the dynamics during phase separation and define two regimes of behavior—classical and viscoelastic—which depend on the polymer concentration and interaction length (i.e., polymer-colloid size ratio) [86]. It is important to note that this model system is highly complex, and one such complication arises from the use of shear to homogenize and rejuvenate these gels. Recently, it has been shown that the shear rate influences the resultant structure and mechanical properties of gels composed of PMMA and polystyrene [87]. Currently, the effect of shear on colloidal gels is not well understood [42] and we provide additional insight on this effect by examining the evolution of gel microstructure under shear in a thermoreversible system. Because this system can be fully rejuvenated via thermal cycling, we can compare thermal cycling to the effect of shear, which may appear to rejuvenate mechanical properties, but not fully restore the gel structure.

In the work presented here, we connect rheological aging with structural aging by concurrently measuring the mechanical properties and microstructure of the gel using rheometry and small angle neutron scattering (Rheo-SANS). In particular, we are especially interested in determining if the aging behavior in an AHS colloidal system is consistent with local particle rearrangements or larger, collective rearrangements within the gel by examining the role of shear history and thermal history on gel formation and aging. For this study, an AHS system consisting of 30 nm silica spheres (volume fraction, ϕ=0.28) with an octadecyl grafted brush dispersed in tetradecane was synthesized. We quench the system just slightly below the gel transition temperature

so we can examine aging on an experimentally accessible time scale. At the selected volume fraction, the system is a single-phase, homogeneous gel [27] that does not sediment (Pe_g [gravitational Péclet number] << 1, [88]), avoiding aging behavior associated with gel coarsening or sedimentation that is observed in phase-separated gels [82-84, 89]. The Rheo-SANS data are analyzed to extract quantitative measures of the evolving microstructure during aging and this is shown to be connected to the evolution of the gel's elasticity. The methods and results presented here should be of industrial relevance for studying a wide range of colloidal systems, including paints, concretes, coatings, inks, and pharmaceuticals, which may exhibit aging behavior on commercially-relevant timescales.

4.2 Experimental Methods

4.2.1 Particle Synthesis

The adhesive hard spheres were synthesized by grafting an octadecyl brush onto 30 nm colloidal silica nanoparticles (Ludox TM-50, Sigma Aldrich) according to the procedure developed by van Helden et al. [28] and further developed by Eberle and co-workers [39]. In brief, the silica suspension was treated with sulfuric acid and then mixed and heated in the presence of 1-octadecanol. The mixture was dissolved in ethanol to graft the brush onto the particle surface via a condensation reaction. The particles were purified by washing three times in a 60/40 mixture of chloroform and cyclohexane using a Sorvall RC 6 Plus centrifuge before drying the particles under a nitrogen stream and finally in a vacuum oven overnight. The particles (ρ=1.80 g/mL) were then dispersed in tetradecane (Fisher, ρ(25°C) =0.7670 g/mL, μ(25°C) = 2.078 mPa s, [90]) at a mass fraction of 0.48, which corresponds to a volume fraction of 0.28,

to form a thermoreversible gel. The particles have been characterized extensively using transmission electron microscopy, densitometry, light scattering, rheometry and SANS [27, 39].

4.2.2 Rheometry

Rheological measurements were performed on a stress-controlled Discovery Hybrid Rheometer (DHR) from TA Instruments using cone and plate geometry (40 mm cone diameter, 2° cone angle) equipped with a solvent trap and cover. The temperature was controlled using a Peltier plate with a ramp rate of approximately 7°C/min. The sample was fully rejuvenated between tests by applying a pre-shear protocol, where the sample was sheared at a rate of 10 s^{-1} in its liquid state at 40°C for 2 minutes, and then the sample was held quiescently at 40°C for 2 minutes. Full rejuvenation was confirmed by monitoring the viscosity at the conclusion of the pre-shear protocol. All aging experiments were performed at 28.6°C where the sample is a soft gel capable of flowing homogeneously (i.e., without phase separation or shear banding). Two distinct temperature profiles were used to approach this temperature: 1) quenching from 40°C to 28.6°C (the cooling direction) and 2) quenching from 40°C to 25°C, and then immediately ramping to 28.6°C (the heating direction). Aging experiments were performed within the linear viscoelastic region for the gel at 0.1% strain and 1 Hz. Prior work on this system showed no evidence of shear banding or wall slip [36]. With a solvent trap, the material was stable for approximately 10 days. We note that the gravitational Péclet number, which compares the time scale of diffusion to the time scale associated with sedimentation, is of order 10^{-5}, such that gravitational sedimentation can be neglected [88]. The Péclet number for the small amplitude oscillatory shear

experiments is of order 10^{-4} while the maximum Péclet number during the shearing at 40°C is also of order 10^{-4}, such that inertial effects are negligible.

4.2.3 Rheo-SANS

Simultaneous rheology and small angle neutron scattering (Rheo-SANS) measurements were conducted at the National Institute of Standards and Technology (NIST) Center for Neutron Research (NCNR) in Gaithersburg, MD using the Rheo-SANS sample environment [91]. The sample was loaded in a titanium concentric cylinder geometry with an inner bob diameter of 29 mm and a 0.5 mm gap on an Anton Paar MCR-501 stress-controlled rheometer placed into the NG7 30 m beamline. Time-resolved SANS data was collected in the 1, 3-plane at a detector distance of 13 m with a 15 m lens. The total sample path-length was 1 mm. Transmissions ranged from 0.304 to 0.306 throughout the experiments. Temperature control in this system was imperfect due to slow response (ramp rate of approximately 1°C/min) and overshoot, and therefore cannot be directly compared to temperature ramp data collected on the DHR. As a result, the pre-shear protocol was lengthened; samples were sheared at 10 s^{-1} in its liquid state at 40°C for 10 minutes and then held quiescently at 40°C for 2 minutes. When the heating profile was used, samples were quenched from 40°C to 25°C (for a total of 15 minutes, including the quench) before conducting aging experiments at 28.6°C, 0.1% strain and 1 rad/s. The scattering data was analyzed using the SANS reduction software package available from the NCNR in IGOR Pro [92]. Data were fitted to the sticky hard sphere model using the "SmearedPolyCore_SHS" function from the SANS reduction package. Fitting parameters for octadecyl-coated particles are available from the literature [39]. The scattering length density of tetradecane (SLD solvent = -4.4e-07 $Å^{-2}$) was determined from the online NIST scattering length density

calculator. The scattering length density of the shell (SLD shell = -3.9e-07 $Å^{-2}$) was determined by fitting the reference state data. The perturbation parameter, which determines the depth of the square-well potential, was set at $\varepsilon = 0.001$ for all cases.

4.3 Results and Discussion

Concurrent rheometry and time-resolved small angle neutron scattering in an aging gel enables the direct connection between its mechanical property evolution and corresponding microstructure. To obtain mechanistic insight into the causes of the aging behavior, the system was probed by applying varied thermal and shear profiles. In sections 4.3.1 and 4.3.2, we investigated the mechanical property evolution associated with the formation and aging of a thermoreversible colloidal gel. Specifically, a reproducible reference state (comprised of a temperature and time) was established in the continuously aging gel. Stress was applied to the sample 1) once it has aged to the reference state and 2) before it has reached the reference state (i.e., during its formation). In section 4.3.3, we support our interpretation of the rheological properties with microstructural measurements and establish a quantitative relationship between the underlying microstructure and the bulk properties during aging.

4.3.1 Rheology of an Aging Thermoreversible Gel

In an octadecyl-functionalized colloidal silica system, the interparticle attractions are tuned by temperature. The temporal evolution of the storage (G') and loss (G'') moduli are monitored in response to a temperature change as shown in Figure 4.1A. Initially, both moduli are comparable to the instrument's resolution under these test conditions. As the sample is quenched from its liquid state at 40°C to 28.6°C, both moduli increase by several orders of magnitude, which is associated with the formation

of an interacting colloidal gel [27, 35]. Note that the critical gel temperature, corresponding to rigidity percolation, is 28.8°C [93, 94]. After the gel fully forms and the temperature remains constant, the storage and loss moduli continue to increase with time under small amplitude oscillatory shear (SAOS). The continual stiffening of the gel over the experimental timescale is characteristic of rheological aging in these systems [41]. During the gel formation and aging process shown in Figure 4.1A, the storage modulus dominates the loss modulus and undergoes the greatest change. This time evolution was empirically fitted to an error function as follows:

$$\log G' = A + B\ \mathrm{erf}(C(\log t - D)) \tag{4.1}$$

where t is time in seconds, as displayed in Figure 4.1B. The error function was selected as it typically describes such diffusive processes. The induction time from this empirical fit (parameter D) defines a characteristic time for gel formation and is approximately ≈270 seconds. This characteristic time is a convolution of the time associated with the temperature quench and gel formation. This characteristic time quantifies the time scale of gel formation following the temperature quench to 28.6°C and demonstrates that significant gel aging occurs long after initial gel formation. Prior work suggested that this characteristic time can be used to scale gelation kinetics in a similar system [80]. We note that this timescale is observational—i.e., it is not fundamental and provides a physical timescale for the process based on the observation method (SAOS).

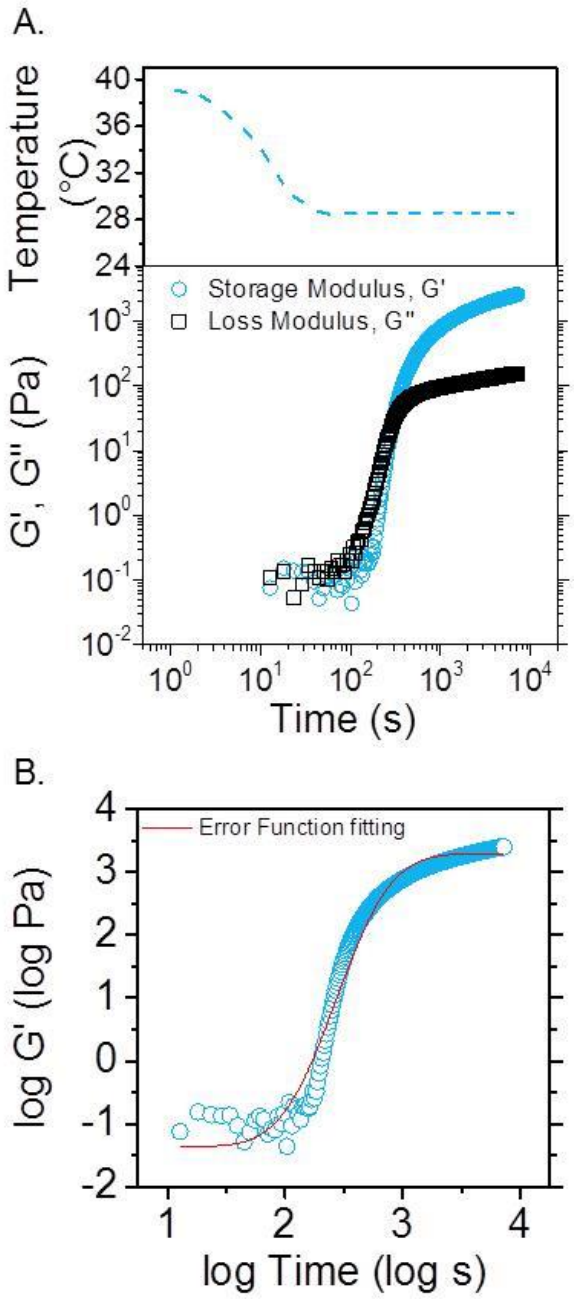

Figure 4.1: The temperature dependence of the storage and loss moduli. **A.** After the gel forms and the temperature remains constant, the sample exhibits rheological aging. **B.** The storage moduli were fit to an error function: log G′= A+ B*erf(C*(log time-D)) where A= 0.97, B=2.33, C=1.91 and D= 2.43. From the fitted D parameter, a characteristic time for gel formation was calculated as approximately 270 seconds.

Small amplitude frequency sweeps for samples quenched from 40°C and subsequently soaked at the desired temperature for 10 min are reported in Figure 2. The experiments were conducted over a period of approximately 4 minutes at 0.1% strain. The thermoreversible gel is very sensitive to temperature and the critical gel temperature is observed to be 28.8°C using the condition established by Winter and Chambon, in which both moduli have identical frequency dependence [93], which is in good agreement with the temperature of 28.7°C reported previously for this system [27]. The data in Figure 4.2 shows that, at this critical gel temperature, G′ and G″ are equal and scale with the $\omega^{0.5}$ over several decades of frequency. Based on this data, all subsequent gel aging studies were conducted at 28.6°C, where the sample is a soft gel capable of flowing homogeneously.

From this SAOS data at the reference temperature of 28.6°C, the relaxation dynamics were quantified by fitting to a model based on mode coupling theory (MCT). This theory describes the behavior exhibited in hard sphere colloidal glasses in which a particle is trapped by neighboring particles, forming a 'cage' which hampers its mobility [95]. This theory is associated with a fast relaxation corresponding to diffusive motion within its cage (β relaxation) and a slower relaxation corresponding to particles escaping from the cage (α relaxation). From MCT, the following expression for the storage and loss moduli were developed [96] and adapted for soft particles [97]:

$$G'(\omega) = G_p + G_\sigma \left[\Gamma(1-a')\cos\left(\frac{\pi a'}{2}\right)(\omega t_\beta)^{a'} - B\Gamma(1+b')\cos\left(\frac{\pi b'}{2}\right)(\omega t_\beta)^{-b'}\right] \quad (4.2)$$

$$G''(\omega) = G_\sigma \left[\Gamma(1-a')\sin\left(\frac{\pi a'}{2}\right)(\omega t_\beta)^{a'} + B\Gamma(1+b')\sin\left(\frac{\pi b'}{2}\right)(\omega t_\beta)^{-b'}\right] + n'_\infty \omega \quad (4.3)$$

where G_p is the plateau modulus, G_σ is the viscoelastic amplitude, t_β is the β relaxation time and n'_∞ is the high-frequency viscosity. In the absence of a more appropriate theory for adhesive hard spheres, equations 1 and 2 were fitted to the linear viscoelastic

spectrum at 28.6°C using mode coupling parameters a′=0.301, b′=0.545 and B=0.963, which are recommended for ideal hard spheres [98] (see Figure 4.2). Following this procedure, the beta relaxation time was determined to be 1.1 s. The beta relaxation time corresponds to diffusive motion within the cage, and is representative of the time required for local bond rearrangement between neighboring particles. Meanwhile, the alpha time is the time required for the gel to flow microscopically and is extrapolated from the model to be of order ~100 s at 28.6°C.

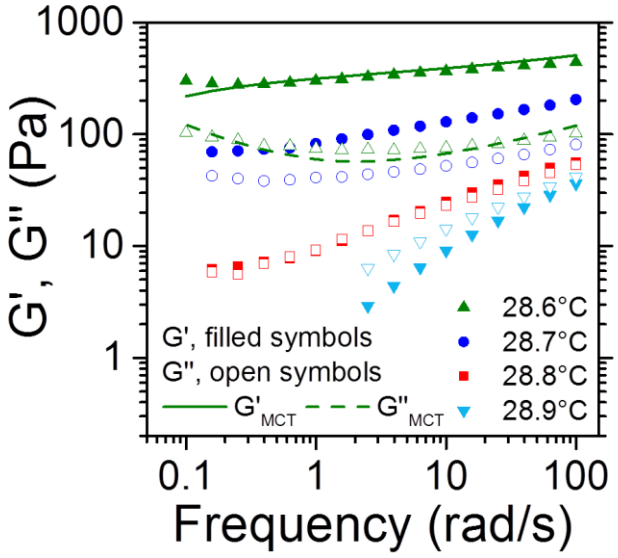

Figure 4.2: Frequency sweeps at 0.1% strain as a function of temperature. Following the Winter and Chambon criteria, the gel transition temperature is at 28.8°C. All tests were conducted at 28.6°C where the gel is capable of flowing homogeneously. The MCT model fit of G′ (solid line) and G″ (dashed line) reveals a β relaxation time of 1.1 s.

By investigating two different thermal profiles, a reproducible reference state for studying aging in this thermoreversible gel was established. The thermal profiles described earlier briefly consist of 1) directly quenching from the liquid state at 40°C to

28.6°C (i.e., the cooling direction) or 2) quenching from 40°C to 25°C to 28.6°C (i.e., the heating direction). The two different thermal profiles and the corresponding mechanical properties are shown in Figure 4.3A. The G′ cooling and heating direction curves converge after 4250 seconds, where the storage moduli are within 2% of each other. Therefore, 4250 seconds and 28.6°C was established as the reference state for both quenching protocols. This reference state is approximately 15 times longer than the characteristic time of gel formation described above. At longer times (from the reference state to the conclusion of the two hour experiment), G′ scales with $t^{0.4}$, which agrees with the results for a similar system as reported by Guo et al. [41]. Our results indicate that this scaling is independent of the thermal history during gel formation. Importantly, the approach to the reference state is highly reproducible, as shown in Figure 4.3B. This data set represents one sample, which was fully rejuvenated by heating to a liquid state and shearing at 40°C between trials; however, slight variability is observed owing to batch-to-batch variation and sample loading.

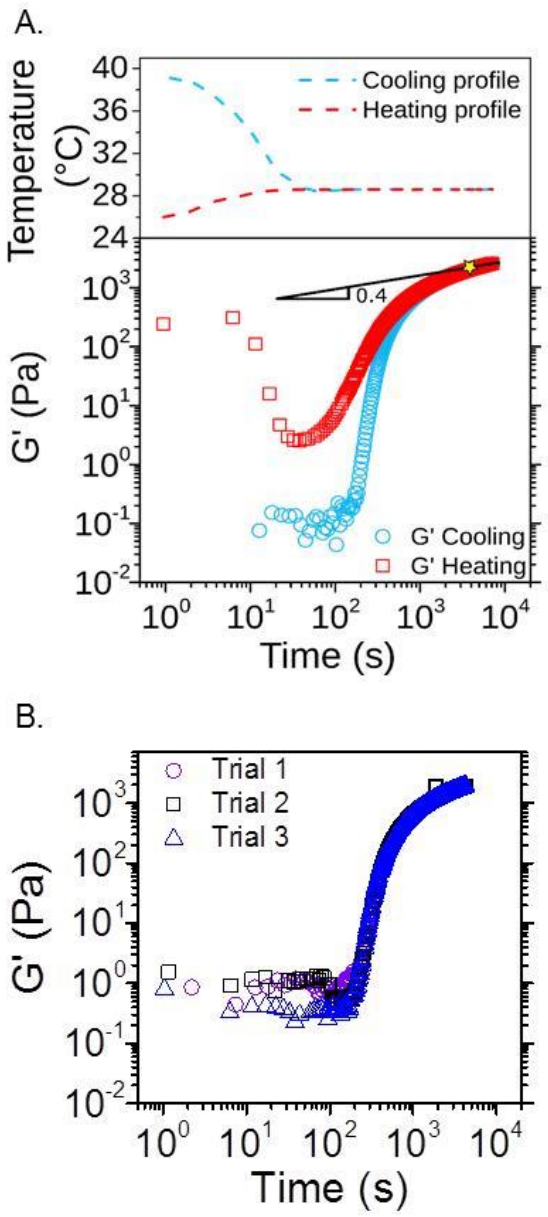

Figure 4.3: Determination and reproducibility of a reference state during gel aging. **A.** Temperature profiles and corresponding evolution of the storage and loss moduli. The reference state is denoted by a yellow star and represents the convergence point of the storage moduli from both the heating and cooling directions. At long times, $G' \sim t^{0.4}$, which agrees with the results reported by Guo et al. and is independent of the thermal history during gel formation [41]. **B.** The approach to the reference state is reproducible. The sample was thermally recycled between trials.

4.3.2 Nonlinear Rheology of an Aging Thermoreversible Gel

4.3.2.1 Application of Stress to an Aged Gel

The nonlinear rheological response of gels elicited by applying increased levels of shear stress provides insight into the underlying structural dynamics during the gel formation and aging process. Rheological measurements were performed after the sample was aged to its reference state of 28.6°C. After the reference state was reached, creep tests were performed by immediately applying stress to the specimen. The response of the material to different stresses of 25 Pa, 40 Pa, 50 Pa, and 65 Pa was evaluated, where the specimen was rejuvenated and aged before each stress was implemented. The gel responses are displayed in Figure 4.4A. In all experiments, creep ringing is observed. These short-time oscillations in strain are observed due to the rheometer inertia, and are therefore expected for a viscoelastic gel tested on a stress-controlled rheometer [99]. At 65 Pa, the sample yields during the experiment. There is a delay of approximately 2 minutes before the onset of flow where stress-driven rearrangements may occur prior to yielding. Identical experiments were performed using the same specimen that was thermally recycled and reformed from the heating direction (Figure 4.4B). Similar responses were observed for both heating and cooling directions, further confirming that the behavior under stress in the aged gel is independent of its thermal history.

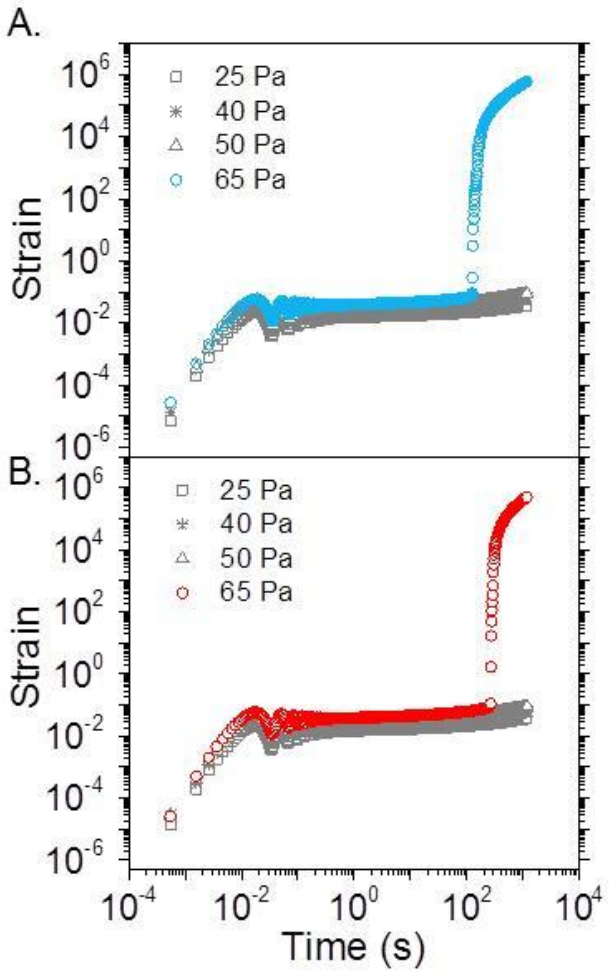

Figure 4.4: Effect of shear stress on aged gels formed from **(A)** the cooling profile (from 40°C to 28.6°C) and **(B)** from the heating profile (from 25°C to 28.6°C). Creep ringing is observed for all tests, and yielding occurred after 65 Pa was applied. The delay before yielding may indicate stress-induced structural rearrangements in the gel microstructure. Together, these results indicate that the gel response to shear stress in the aged state is independent of its thermal history during gel formation. All data sets were collected from the same specimen that was thermally rejuvenated at 40°C between trials.

Aging in these colloidal gels was further evaluated by interrupting an aging specimen via an applied stress and assessing the impact on the modulus. The specimen

was initially thermally rejuvenated and then G′ was monitored using SAOS while the sample aged to the reference state of 4250 seconds at 28.6°C (from the cooling protocol, similar to Figure 4.3B). A 20 minute creep test was then immediately performed by applying a stress of 0, 25, 40, 50, and 65 Pa. The samples were permitted to recover for 20 additional minutes and the modulus was subsequently monitored using SAOS. No substantial changes in G′ are observed at stress values of 50 Pa and lower. However, for the experiment at 65 Pa, yielding was noted (Figure 4.4A) and the aging trajectory was considerably altered. In particular, using G′ values to quantify gel "age," the results presented in Figure 4.5 indicate that the age was reduced by approximately one half after applying 65 Pa. To analyze the post-stress aging further, longer aging studies are presented and interpreted in conjunction with the results of the next study, which are discussed at the end of section 4.3.2.2 (see Figure 4.7).

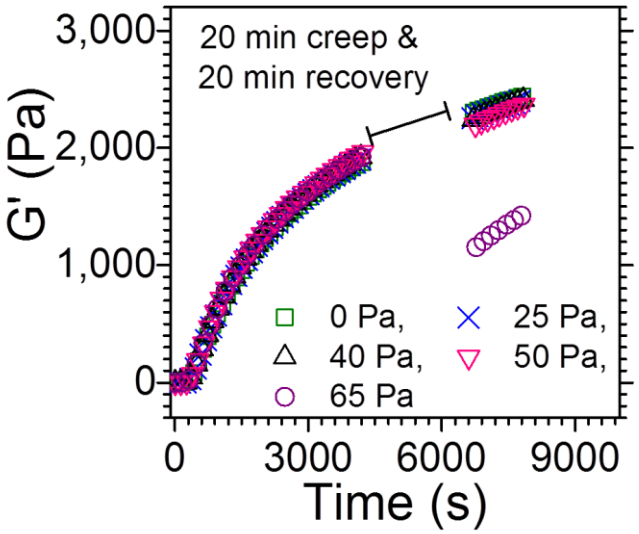

Figure 4.5: The aging trajectory of one sample that was thermally recycled between tests. In each test, the sample was aged to the reference state of 4250 seconds and shear stresses of 0 Pa, 25 Pa, 40 Pa, 50 Pa and 65 Pa were applied for 20 minutes. The samples recovered for 20 minutes, and aging was monitored for an additional 20 minutes.

4.3.2.2 Application of Stress during Gel Formation

To further explore the stress response of the colloidal gel, stress was applied during gel formation (whereas in the previous section, stress was applied *after* gel formation). Specifically, oscillatory shear stresses of 25 Pa or 40 Pa were applied at 1 Hz until the reference state was reached (at 4250 seconds), followed by SAOS measurements at 0.1% strain and 1 Hz to monitor subsequent structure formation. Gel formation was hindered or suppressed for oscillatory stresses of both 25 and 40 Pa, respectively, as shown in Figure 4.6 (the 0 Pa continuous SAOS measurement is shown for comparison). While these lower stresses (i.e., < 65 Pa) were insufficient to affect the modulus *after* gel formation (i.e., see Figure 4.5), the presence of these stresses *during* gel formation significantly affects the formation evolution. In the 40 Pa case, where bulk property measurements indicate that macroscopic gel formation is suppressed under the applied stress, a very rapid rate of G′ evolution is observed when the stress was released. This suggests that some structure was formed in the sample under the applied flow as gel formation occurs more rapidly when the stress was removed.

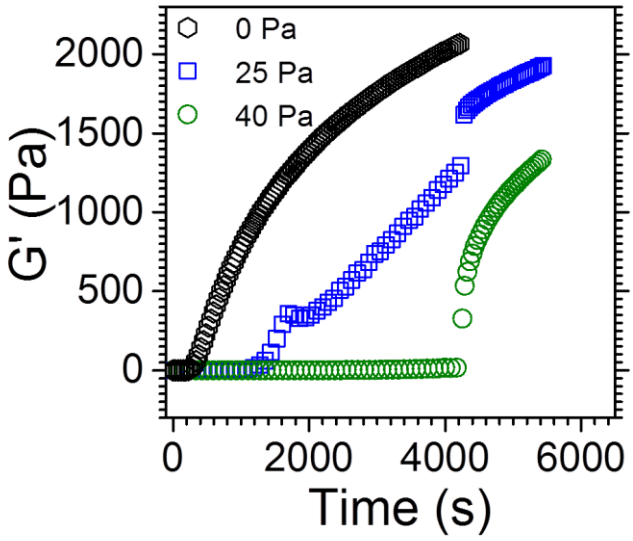

Figure 4.6: Oscillatory stress applied during gel formation. In each test, the sample was aged to 4250 s, which corresponds to the reference state of the unstressed gels, under oscillatory stresses of 25 Pa and 40 Pa. (The corresponding strain amplitude values under oscillation ranged from 1033% to 1.84% for the 25 Pa experiment and from 1638% to 64.8% for the 40 Pa experiment.) The stress was then released and gel formation was monitored. All measurements were performed at 1 Hz. In the 40 Pa case, bulk property measurements indicate that gel formation was prevented, yet there is a substantial increase in the rate of G′ evolution when compared to the 0 Pa reference case (i.e., 0.1% stain, 1 Hz frequency SAOS experiment), suggesting that the gel microstructure evolved under shear.

The relatively rapid increase in G′ upon cessation of stress as compared to the trial where no stress was applied suggests that the gel microstructure evolved with time under the applied stress, yet we note the same long-term aging behavior in these samples. This effect is evident in Figure 4.7 where the 40 Pa oscillatory stress data set has been translated in time only to overlay on the 0 Pa curve. Moreover, longer aging experiments following the application of 65 Pa creep test at the reference state were

conducted, which show the same long-time behavior (Figure 4.7). Specifically, for all three data sets, after the reference state is reached at 4250 seconds, G′ scales with $t^{0.4}$, which is consistent with the aging behavior in Figure 4.3 and in the work of Guo *et al*. Consequently, these results show that the gel microstructure evolved under shear and the gel eventually ages following similar mechanism of aging as unstressed gels. Thus, gels prepared under different shear conditions in this study will converge to the same long-term behavior. This is further corroborated by microstructural measurements, which are discussed in the following section.

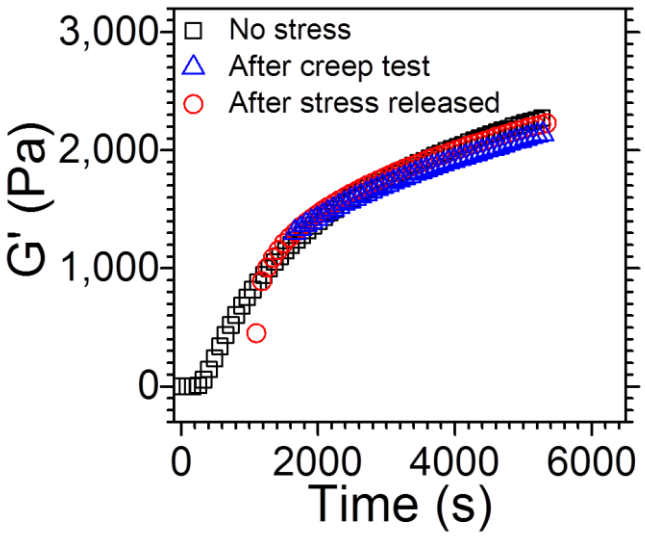

Figure 4.7: Long-time aging experiments. Data sets shown are (1) “no stress” case where the sample ages under SAOS, (2) “after creep test” case where the gel was subjected to a 20 minute 65 Pa creep tests followed by a 20 minute recovery period prior to aging under SAOS and (3) “after stress released” case where 40 Pa stress was applied to the gel during its formation, and subsequent aging was measured under SAOS after the stress was removed. Time was shifted backwards by 4985 s and 3150 s for the “after creep test” and “after stress released” experiments, respectively to show the same behavior.

4.3.3 Microstructural Measurements

Time-resolved Rheo-SANS experiments were conducted to track the evolution of gel microstructure in samples subjected to varied thermal and stress histories. The aging of the specimens was first evaluated in the absence of shear from the cooling and heating direction (Figures 4.8A and 4.8B, respectively). In the cooling direction, the sample initially had a liquid-like microstructure that evolved to a microstructure expected for a homogeneous gel [27, 35]. In contrast, gel-like microstructure was initially observed in the heating direction and rapidly evolved to a state consistent with a warmer gel upon heating. The scattering data from the cooling direction are consistent with the particles gradually sampling lower energy states as the gel forms and ages. Moreover, the scattering data collected from the gel formed from the heating direction indicate that the particles sample fewer states as compared to the gel formed from the cooling direction. This observation is consistent with particles attempting to escape from a deeper energy well achieved by undercooling, and is consistent with the free energy viewpoint of colloidal gel aging.

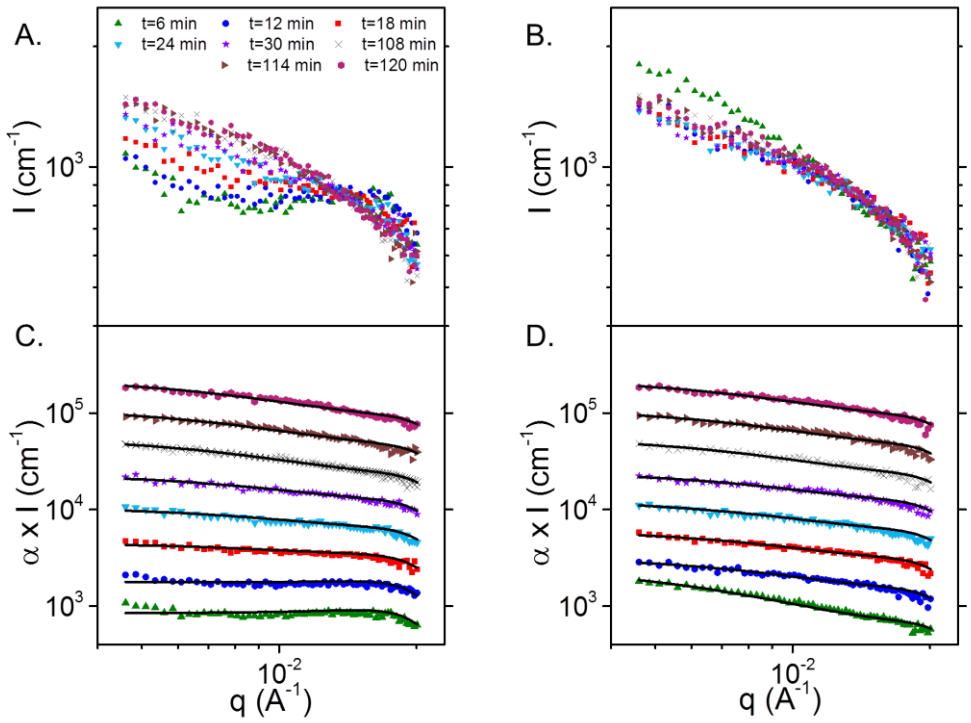

Figure 4.8: Time-resolved small angle neutron scattering (SANS) data during a two-hour aging experiment. Samples were quenched from the **(A)** cooling direction and **(B)** heating direction. The data were fit to the sticky hard sphere model for the **(C)** cooling direction and **(D)** heating direction. Each subsequent set of intensities was doubled (multiplied by the constant α) from the previous data set to clearly show the fits. Note: the time-resolved data are binned every six minutes and shown on logarithmic scales.

To provide a single parameter quantifying the structure, the scattering data were successfully fitted to a liquid state theory model based on the sticky hard sphere (SHS) model (or Baxter model), which is first introduced in Chapter 1. The Baxter parameter so obtained provides a single parameter (τ, which quantifies the strength of attraction between particles) that can be used to track how the gel forms and ages, which can be further used to develop a relationship between the microstructure in the gel and

corresponding bulk properties. Note that the structures formed from quenching into the gel state are not equilibrium states and instead, represent states along an aging trajectory. As such, the Baxter parameters derived from these fits are 'effective' parameters and will converge to the true Baxter parameter for a given temperature as the structure ages. The fitted results are displayed in Figure 4.8C and 4.8D for the cooling and heating data, respectively. Note that scattering curves are displaced in intensity by doubling the intensity sequentially for clarity. Except for the Baxter fit parameter, all other model parameters for octadecyl-coated particles are available from the literature [39] and these parameters are described in the materials and methods section.

To quantify the evolving microstructure in the gel, we introduce λ as the order parameter of the aging structure, which is defined as follows:

$$\lambda = \frac{\tau_{40}^{eq} - \tau^{eff}}{\tau_{40}^{eq} - \tau_{\infty}} \tag{4.4}$$

where τ_{40}^{eq} is the value of the Baxter parameter in the liquid state at 40°C, τ^{eff} is the value of Baxter fit parameter at each time point and τ_{∞} is the long-time equilibrium Baxter parameter in the gel. By fitting the SHS model to time-resolved SANS data as described above, τ_{40}^{eq}= 0.623 and τ_{∞} ≈0.245.

The evolution of λ in time is displayed in Figures 4.9A and 4.9B along with the corresponding storage modulus at the specified time intervals for both the cooling and heating profiles, respectively. Importantly, the monotonic increase in G′ is matched by a monotonic increase in λ (i.e., *aging toward equilibrium*). Further, this quantitative analysis demonstrates that a specific elastic modulus corresponds to a specific microstructure, which is independent of the sample's thermal history (Figure 4.9C). By

plotting $\log G'$ vs. λ for each aging trajectory and, observing an approximately quadratic relationship, we obtain the empirical expression:

$$\log G' = -90.99\,\lambda^2 + 188.16\,\lambda - 94.17 \quad (4.5)$$

which was fit to both quenching profiles, as shown in Figure 4.9C. Thus, aging due to local rearrangements leads to microstructures monotonically evolving along a trajectory of ever stronger interactions. This analysis, which is the first of its kind for aging colloidal gels, is consistent with the viewpoint of aging as a trajectory in the free energy landscape, where the microstructure is observed to evolve smoothly towards an equilibrium state with time. Note that aging in polymers is often characterized by a 'fictive' temperature, while previous work on colloids has suggested that aging can result from a time-dependent pair potential (see Guo et al. for a discussion [41]). Our analysis does not support a time-dependent potential, but rather, is a consequence of sampling ever lower free energy states as the sample evolves towards its equilibrium microstructure at a given quench temperature. The structure order parameter is therefore more analogous to the fictive temperature concept invoked for homogenous aging in polymer and colloidal glasses [100]. Moreover, the overshoot of the order parameter in Figure 4.9B is similar to Kovacs memory effect, which is observed in aging glasses subjected to non-monotonic temperature profiles, and strengthens the case for a connection between λ and the fictive temperature [101].

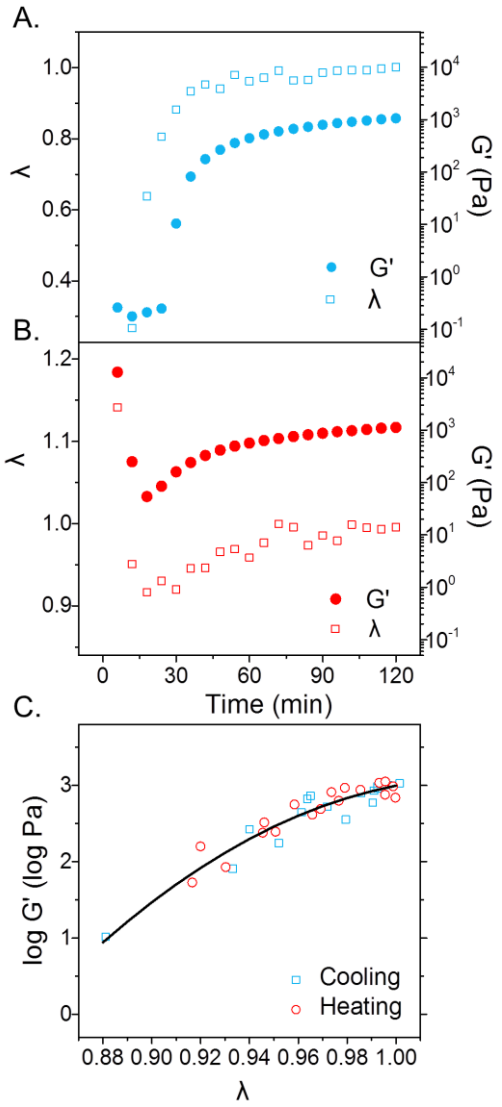

Figure 4.9: Time-resolved Rheo-SANs measurements. The evolution of the structural parameter λ and G′ as a function of time are shown from the **(A)** cooling direction and **(B)** heating direction. The structural parameter λ was determined from Equation 3 after fitting the sticky hard sphere model to the scattering data at each time point. The plotted value of G′ is an average value of the storage modulus determined from SAOS measurements during the indicated six minute interval. **(C)** The microstructure and storage modulus show a one-to-one correspondence, which is independent of the thermal profile during gel formation. The storage modulus and particle interactions are related by equation 4.5 over the range of approximately 0.88 to 1.

Microstructural measurements also confirm the choice of reference state, which is consistent with the one-to-one relationship between G′ and microstructure discussed previously. As shown in Figure 4.10, the scattering data at the reference state for gels quenched from the heating and cooling direction are nearly identical. Both structures are successfully fit to the liquid state theory for a homogeneous AHS colloidal suspension. The λ values of 0.964 and 0.996 for the cooling and heating direction respectively are well above the critical value for phase separation. Thus, this result shows that the gel is homogeneous on the particle length scale and the particle interactions are very short-ranged.

To better understand the mechanism by which the system reaches the homogeneous reference state and continues to age, we analyze the mechanical response using mode coupling theory (MCT) to determine the nature of the local particle motion. Within the context of mode coupling theory, the characteristic localization length is the mean-squared displacement associated with local particle motion. Mode coupling theory provides a scaling for homogeneous gels as follows:

$$\frac{G'a^3}{k_BT} = 0.29\frac{\phi a^2}{r_{loc}^2} \tag{4.6}$$

where r_{loc} is the localization length and a is the particle radius [102]. Using the G′ value corresponding to the reference state of 4250 seconds at 1 Hz reported in Figure 4.3, r_{loc} was calculated as 3.3 nm. This localization length is on the order of the brush size (reported to be 2.76 nm by Eberle et al. [39]). Thus, particles are bound by contact forces and the elasticity arises from thermal motion on the length scale of the coating responsible for this attraction. This result is consistent with local particle rearrangements as the mechanism of aging. We note that prior researchers studying a similar thermoreversible system observed quantitatively similar localization

lengths [37]. The localization length is much larger in repulsive glasses and in depletion gels [79], where the localization length is on the order of the size of the dense, phase-separating clusters [103]. This result strongly supports local particle rearrangements occurring throughout the homogeneous gel as the mechanism of aging.

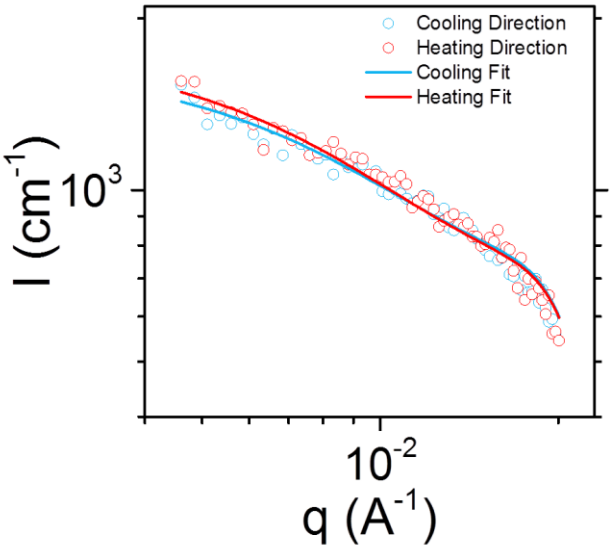

Figure 4.10: At the reference state, the microstructures of the gels are nearly identical and are independent of the temperature profile during formation. Both data sets are fit to liquid state theory with λ values of 0.964 and 0.996 for the cooling and heating direction, respectively. Data are shown on logarithmic scales.

Importantly, this analysis suggests that local particle rearrangements and motion are responsible for the mechanical and structural aging under thermal quench. This is clearly distinct from the mechanisms identified in phase separating colloidal gels, where a sequence of particle surface migration, caging, and sequestration in a dense glassy solid have been proposed based on large-scale simulations (see, for example, Zia, Landrum and Russel [27]). Questions remain, however, if this mechanism of local

rearrangement extends to aging under an applied shear stress. We extend the study of the gel's stress response by obtaining time-resolved microstructural and rheological measurements while applying oscillatory stress during gel formation by quenching from 40°C. The time-resolved scattering data were binned into 3.5 minute intervals; the first bin and last bin (corresponding to the first 3.5 minutes and the last 3.5 minutes of the 4250 second experiment, respectively) are displayed in Figure 4.11A with open and closed symbols, respectively. The initial structures are similar and liquid-like, with a correspondingly lower λ values. The microstructures after quenching under stress are characteristic of that of a gel and qualitatively very similar to that observed for purely thermal quenching. Gel formation was observed under oscillatory stresses of 0 Pa, 10 Pa, and 40 Pa. After the stress was released at 4250 s, the initial G′ values in these gels were lower than the initial G′ value in the unstressed gel (0 Pa), yet the bulk properties in these stressed gels evolved at a faster rate (Figure 4.11B). Using the relationship developed above quantitatively connecting G′ to λ, similar initial mechanical properties were predicted (x markers in Figure 4.11B) based on λ values from microstructural measurements collected during the final 3.5 minutes of the experiment. The discrepancy between the predicted and measured G′ values may be due to both measurement noise from the SANS data collected over short times and expected run-to-run variability. Similarly, from the measured G′ values in Figure 4.11B, corresponding values of λ were calculated, and these predicted fits are indistinguishable from the fit data plotted in Figure 4.11A. Note that this data are slightly different from that reported in Figure 4.6 because of differences in the thermal properties of the Rheo-SANS gas-cooled Couette sample environment as compared to the performance of the DHR rheometer with a cone and plate geometry and Peltier. Nevertheless, this sequence of experiments shows that

the gel structure evolves under shear in a manner similar to thermal quenching for these homogeneous gels. In this work, we have not tested very large values of the inverse Bingham number, M′, such that shear would fundamentally disrupt the gel, as done previously for this system [104]. In other systems where there are substantial heterogeneities in structure and/or dynamics, and where shear may densify the structure, the complex shear history dependence of the microstructure could be expected to lead to a shear history dependence of the mechanical properties that is not equivalent to thermal rejuvenation [105]. We do not observe such effects in our system under the conditions explored.

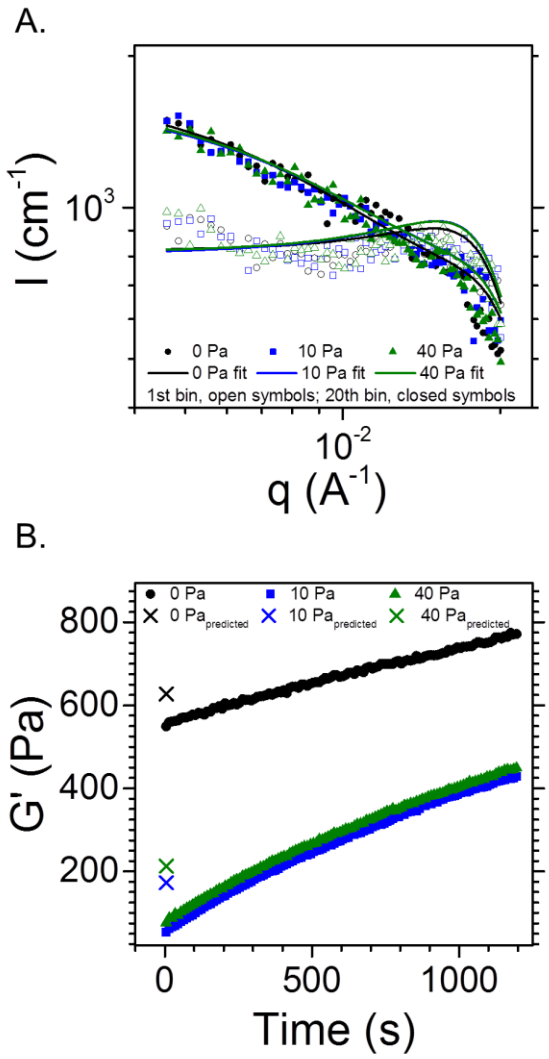

Figure 4.11: Microstructure and rheology corresponding to a gel quenched under stress. **A.** Time-resolved SANS data were binned into 3.5 minute intervals; the first and last bin corresponds to open and closed symbols, respectively. The microstructure evolved under stress. (The values for the structural parameter λ are as follows: $\lambda_{initial,\ 0\ Pa} \approx 0$, $\lambda_{final,\ 0\ Pa} = 0.976$, $\lambda_{initial,\ 10\ Pa} \approx 0$, $\lambda_{final,\ 10\ Pa} = 0.937$, $\lambda_{initial,\ 40\ Pa} \approx 0$ and $\lambda_{final,\ 40\ Pa} = 0.942$.) Data are shown on logarithmic scales. **B.** Immediately after the stress was released, the initial G′ values were lower in the stressed gels when compared to the unstressed gel (0 Pa), yet the bulk properties in the stressed gels evolved at a faster rate, thereby demonstrating that shear influences how the gel ages.

4.4 Summary and Conclusions

In conclusion, we quantitatively relate the bulk rheological properties to the underlying microstructure in an aging, homogeneous, thermoreversible AHS colloidal gel and find a unique, quantitative relationship irrespective of thermal or shear history over the range of parameters explored. By combining rheology and time-resolved small angle neutron scattering, a reproducible reference state in the continuously aging colloidal gel is established from which stress is applied to probe the gel's response. The rheological behavior after application of stress 1) during gel formation and 2) during gel aging led us to hypothesize that the gel's microstructure develops while under shear during thermal quenching, which is further confirmed by direct microstructural measurements.

The modeling and analysis of concurrent rheological and microstructural measurements provide insight about the colloidal-level motions and interactions responsible for aging. An empirical relationship is developed between an order parameter, which characterizes the distance from equilibrium as determined from scattering measurements of the structure, and the macroscopic property of elastic modulus during gel aging. This empirical relationship enables predicting properties of other rheological experiments from microstructure measurements. For example, we demonstrate that a specific elastic modulus corresponds to a given microstructure, such that the rheological state for a given microstructure is independent of the thermal and shear history of the gel that yielded the given microstructure. Moreover, while the specific microstructure at a given time is dependent on the sample's history, once at a particular microstructure, the sample will quiescently age along the same trajectory regardless of history.

Analysis of the elastic modulus at the reference state with mode coupling theory yields a characteristic localization length of 3.3 nm in the gel, which is comparable to the interaction length between particles in the homogeneous gel. This result is consistent with local particle rearrangements as the mechanism of rheological aging. Indeed SANS measurements of the gel structure confirm that the sample ages homogeneously, and therefore, ages by a mechanism distinct from that observed for phase-separating colloidal gels (e.g., see [44]).

Overall, this work expands our understanding of colloidal gel aging by establishing a quantitative, predictive relationship between the underlying microstructure and bulk mechanical properties, and is consistent with local particle rearrangements as the mechanism of rheological aging. The measurements and analysis support that aging is a trajectory in the free energy landscape, and can ultimately be used to further test and confirm this viewpoint through computational studies. The results of this study may be industrially relevant to products that age on commercially-relevant timescales, such as foods, paints and pharmaceuticals. The approach may also be applicable to other arrested systems, such as metallic glasses, which have been observed to age rheologically in a manner similar to colloidal systems in some respects [106, 107]. Moreover, it is has been suggested that colloids can serve as surrogates for atomic and molecular systems [25, 26]. In particular, the larger size scale of colloidal systems and tunable particle interactions allow for direct measurement of local microstructure and manipulation, respectively, thereby furthering the understanding of complex condensed matter systems and aiding in the design of advanced materials.

Chapter 5

STRUCTURAL AND RHEOLOGICAL AGING IN MODEL ATTRACTION-DRIVEN GLASSES

5.1 Introduction

The study of out-of-equilibrium systems is of fundamental scientific interest and industrial applicability, and, as such, characterizing and controlling these systems is considered by the Department of Energy as one of the five grand challenges facing scientists today [108]. Colloidal dispersions are usually out-of-equilibrium systems that are of particular relevance as they are found in a wide variety of natural and synthetic consumer products, such as foods, pharmaceuticals, paints and cosmetics [109]. Moreover, colloidal dispersions are often employed as model systems to probe and understand non-equilibrium behavior in other systems of interest, such as atomic or molecular systems, because colloidal dispersions have more experimentally accessible length scales and time scales [110]. In particular, the size scale of colloidal particles allows for the tracking of their motion using microscopy. Additionally, the use of colloidal glasses to understand behavior in structural glasses is particularly advantageous as the volume fraction can be easily altered in colloidal glasses, while the effects of density and temperature are coupled in molecular glasses [111]. Furthermore, the tunable interactions between colloidal particles and ability to purchase or synthesize particles of varying shapes and sizes also contribute to their utility as models to understand other condensed matter systems.

Aging phenomena are observed in many types of glassy colloidal dispersions [109, 112]. Specifically, colloidal dispersions are typically in dynamically arrested states with significantly hindered mobility, which prevents the system from reaching thermodynamic equilibrium on experimental time scales [40-42, 109]. However, sufficient thermal mobility is preserved such that system continues evolving toward thermodynamic equilibrium. As a direct consequence, aging phenomenon is observed in many types of colloidal gels and glasses as time-dependent properties. For example, experiments and simulations probe aging behavior in model colloidal glass systems such as Laponite [111, 113-116], star polymers [117, 118] and colloid-polymer mixtures [119-121]. In this context, the "age" of the sample refers to the time elapsed since the material was rejuvenated. Rejuvenation is a mechanical or thermal process that erases the structural history of the sample before a new test is conducted. Typically, as the sample ages, the rate of aging decreases and the relaxation time of the material increases [112]. This time-dependent behavior complicates the characterization of these aging systems, which is required to accurately report, control and predict product stability, shelf-life and safety.

Importantly, the molecular mechanism underlying the aging process is specific to the evolution of microstructure in the system. Stiakakis et al. used multispeckle dynamic light scattering (MSDLS) and small angle neutron scattering (SANS) to determine that multi-arm star polymer glasses age via crystallization, which resulted in an increased rate of the short-time diffusion [122]. Pham and coworkers mapped the transition from a repulsive to attractive glass in a depletion glass and noted aging effects in all non-crystallizing samples; static light scattering was used to probe the underlying structure yet, within the attractive glasses samples of varied attraction strength,

structural changes could not be resolved [119]. To correlate the dynamics to structure during aging, Cianci et al. use a glassy system composed of poly(methyl methacrylate) (PMMA) colloids in a mixture of decalin and cyclohexylbromide and monitored the real-time motion using confocal microscopy [123]. While they did not determine a mechanism, their results suggest a correlation between structure and dynamics during aging; tetrahedra that were categorized as "looser" and more "irregular" led to enhanced mobility that facilitated the aging process. Moreover, computer simulations of aging attractive colloidal glasses conducted by the Cates group showed that the number of bonds per particle increased as the system aged, resulting in a stiffer network that relaxed more slowly [124]. Overall, these results highlight the complex behavior associated with aging in colloidal glasses, and emphasize the utility in uncovering its mechanistic origin and exploring its structural evolution.

Applied stress may alter the aging process, and these results are typically interpreted in the context of the free energy landscape viewpoint of colloidal aging. Briefly, this viewpoint describes a complex landscape of free energy states in which the system continuously evolves toward lower free energy states via thermal motion as the system ages and approaches thermodynamic equilibrium [43, 76, 125]. Viasnoff et al. experimentally demonstrated the nontrivial effect of shear in a colloidal glass [126]. Specifically, their experiments measuring the relaxation dynamics in a glassy suspension of polybeads indicated that high shear and low shear led to rejuvenation and "overaging," respectively, where "overaging" refers to accelerated aging. On a microscopic level, they proposed that high strains destabilized the system, while moderate strains enabled the sample to explore more stable configurations. Lacks and Osborne corroborated the experimental results of Viasnoff et al. through molecular

simulations [77]. Using an energy landscape framework, they reported that a cycle of large strain rejuvenated the glass while a small strain overaged it; shear "shuffled" the system to shallower or deeper energy minima, respectively. Here, we examine the structural basis of this phenomenon by directly measuring the effect of shear on the glass microstructure via time-resolved SANS techniques [78]. Moreover, by using a system that is fully rejuvenated by thermal cycling, we thoroughly investigate the use of shear as a rejuvenation method, which may fully regenerate the original mechanical properties, but incompletely rejuvenate the microstructure [127].

In the work presented here, we investigate colloidal glass aging by relating the bulk macroscopic properties to the underlying microstructure through concurrent rheological and small angle neutron scattering (Rheo-SANS) measurements, respectively. We employ a model thermoreversible adhesive hard sphere (AHS) system composed of octadecyl-functionalized nanoparticles dispersed in tetradecane [27, 35, 36, 88]. At the volume fraction selected for this study (ϕ=0.46), the system forms an attractive driven glass (ADG). In this model system, the attractions are controlled by temperature, which induces a phase transition of the brush [39]. At 40°C, the sample melts and is subsequently subjected to a pre-shear protocol that fully erases the structural history. Rheological aging in the gel state was first observed in this system by Eberle et al. who proposed aging occurred via the interdigitation of the brush [27]. In the same colloidal gel system, our most recent work develops a quantitative and predictive relationship between the macroscopic properties and the underlying microstructure during gel aging, which is independent of the thermal and shear history of the gel [75]. Here, we extend this work by connecting rheological and structural aging in a colloidal glass through simultaneous bulk property and microstructural

measurements. Moreover, we examine the effects of thermal and shear history on the glass structure and properties. Under these experimental conditions, this thermoreversible system forms a homogeneous glass and thus exhibits a fundamentally distinct and previously unexplored aging mechanism compared to the model systems described above.

5.2 Experimental Methods

5.2.1 Preparation of the Thermoreversible AHS System

The octadecyl-coated silica nanoparticles were functionalized using an established protocol [28, 39]. Briefly, Ludox TM-50 silica nanoparticles (30 nm in diameter) were purchased from Sigma Aldrich and reacted with 1-octadecanol (Alfa Aesar). The particles were purified by centrifugation in a Sorvall RC 6 Plus centrifuge and dried under a nitrogen stream and then in a vacuum oven for at least 24 hours. Full characterization of the functionalized nanoparticles was reported elsewhere [27, 39]. The dried particles were dispersed in tetradecane at a volume fraction of 0.46 which forms a glassy, thermoreversible adhesive hard sphere (AHS) system.

5.2.2 Concurrent Rheological and Structural Measurements (Rheo-SANS)

Simultaneous rheological and small angle neutron scattering (Rheo-SANS) were conducted at the National Institute of Standards and Technology (NIST) Center for Neutron Research (NCNR) in Gaithersburg, MD. Time-resolved SANS experiments were performed on the NGB 30m beamline in the 1,3 plane at a detector distance of 13 m with a focusing lens. An Anton Paar MCR-501 stress-controlled rheometer was placed into the beamline and the AHS sample was contained within titanium concentric cylinder geometry with an inner bob diameter of 28 mm and a 0.5 mm gap. The total

sample path-length was 1 mm and sample transmissions ranged from 0.301 to 0.304. Between experiments, the sample was rejuvenated using a two-step pre-shear protocol in which the sample was (1) sheared in its liquid state at 10 s^{-1} for 10 minutes at 40°C and (2) held quiescently at 40°C for 2 minutes. Aging experiments were conducted at 29.4°C at 0.1% strain and a frequency of 1 rad/s. Two thermal histories were investigated: (1) the cooling direction in which the sample was quenched from its liquid state at 40°C to 29.4°C and (2) the heating direction in which the sample was quenched from 40°C to 25°C and then to 29.4°C. The gas-cooled Rheo-SANS Couette sample environment exhibited imperfect temperature control, which resulted in overshoots from the set point temperature during the quench. The shear history dependence was evaluated by shearing the aged sample at rates of 5 s^{-1}, 100 s^{-1}, 500 s^{-1} and 1000 s^{-1}. A reference time of 4250 seconds was selected for consistency with results acquired for our earlier study investigating aging in the gel state (ϕ=0.28) [75].

5.2.3 Small-Angle Neutron Scattering (SANS)

Static SANS measurements were also conducted at the NIST NCNR on the NCB 30 m beamline. Detector distances of 1 m, 4 m, 13 m (with and without a focusing lens) were used. Samples were carefully loaded into cells containing a 0.01 inch aluminum spacers such that sample transmissions were approximately 0.80. The cells were loaded into a 10 position sample holder (10CB) equipped with a fluid bath to maintain the set temperature throughout the experiment. Samples were equilibrated at the desired temperature for at least 20 minutes prior to measurement.

5.2.4 Rheo-SANS Data Analysis

The SANS scattering data was analyzed using the SANS Data Reduction Macros in Igor Pro available from NIST [92]. Time-resolved scattering results were binned using event mode processing in Igor Pro. 1-D scattering patterns were fit to the sticky hard sphere (SHS) model (or Baxter model) to extract the Baxter parameter (τ) in SAS View. Fitting parameters are described elsewhere [39, 75]. We note that because the hard sphere structure factor calculated using the Percus-Yevick closure approximation deviates from experimental and computational results at high volume fraction, we fit the scattering length density (SLD) of the shell (SLD shell = -1.989e-06 $Å^{-2}$) to data. The perturbation parameter was fixed as $\varepsilon = 0.01$ for all cases.

5.3 Results and Discussion

This work quantitatively connects rheological aging to structural aging in a colloidal glass using rheometry and time-resolved small angle neutron scattering. First, in section 5.3.1, the microstructure of the thermoreversible colloidal system in the liquid state at 40°C and the glass state at 25°C are measured, which are plotted on the AHS phase diagram developed for this system. Then, in section 5.3.2, small amplitude frequency sweeps are conducted to find an appropriate temperature to perform subsequent aging experiments. In section 5.3.3, concurrent rheometry and SANS experiments are performed to connect the macroscopic bulk property changes to the evolution in the underlying microstructure during glass aging. Moreover, to evaluate the influence of thermal and shear history on the aging process, samples are formed using two different thermal profiles and varied rates of shear are applied to the aged sample.

5.3.1 Static Microstructural Measurements

Figure 5.1 shows SANS data for the AHS system at 40°C and 25°C. The length scales probed by these measurements (i.e., $2\pi/q \sim L$) range from the nanometer to ~0.5 microns. The lines show fitted SHS model predictions with the parameters indicated, showing that high temperature state is a liquid while the quenched sample is an AHS glass, as shown on the phase diagram (Figure 5.2). At the scattering vector (q) ranges investigated in subsequent Rheo-SANS ($0.008\ Å^{-1}<q<0.5\ Å^{-1}$), we do not observe steep power law behavior, indicating that the material is homogenous on the length scales investigated in this study. At largest length scales probed, the data deviates from model predictions. At present, these deviations are under investigation as artifacts due to the specifics of the neutron optics of the lens configuration coupled with some multiple scattering, as these samples have relatively low transmissions. Further, these deviations are independent of thermal history and shear rate, unlike the rest of the patterns. From here forward, the low-q data is removed. However, in contrast to the above results, other glassy systems exhibit strong upturns in scattering intensity that indicate large voids characterized by colloid-poor regions in the material, which was not observed for this system.

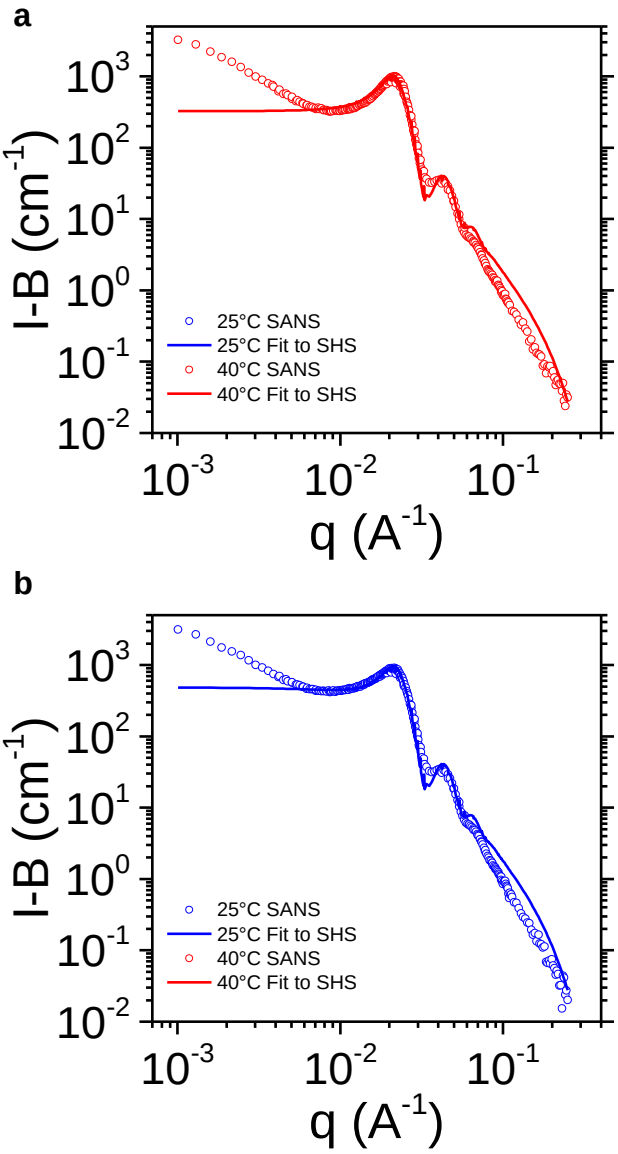

Figure 5.1: Small angle neutron scattering (SANS) data at 40°C (**A**) and 25°C (**B**). Note that the high temperature state is a liquid while the quenched sample shows much stronger scattering characteristic of an AHS glass. Fitted Baxter parameters shown on the plot are 0.367 and 0.234 at 40°C and 25°C, respectively. (Note "B" is the background, which was subtracted from the overall intensity.)

For reference, the phase diagram for the AHS system is presented in Figure 5.2. The phase diagram plots the Baxter parameter (τ_β) as a function of volume fraction (ϕ). The Baxter parameter was obtained from fitting liquid state theory to scattering data, as discussed below. A lower Baxter parameter corresponds to increased interaction strength and can be thought of as an effective temperature. The purple arrow on the diagram points to the location of two points of interest at working volume fraction for this study (ϕ=0.46). As described explicitly later, to examine the aging process, the sample was pre-sheared in its liquid state at 40°C and quenched to its glass state at 29.4°C where rheological and structural aging was monitored. On the phase diagram in Figure 5.2, the green triangles represent the experimentally determined dynamic arrest transition for this system [35]. The open red circular marker designates the liquid state at 40°C and the blue square marker labels the state of the soft glass for this work. To analyze our data, as discussed in the methods section, we fitted a single parameter (SLD of the shell) to the reference state data to more carefully capture the structural changes associated with aging in the glass state. As a result, the fitted Baxter parameter corresponding to the liquid state data obtained from the analysis conducted here appears to fall below the percolation line determined by Eberle and co-workers. However, the two results are consistent; when the SLD of the shell reported by Eberle and coworkers is used to fit the data in the above figure, we obtain a Baxter parameter of 1.25 (filled red circle on the phase diagram), which is above the experimentally determined dynamic arrest transition. Moreover, as the results presented here on glass aging are compared to our previous work on gel aging, two additional points corresponding to a gel sample (ϕ=0.28) are also plotted on the phase diagram. Similarly, the red circular marker

indicates the liquid state at 40°C and blue square marker corresponds to the gel state at 28.6°C, which was studied in Chapter 4.

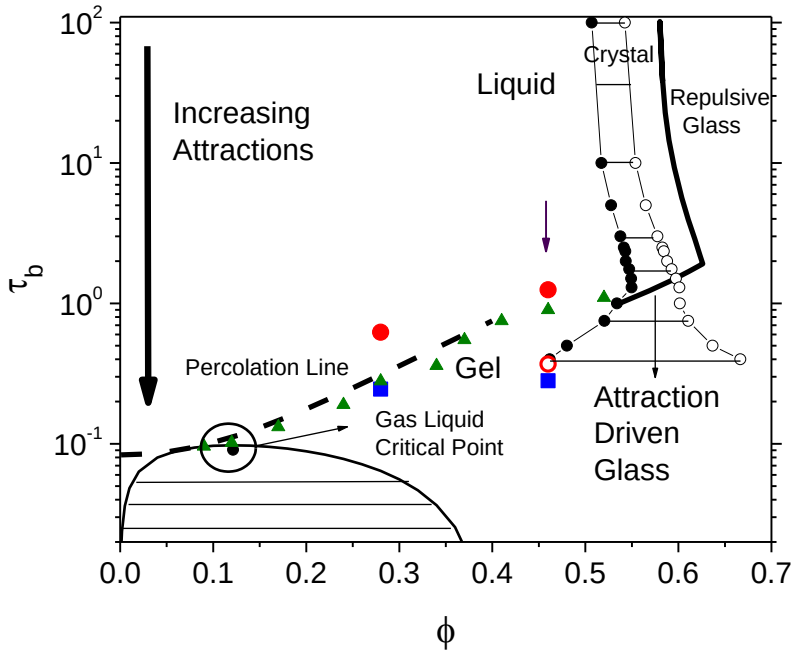

Figure 5.2: The phase diagram for the AHS system is presented. Relevant locations are clearly marked. The red circular marker designates the liquid state at 40°C and the blue square marker labels the equilibrium state of the soft glass at the working volume fraction (ϕ=0.46). In this work, a single fitting parameter was adjusted to more carefully capture the structural changes associated with aging, which led to a lower Baxter parameter (red, open circle) that fell below the percolation line determined by Eberle and co-workers (experimental data shown by green triangles). The results are consistent; applying the same fitting parameters as Eberle and co-workers, a Baxter parameter, which is above the dynamic arrest line, was obtained (filled, red circle) for the structural data reported here. As we interpret the results presented here in terms of previous work on gel aging, the red circular marker indicates the liquid state at 40°C and blue square marker corresponds to the equilibrium state of the aged gel (ϕ=0.28). Figure is produced from data in reference [35].

5.3.2 Rheological Measurements

Small amplitude frequency sweeps were conducted to determine the glass transition temperature and select an appropriate temperature to conduct aging experiments (Figure 5.3). The sample (ϕ=0.46) was quenched from its liquid state at 40°C to the temperature indicated in Figure 5.3. Rheological measurements began 45 minutes after setting the rheometer to the desired temperature to allow the sample to cool and equilibrate at the set temperature. All tests were conducted at 0.1% strain. The sweeps in Figure 5.3 indicate that the sample is highly sensitive to temperature changes as small as 0.1°C over the temperatures ranging from 29.4°C to 29.7°C. Based on this data, we observe that the transition temperature occurs between 29.5°C and 29.6°C. Eberle et al. previously reported a transition temperature for the same sample (ϕ=0.46) at 30.0°C [27], and we attribute this temperature discrepancy to a slight temperature difference between the TA Instruments AR-G2 with a Peltier plate and the gas-cooled Rheo-SANS environment used in this measurement. From the frequency sweeps displayed in Figure 3, we elected to conduct all subsequent aging experiments at 29.4°C, where a soft attraction-driven glass is observed.

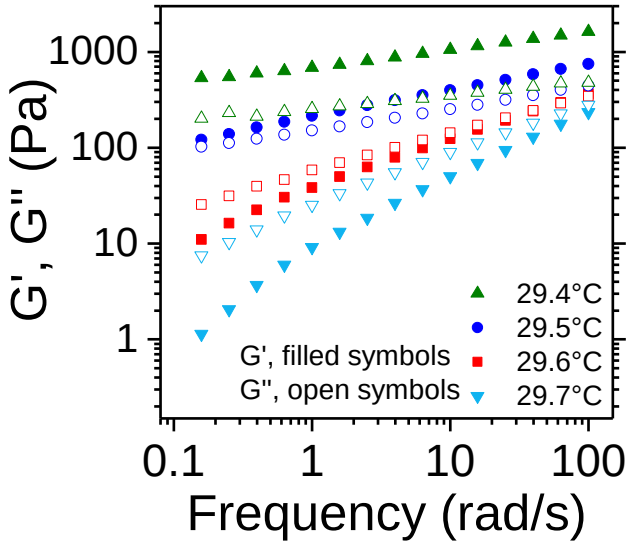

Figure 5.3: Small angle frequency sweeps for temperatures ranging from 29.4°C to 29.7°C. All tests were conducted at 0.1% strain. The critical temperature occurs between 29.5°C and 29.6°C. All subsequent aging experiments were conducted at 29.4°C; at this temperature, a soft attractive-driven glass formed.

Aging phenomena was observed in the attraction-driven glass. In the model system selected for this study, short-range attractions are controlled by temperature via a liquid-to-solid transition of the octadecyl brush grafted to the surface of the silica nanoparticle. Specifically, the sample was immediately quenched from the liquid state at 40°C to a soft attraction-driven glass at 29.4°C and small amplitude oscillatory shear experiments revealed that the storage modulus (G′) evolved in time after the temperature equilibrated, as shown in Figure 5.4. There was a temperature overshoot due to imperfect temperature control on the Rheo-SANS equipment, which paired with the high sensitivity of sample to 0.1°C temperature changes (Figure 5.3), resulted in the non-monotonic changes in storage modulus early in the experiment. The overshoots in

storage modulus directly correspond with the fluctuations in temperature; as expected, peaks and troughs in temperature correspond to troughs and peaks in storage modulus, respectively. However, after the temperature equilibrated, the specimen continued to stiffen throughout the two hour aging experiment. This continual increase in storage modulus in time is characteristic of rheological aging, which we further investigated via structural measurements in the following section.

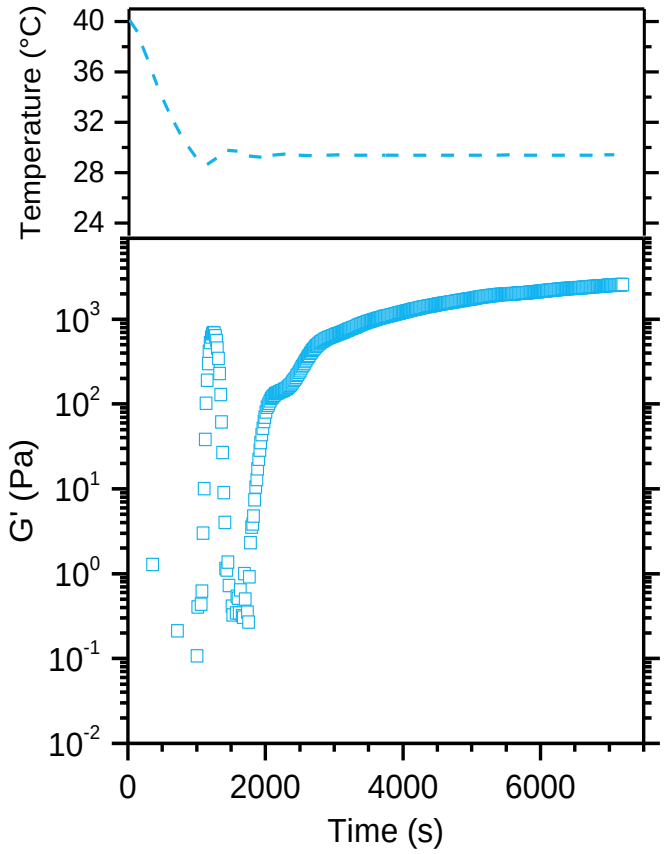

Figure 5.4: The attractive-driven glasses ages. The sample was immediately quenched from its liquid state at 40°C to a soft attractive-driven glass at 29.4°C. The temperature overshoots from the imperfect temperature control on the Rheo-SANS equipment, paired with the high sensitivity of sample to small temperature changes, resulted in the non-monotonic changes in storage modulus early in the experiment. However, after the temperature equilibrated, the specimen continued to stiffen throughout the two hour aging experiment.

5.3.3 Concurrent Rheological and Structural Measurements

Time-resolved SANS data were collected to monitor the structural evolution of the glass during aging. Samples were immediately quenched from 40°C to the glass state at 29.4°C. Using event mode processing in Igor Pro, the scattering data were binned into 20 intervals, each 6 minutes in duration, and shown in Figure 5.5A. Small structural changes are observed in which the greatest changes occur at the longest length scales probed (i.e., lowest q). As shown in the figure, the microstructure evolves to a pattern that would be expected for a concentrated glass. As the sample forms and ages, the evolution in microstructure is consistent with particles sampling progressively lower energy states, in concurrence with the free energy viewpoint of aging. Moreover, as expected, the nearest neighbor peak at $q \approx 0.02$ $Å^{-1}$ corresponds to a length scale of approximately 30 nm, which is the diameter of the particles used in this study. These structural measurements correspond to the rheological experiment conducted above (Figure 5.4), and are analyzed jointly below.

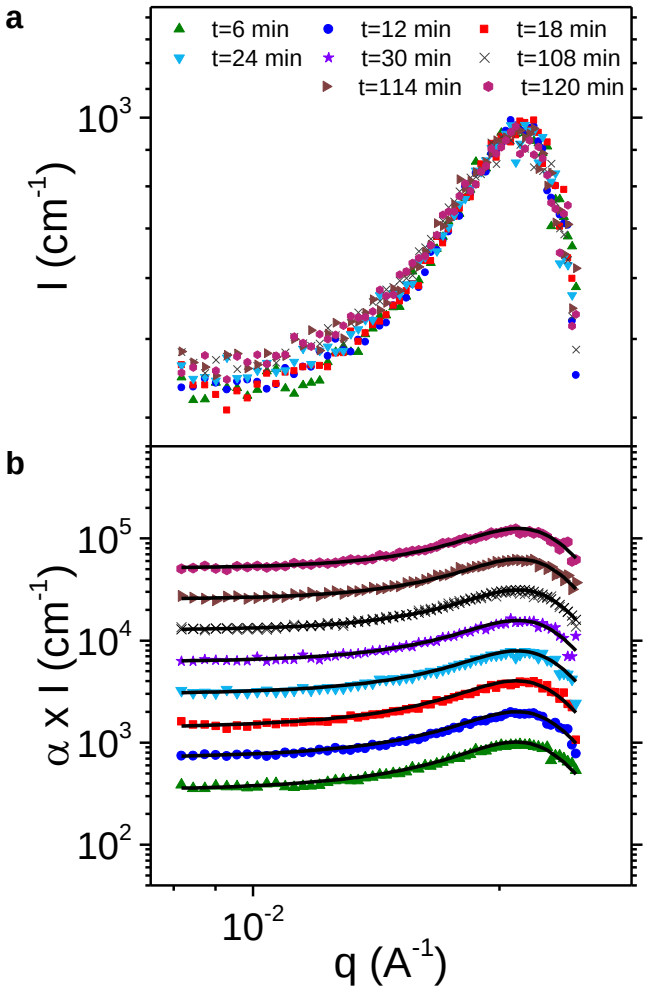

Figure 5.5: Time-resolved small angle neutron scattering (SANS) data during a two hour aging experiment are shown. Samples were quenched from the liquid state at 40°C to 29.4°C. **A.** Scattering data during the two hour aging experiment was binned into 20 intervals. **B.** The data was fitted to the sticky hard sphere model. The intensity was doubled from the previous data set to more clearly display the fits.

Using a structural parameter λ, we directly related rheological aging to structural aging in the thermoreversible model glass. First, to assess structural changes during aging, the scattering data was fit to the SHS model, which is commonly used to model attractive systems [27, 75]. In this work, only one parameter, the Baxter parameter (τ), was fit to data at each time point. This effective τ, or τ_{eff}, was used to track the evolution of the microstructure. All other fitting parameters were described in the methods section. The data and the fitted models are displayed in Figure 5.5B. Note that the intensities at each time point are offset by a factor of two from the previous data set for clarity. For each bin of data, a fitted parameter τ was obtained, and the evolution of this parameter in time tracks the effective strength of attraction between the particles in the glass as it ages. As explained in Chapter 4, the Baxter parameters obtained from this analysis represent points along an aging trajectory and are not equilibrium states. To quantify structural changes toward equilibrium, we calculated a structural parameter λ as follows:

$$\lambda = \frac{\tau_{40}^{eq} - \tau^{eff}}{\tau_{40}^{eq} - \tau_{\infty}} \tag{5.1}$$

where τ_{40}^{eq} is the value of the Baxter parameter in the liquid state at 40°C, τ^{eff} is the value of Baxter fit parameter during each time interval and τ_{∞} is the equilibrium Baxter parameter for this temperature. By fitting the SHS model to time-resolved SANS data, τ_{40}^{eq} = 0.367 and $\tau_{\infty} \approx 0.281$. (Baxter parameters at temperatures of interest are shown in Table 5.1.)

The evolutions in microstructure and bulk properties are shown in Figure 5.6A. The reported G′ values correspond to averaged values of the storage modulus during each 6-minute interval. To relate particle interactions to resultant mechanical properties, we first reduce noise from SANS measurements and/or nonlinear model

fitting by using linear regression to obtain an empirical expression for the Baxter parameter as a function of the aging time:

$$\lambda = 0.119 \ln t + 0.393 \quad (5.2)$$

where the units of t are minutes. As the glass ages ($t \geq 30$ minutes), there is a monotonic increase in both G′ and λ as the sample evolves towards its equilibrium state. Moreover, Figure 5.6B, which displays G′ as a function of λ, indicates that there is a one-to-one relationship between storage modulus and microstructure that evolves in time as the sample ages, similar to the colloidal gels [75].

We analyze our results within an Avrami framework to develop an empirical equation that quantitatively captures the relationship between log G′ and λ as the glass ages. The Avrami equation, which is a kinetic model that describes the process of crystallization by nucleation and growth, was previously used to relate the mechanical properties to a space filling parameter, ζ, during crystallization of a fatty acid model system [128]. In this spirit, we adapt the Avrami analysis to relate the mechanical properties (G′) to the underlying microstructure (λ) as the glass ages:

$$\log G' = 3.40\ (1 - \exp(-7.64\ \lambda^{10.92}) \quad (5.3)$$

where $0.80<\lambda<0.96$. Figure 5.6B shows this empirical equation represents the data well. However, based on this analysis, there is no clear interpretation for the Avrami parameters in the above equation. Further work is required to interpret the results within the Avrami framework and extract a physical meaning. Importantly, however, this is the first approach toward developing a phenomenological relationship between colloidal glass microstructure and rheological properties during glass aging. Moreover, the monotonic increase in both the bulk properties and structural parameter is consistent

with the free energy landscape viewpoint of aging, in which a sample evolves toward equilibrium by sampling progressively lower energy states.

Table 5.1: Table of Baxter parameters used in this work.

Temperature (°C)	**τ value**
40°C	$\tau_{40} = 0.367$
25°C	$\tau_{25} = 0.234$
29.4°C	$\tau_{\infty} \approx 0.281$

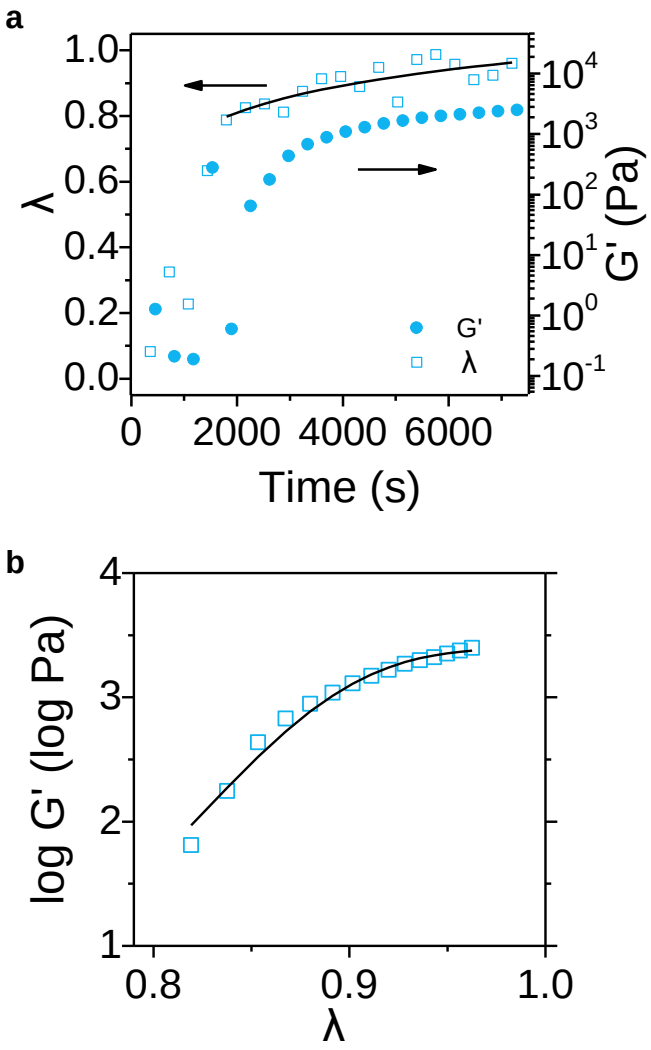

Figure 5.6: A quantitative relationship between the bulk property changes (G′) and the underlying microstructure (λ) during colloidal glass aging is developed. **A.** The evolution in G′ and λ is shown. Noise from SANS measurements and/or nonlinear model fitting was reduced by using linear regression to obtain expressions for the effective τ as a function of the aging time: $\lambda = 0.119 \ln t + 0.393$ where t is given in minutes. As the glass ages ($t \geq 30$ minutes), there is a monotonic increase in both G′ and λ as the sample evolves towards its equilibrium state. **B.** G′ is plotted as a function of λ. A specific storage modulus corresponds to a specific microstructure, which evolve in time as the sample ages. The Avrami equation (solid line, eqn 5.3) captures the relationship between log G′ and λ as the glass ages.

While the above analysis enabled the development of an empirical, but quantitative relationship between structural and rheological aging in colloidal glasses, the mechanistic origin of the aging process remains unclear. To understand this process, we calculated a localization length based on predictions from mode coupling theory (MCT). As discussed in the previous chapter, the localization length is the mean squared displacement of particle motion when trapped within a cage of nearest neighbors. The prediction from MCT is shown below:

$$\frac{G'a^3}{k_BT} = 0.29\frac{\phi a^2}{r_{loc}^2} \tag{5.4}$$

where a is the particle radius and r_{loc} is the localization length [102]. Using the final G′ value measured after two hours of aging during the small amplitude oscillatory shear measurement shown in Figure 5.4, a localization length of 3.8 nm was calculated. This localization length is very close to the localization length of 3.3 nm calculated for the AHS gel [75]. Moreover, the calculated localization length is on the order of the brush size, which was reported as 2.76 nm by Eberle and coworkers [39], who proposed interdigitation of the brush layer as the aging mechanism in the system [27]. This result suggests local particle motion as the mechanism of aging in this system, which is similar to the results observed in colloidal gels. Overall, the localization length calculated from MCT suggests that local particle rearrangements persistently occurring within the glass are responsible for the observed structural and rheological aging.

5.3.3.1 Effect of Thermal History

To evaluate the effect of thermal history on the evolution of bulk properties and microstructure, the glass was formed using two distinct thermal profiles. As described in the methods section, samples were formed by: (1) quenching from 40°C to 29.4°C (the cooling direction) or (2) quenching from 40°C to 25°C to 29.4°C (the heating

direction). Thus far, all samples were formed following application of the cooling profile. Here, we evaluate the microstructure and bulk properties from an alternative thermal path, designated here as the heating direction, and compare them to the results presented earlier for samples quenched from the cooling profile. To track the structural evolution of the glass, time-resolved SANS data were collected. Specifically, samples were rejuvenated by following the pre-shear protocol at 40°C and quenched to 25°C for 45 minutes. The temperature was raised from 25°C to 29.4°C and Figure 5.7 displays the corresponding evolution in microstructure as the AHS colloidal glass forms and ages from the heating direction. Similar to the earlier experiment for samples quenched from the cooling profile, the data was analyzed using event mode processing in Igor Pro, in which the scattering data was binned into 20 intervals, each 6 minutes in duration. The scattering data corresponding to samples formed and aged from the heating profile are consistent with a more deeply quenched glass that transitions to a less attractive glass and evolves towards an equilibrium state. In contrast to the cooling data, the glasses formed and aged from the heating direction appear to sample fewer energy states, which is consistent with particles attempting to escape from deep energy wells in favor of lower free energy states via thermal motion. These results qualitatively mirror the behavior observed for AHS colloidal gels [75] and support aging as a trajectory in the free energy landscape where the microstructure evolves towards an equilibrium state characterized by increasing particle attractions.

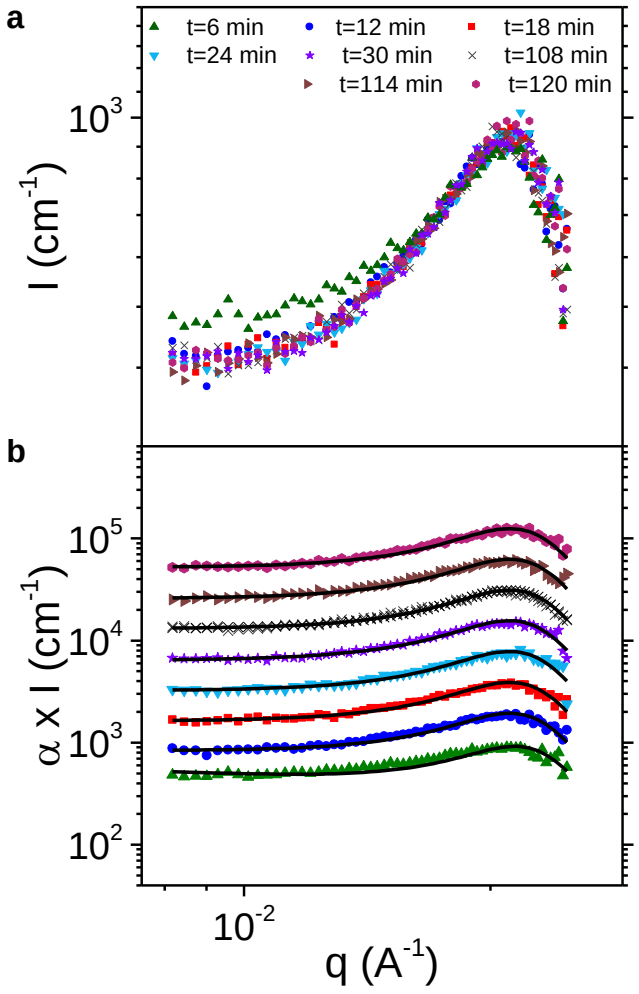

Figure 5.7: Time-resolved small angle neutron scattering (SANS) data during a two hour aging experiment are shown. Aging was examined from the "heating direction"; the temperature was reduced from 40°C to 25°C prior to aging at 29.4°C. **A.** Scattering data during the two hour aging experiment was binned into 20 intervals. **B.** The data was fit to the sticky hard sphere (SHS) model to obtain a single structural parameter, λ, to quantify the structural aging in the glass. The intensity was doubled from the previous data set to more clearly display the fits.

The influence of the thermal history on the mechanical properties and microstructure is shown in Figure 5.8A. While the path towards the equilibrium state of the glass is highly dependent on the quenching profile, samples formed and aged from both quenched profiles appear to approach the same equilibrium state. For this analysis, once again, we reduce noise from SANS measurements and/or nonlinear model fitting via linear regression as shown by the solid lines on the plot. Importantly, for both thermal histories, a monotonic increase in bulk properties, which correspond to a monotonic evolution in microstructure, was observed during aging. In samples formed from both thermal profiles, the data suggests a one-to-one correspondence between rheological aging and structural aging, which is consistent with aging as a trajectory in the free energy landscape, in which the glass evolves towards lower energy states as it approaches its equilibrium state. To evaluate how thermal history impacts the aging trajectory, the mechanical properties are shown as function of the structural parameter in Figure 5.8B. The error bars represent the 95% confidence interval on the regressed structural parameter. Using this analysis for an aging AHS gel (Chapter 4), we observed a one-to-one correspondence between mechanical properties (G′) and gel microstructure (λ) during aging, which was independent of the thermal pathway [75]. Interestingly, for AHS colloidal glasses, it appears that the relationship between G′ and λ during aging may be influenced by the thermal profile. It is important to note that both gel and glass aging were monitored over a two hour period, yet particle rearrangements were likely slower in the concentrated sample due to the reduced mobility. In the aging gel sample, the convergence of G′ from the heating and cooling direction occurred after approximately an hour, after which the thermal history did not affect the relationship between G′ and λ; meanwhile, the convergence of the storage moduli in the glass sample

occurred near the very end of the two hour experiment as displayed in Figure 5.8A. It is at these later time points that values begin to converge as shown in Figure 5.8B. Based on these results, we hypothesize that the influence of the thermal profile during formation may weaken as the sample ages, and a longer aging experiment may reveal a convergence of two thermal profiles shown in Figure 5.8B.

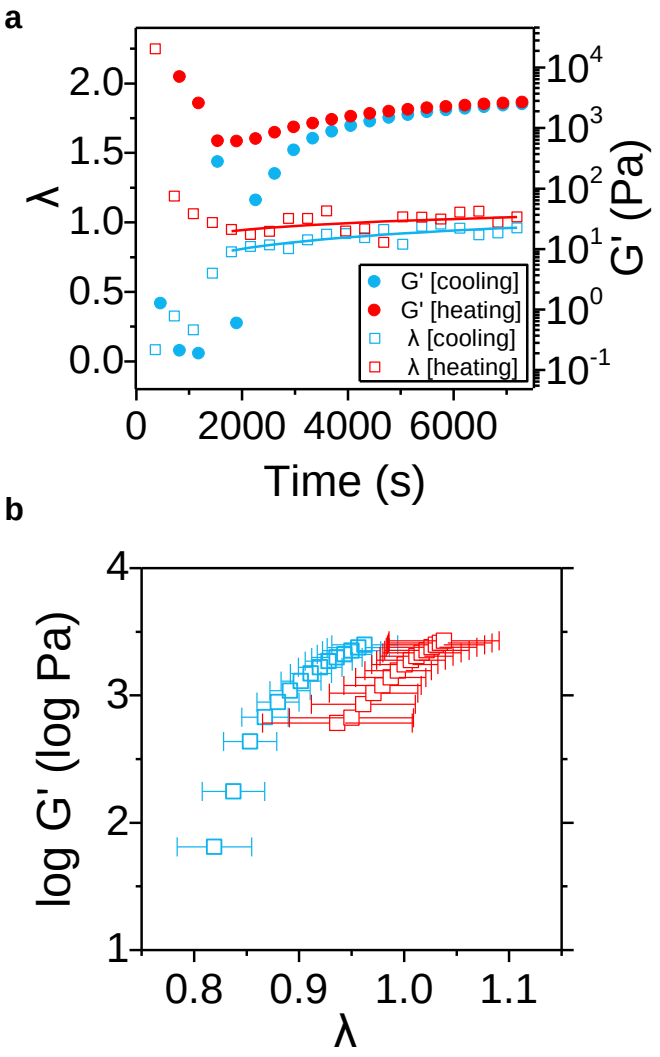

Figure 5.8: The influence of thermal history on the microstructure and bulk properties during aging is displayed. **A.** The evolution of the structural parameter λ and storage modulus, reported every six minutes, over a two hour aging experiment is shown for a ϕ=0.46 colloidal glass. Glasses were formed and aged from two distinct thermal profiles: (1) the cooling profile in which the temperature was dropped from 40°C to 29.4°C and (2) the heating profile where the temperature was increased from 25°C to 29.4°C following a pre-shear protocol at 40°C. **B.** The storage modulus is plotted as a function of its microstructure, captured by the structural parameter λ, which indicates that the relationship between G′ and λ during aging may be influenced by the thermal profile.

5.3.3.2 Effect of Shear History

To assess how processing conditions influence the aging process, we probe the aged glass by applying shear. In these experiments, glasses were formed from the cooling profile and aged to a reference state of 4250 s, which was selected for consistency to prior work [75]. The aged sample was then immediately sheared at rates of 5 s^{-1}, 100 s^{-1}, 500 s^{-1} or 1000 s^{-1} for 20 minutes. The same sample was used for this set of experiments, and was fully rejuvenated via thermal cycling between tests, as described in the methods section. The microstructure and corresponding viscosity during shear are displayed in Figure 5.9A and Figure 5.9B, respectively. Similar to the previous analysis described above, the microstructural measurements were fit to the SHS model, from which λ values were calculated. For shear rates of 5 s^{-1}, 100 s^{-1}, 500 s^{-1} and 1000 s^{-1}, structural parameters of 1.03, 1.27, 1.08 and 0.94 were calculated, respectively. The increase and subsequent decrease in λ is consistent with the shear-induced building and destruction of the sample microstructure, respectively. These results are similar to the experimental results of Eberle and co-workers, which showed that large strains (comparable to or exceeding the interparticle force) destroyed the sample microstructure while weak flow led to additional structuring of the sample [104]. Under the conditions studied in this work, the pronounced shear-induced anisotropy measured by Eberle et al. was not observed. Thus, the changes in λ observed here are due to shear-induced structure, which do not persist following the cessation of shear, as discussed below.

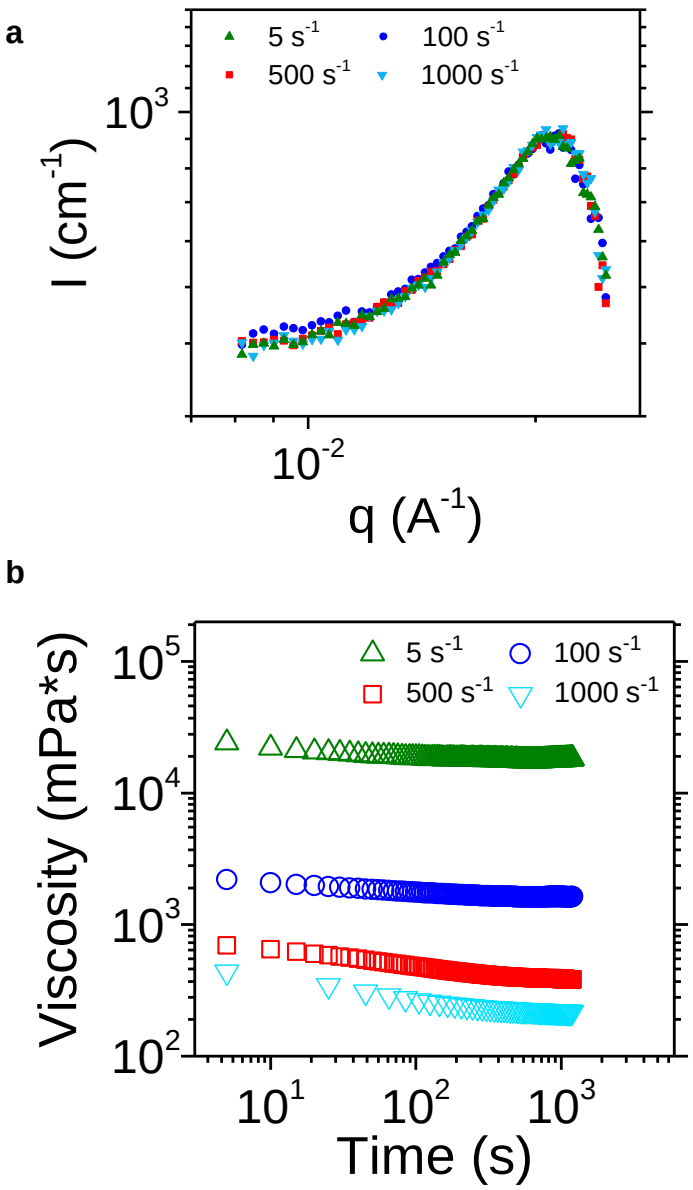

Figure 5.9: **A.** Microstructural measurements of 0.46 volume fraction colloidal glass under shear rates of 5 s^{-1}, 100 s^{-1}, 500 s^{-1} and 1000 s^{-1} for 20 minutes are shown. The corresponding λ values are: λ_{5s}^{-1}=1.03, λ_{100s}^{-1}=1.27, λ_{500s}^{-1}=1.08 and λ_{1000s}^{-1}=0.94. **B.** The corresponding viscosity measurements during shear are also displayed.

Following the application of shear, the aging process was tracked for an additional 4250 s to further assess the influence of shear on the aging trajectory. Specifically, the continued aging of the specimen was monitored using small amplitude oscillatory shear measurements. The evolution of the microstructure is displayed in Figure 5.10A after shearing at 1000 s^{-1}. An initial, intermediate and final structure is shown and the corresponding λ values increase from 0.64 to 0.96 by the conclusion of the 4250 s aging experiment. The increasing λ values signify the rebuilding of structure as the sample ages. Figure 5.10B displays the corresponding mechanical property changes following shearing at the specified rate. Immediately following shear, G′ values decrease to below the detection limit on the rheometer following shearing at 500 s^{-1} and 1000 s^{-1}, indicating the higher shear rates rejuvenated the sample's mechanical properties. The mechanical properties following shearing at 100 s^{-1} show an order of magnitude decrease of G′, yet does not appear to fully restore the mechanical properties, while the bulk properties following shearing at 5 s^{-1} show only a slight decrease in mechanical properties immediately following shear compared to the samples sheared at higher rates. At the lowest shear rate tested (5 s^{-1}), we do not observe clear evidence of overaging. We note that the sample sheared at 5 s^{-1} evolved to a slightly higher storage modulus at the conclusion of the experiment when compared to samples that were sheared at higher rates. However, this difference may also be due to slight variability in aging (inset in Figure 5.10B). Future work testing the sample's mechanical properties and microstructure following the application of oscillatory strains (1 s^{-1}) are proposed in Chapter 6 to investigate this phenomenon further. At the higher shear rates tested, the rejuvenation of mechanical properties indicates that shear destroys the microstructure, decreasing the glass "age". However, despite rejuvenation of bulk

properties following shear, the underlying microstructure may only partially rejuvenate, as discussed further below. Regardless of shear history, however, the samples eventually evolve along a similar trajectory as the sample ages (Figure 5.10B).

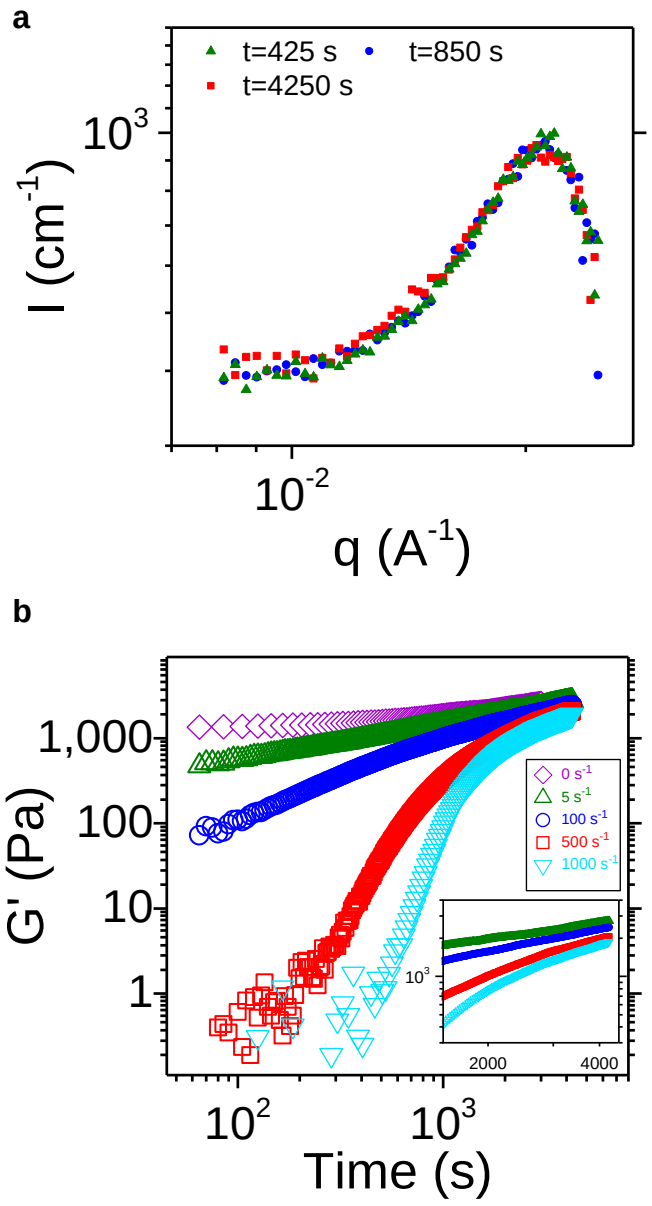

Figure 5.10: **A.** Time-resolved microstructural measurements following 20 minutes of shearing at a rate of 1000 s^{-1} (λ_{425s}=0.64, λ_{850s}=0.74, λ_{4250s}=0.96) are displayed. **B.** The evolution of mechanical properties under SAOS after shearing for 20 minutes at the specified shear rate is shown.

The effectiveness of mechanical rejuvenation to restore the original microstructure in colloidal glasses has not been extensively investigated. By using a system that is fully rejuvenated by thermal cycling, we investigate the use of shear as a rejuvenation method, which may restore the original mechanical properties, but incompletely rejuvenate the microstructure. Figures 5.11A and B compare the effects of thermal rejuvenation and mechanical rejuvenation on the evolution of mechanical properties and microstructure, respectively. Thermal rejuvenation consisted of shearing the sample at 10 s^{-1} in its liquid state at 40°C for 10 minutes followed by holding the sample quiescently at 40°C for 2 minutes. Mechanical rejuvenation consisted of shearing the sample at isothermally (at 29.4°C) at 1000 s^{-1} for 20 minutes. Following the cessation of shear, an immediate rise in the mechanical properties was observed, whereas the sample that was thermally rejuvenated evolved more slowly. This indicates that either the glass structure was not completely erased by shearing, or that the microstructure continued to evolve under shear. Figure 5.11B confirms the former perspective as the sheared sample starts with a much larger value of λ. However, despite differences in the trajectory during formation and early aging, the samples appear to tend toward a similar equilibrium state regardless of shear history. Figure 5.12 clearly shows similar aging trajectories; note that the cooling data was shifted in time only (by 24 minutes) to directly compare thermal rejuvenation to mechanical rejuvenation. This long-time behavior is qualitatively similar to the results obtained for colloidal gels [75]. Indeed, the same empirical relationship between G' and λ that was developed for glass aging following a thermal quench (equation 5.3) applies to glass aging following shear at the rates tested in this work (Figure 5.13). We note that at short times immediately following shear (corresponding to low λ values in the figure), the data deviates from the

relationship, which indicates that immediately following shear, λ may not fully characterize the microstructure. However, during long-time aging, this result indicates that there is a one-to-one correspondence between the mechanical properties and underlying microstructure under these experimental conditions.

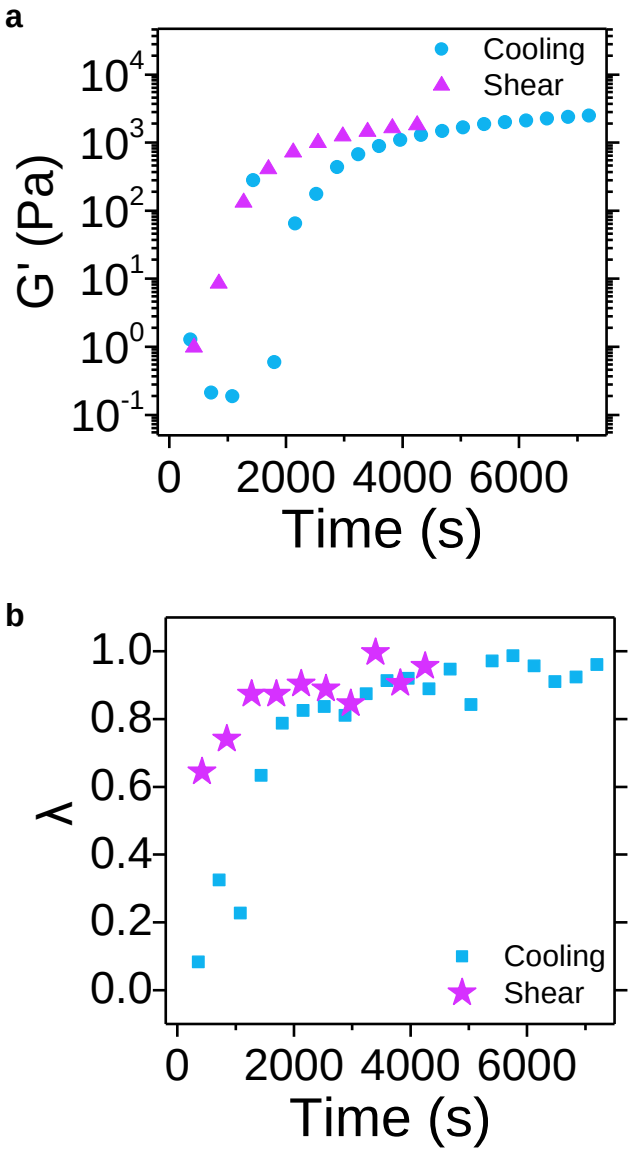

Figure 5.11: The effects of thermal and mechanical rejuvenation on gel mechanical properties (G′) and microstructure (λ) are shown. Thermal rejuvenation consisted of shearing the sample at 10 s^{-1} in its liquid state at 40°C for 10 minutes followed by holding the sample quiescently at 40°C for 2 minutes. Mechanical rejuvenation consisted of shearing the sample at isothermally (at 29.4°C) at 1000 s^{-1} for 20 minutes. **A.** Evolution of storage modulus following thermal cycling and shear. **B.** Evolution of microstructure following thermal cycling and shear.

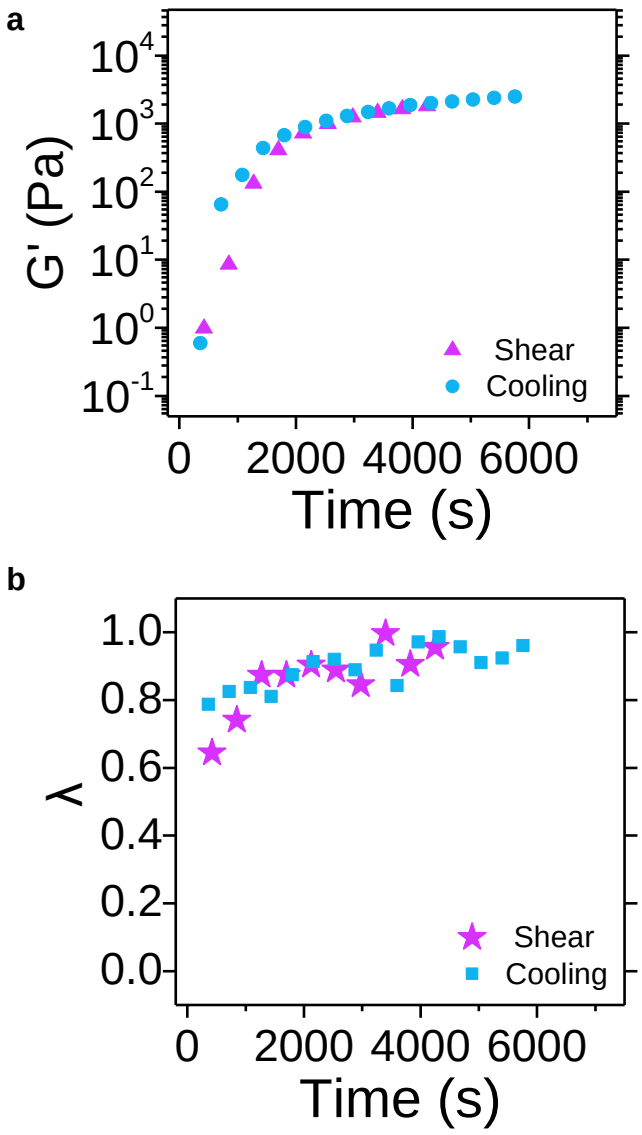

Figure 5.12: Data from Figure 5.11 replotted to directly compare thermal rejuvenation to shear rejuvenation. Cooling data was shifted in time only (by 24 minutes) to overlay the aging trajectory following shear rejuvenation.

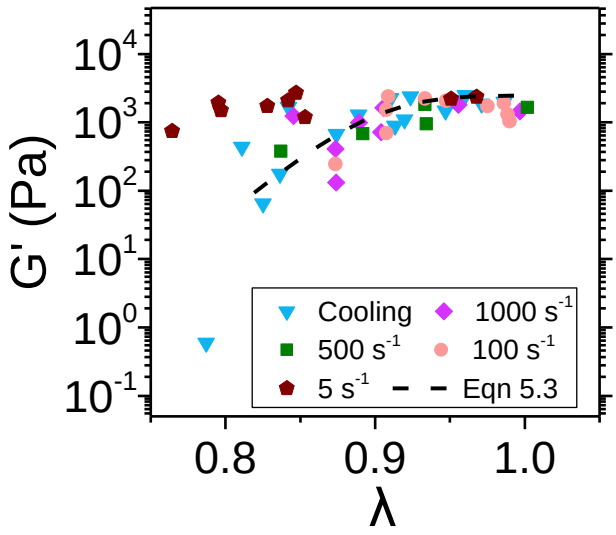

Figure 5.13: The storage modulus is plotted as a function of its microstructure, which is described by the structural parameter λ, to directly relate the bulk properties to the underlying microstructure following shear. The same relationship between G′ and λ that was developed for glass aging following a thermal quench (eqn 5.3, dashed black line) applies to glass aging following shearing the sample at 5 s^{-1}, 100 s^{-1}, 500 s^{-1} and 1000 s^{-1}, indicating that there is a one-to-one correspondence between the mechanical properties and underlying microstructure under these experimental conditions. We note that at short times immediately following shear (corresponding to low λ values in the figure), the data deviates from the relationship, which indicates that immediately following shear, λ may not fully characterize the microstructure.

5.4 Summary and Conclusions

In this work, we quantitatively relate rheological aging to structural aging in a thermoreversible colloidal glass (ϕ=0.46) using concurrent rheometry and time-resolved small angle neutron scattering (Rheo-SANS) measurements. Time-resolved SANS measurements were fit to the SHS model to obtain a Baxter parameter at each time-point, from which a structural parameter λ was calculated to quantify the evolution in microstructure as the system ages. A monotonic increase in both the bulk properties and structural parameter during aging was observed, from which an empirical relationship between G' and λ was established. To our knowledge, this is the first approach toward developing a phenomenological relationship between colloidal glass microstructure and rheological properties during aging. Mode coupling theory predicts a localization length of 3.8 nm for this AHS glass, which is on the order of the brush size, indicating that local particle rearrangements may be responsible for the observed rheological aging.

Moreover, by probing the system with different thermal profiles and shear rates, the effects of thermal and shear history on glass mechanical properties and microstructure during aging were investigated. At the shear rates tested, shear destroys the glass microstructure, decreasing the glass "age" and either incompletely or fully rejuvenating the mechanical properties at lower (5 s^{-1} and 100 s^{-1}) and higher (500 s^{-1} and 1000 s^{-1}) shear rates, respectively. However, despite rejuvenation of bulk properties following shear, the underlying microstructure may only partially rejuvenate. As the model system employed in this study is fully rejuvenated by thermal cycling, we directly compared thermal rejuvenation to mechanical rejuvenation. After mechanical rejuvenation, the evolution of the storage modulus and λ progressed more rapidly compared to the thermal rejuvenation, indicating that either the glass structure may not

be completely erased by shear or that the microstructure continues to evolve under shear. While the glass formation and aging trajectory is significantly affected immediately following a temperature quench or the application of stress, the samples appear to eventually evolve along a similar aging trajectory, independent of the thermal and shear history for long times. Thus, despite differences in processing conditions tested here, all samples eventually age similarly.

In conclusion, this work extends the understanding of aging behavior in colloidal glasses by quantitatively linking the macroscopic bulk property changes to the underlying microstructural rearrangements. The results and analysis contained herein may be applied to further understand the molecular mechanism underlying the aging process in other model colloidal systems or colloidal-based consumer products. Moreover, our measurements and approach may be employed to validate or improve simulations, and extended to examine and interpret non-equilibrium behavior in atomic or molecular systems.

Chapter 6

SUMMARY, CONCLUSIONS AND FUTURE WORK

In conclusion, significant progress has been made towards the development of an advanced, protective material that offers self-healing functionality, which allows for self-repair following material fatigue or failure, and increased strength in response to ballistic or puncture threats via the incorporation of colloidal particles. In particular, this thesis focused on the development and characterization of each component of the envisioned material through (1) the design and testing of light- and force-activated polymers for self-healing applications and (2) the characterization of the long-time behavior in a model colloidal gel and glass. In Chapter 2, a new class of photo-active materials was introduced that incorporated an iniferter group into the network architecture, which initiated a photo-triggered secondary polymerization, increasing the modulus by two orders of magnitude while strengthening the network by over 100%. The final modulus was tuned *a priori* by adjusting the concentration of the polymerizable group in the initial formulation. Moreover, the versatility of this new approach was demonstrated in three ways: (1) fully healing, reforming, and strengthening a sample after it had been severed, (2) photopatterning via spatial confinement of the light-induced property changes, and (3) cold-working a polymer film into a 3D configuration and then "locking-in" the film's shape using light. Previous radical-based methods that use a separate photoinitiator eventually terminate, eliminating the possibility of multiple healing events and making it challenging to tune bulk properties changes; however, the radicals produced in the system described here

are produced by a long-lived radical species that reversibly recombine, thereby allowing radical generation within the network to be continuously triggered using light. The utility of this dynamic bond is explored further in Chapter 3 by demonstrating that it is triggered by mechanical force in addition to light. While most synthetic polymers fail in response to sustained or increased levels of force, these force-responsive 'smart' polymers were designed to cleave selectively under stress, which triggers a crosslinking reaction and results in a significant macroscopic bulk property change (i.e., gelation) within minutes. These polymers are engineered to contain reversible addition-fragmentation chain-transfer (RAFT) units, or thiocarbonylthio functional groups, in the polymer backbone that function as mechanophores (i.e., mechanically-responsive chemical units). In contrast to other mechanophores, which require extensive synthetic procedures, these polymers were synthesized in a single step via a RAFT polymerization. These new, force-sensitive polymer systems that respond constructively to force are an important step towards developing responsive materials that heal without human intervention.

In Chapters 4 and 5, a temperature-responsive model colloidal system was examined to quantitatively relate rheological aging to structural aging by simultaneously measuring the bulk properties and gel microstructure using rheometry and small angle neutron scattering (Rheo-SANS), respectively. These studies enabled an empirical relationship to be established between the time-dependent storage modulus and the underlying microstructure as the sample aged. The effects of thermal and shear history on the aging behavior of this thermally-responsive model system were investigated in combination with the effectiveness of mechanical rejuvenation, which appears to rejuvenate mechanical properties but does not fully restore the gel structure.

Overall, the rheological and microstructural results for the colloidal gels and glasses examined in this work were consistent with local particle rearrangements as the mechanism of aging, which led to monotonically increasing interaction strengths in a continuously evolving system, and supported the hypothesis that aging is governed by the system's trajectory in the free energy landscape.

In the work shown here, a photo-active 'healing' network and a mechanically-active 'healing' polymer system were demonstrated; however, combining the two concepts into a mechanically-active 'healing' network, remains a challenge. The photo-active network developed in Chapter 2 could not withstand force-based testing as the material was highly solvated and weak prior to the secondary polymerization. By altering the network chemistry (incorporating rigid isocyanate groups), a stronger network was developed, but it did not allow for enough molecular mobility for the second-stage polymerization on an experimentally accessible timescale, even when tested under light. Towards the development of such a force-responsive crosslinked network, a double network strategy incorporating "sacrificial" bonds should be investigated [129]. The double network approach described by Durcot and co-workers in 2014 resulted in an elastomer with increased stiffness and toughness due to sacrificial bonds, which selectively broke before material failure occurred [129]. Here, such a double network strategy would incorporate a rigid network (network 1) that can withstand mechanical deformation while allowing the sacrificial bonds, such as the trithiocarbonyl groups used in this work, to be incorporated in the crosslinks of another network (network 2), that can cleave and initiate a healing polymerization. Preliminary data indicate that the double network approach appears to be a viable path towards the development of a mechanically-active polymer network.

Additionally, further studies focusing on the aging behavior of the colloidal gels and glasses are recommended. In particular, future work may further investigate "overaging" behavior in the thermoreversible colloidal systems studied here. As described in Chapter 5, experimental and computational studies have shown that application of low to moderate strain to colloidal systems led to overaging, or accelerated aging. It is hypothesized that low or moderate shear enables the systems to explore lower free energy states, thus promoting aging. Under the conditions studied in this dissertation (i.e., steady shear), overaging behavior was not observed. However, application of oscillatory shear at low shear rates may lead to overaging behavior and future studies may investigate the structural and rheological response of the system under these conditions using Rheo-SANS. Moreover, continued study of a weak (ϕ=0.12) gel are envisioned. (Preliminary data for this sample are shown in Appendix D.) In particular, it is hypothesized that a deeper (and more controlled) temperature quench of the weak gel may lead to phase separation. By monitoring the rheological changes and underlying microstructure during gel formation and aging following a deep quench, a distinct mechanism of aging that was not observed for the gel and glass samples studied in the dissertation may be revealed.

The results from this dissertation lay the foundation for the development of the protective material described in the introduction. Such a material will offer self-healing functionality, which will initiate self-repair in response to material fatigue or failure, while simultaneously providing increased strength in response to ballistic or puncture threats through the incorporation of colloidal particles. As future work, a self-healing composite material composed of colloidal particles is proposed. In particular, colloidal particles may be added as filler material to polymer networks containing a photo- or

mechanically-responsive crosslinker, resulting in composite materials with enhanced strength and reduced cost. To accomplish this, a solution-based model system consisting of the mechanically-active polymer in solution with diacrylate monomer and colloidal particles can be tested to evaluate the response of the system to applied force. As described in in Chapter 4, the mechanically-active polymer initiated a radical polymerization during sonication. In the work proposed here, the polymer system will be tested using stress-controlled rheometry, which will provide a more precise measure of the shear force required to cleave the polymer to aid in the formulation of the composite material. Moreover, silica nanoparticles could be added to the formulation to enhance the stress response. Future Rheo-SANS experiments could focus on studying the microstructure during a force-induced crosslinking polymerization. An alternative approach is to functionalize the silica nanoparticles with the labile bond crosslinker described in Chapter 2. The particles can be formulated using a similar synthetic strategy as the octadecyl coated-nanoparticles studied here. These functionalized particles may be used in formulations, such as those for shear thickening fluids, which have been shown to exhibit significant puncture resistance, to enable a secondary mechanism of stress response in these systems. Overall, the development of such a composite, protective material has tremendous potential to enhance material safety and dependability.

REFERENCES

[1] Stuart, M. A. C., Huck, W. T. S., Genzer, J., Muller, M., Ober, C., Stamm, M., Sukhorukov, G. B., Szleifer, I., Tsukruk, V. V., Urban, M., Winnik, F., Zauscher, S., Luzinov, I., and Minko, S., ‘‘Emerging applications of stimuli-responsive polymer materials,’’ Nature Materials **9**, 101-113 (2010).

[2] Schattling, P., Jochum, F. D., and Theato, P., ‘‘Multi-stimuli responsive polymers - the all-in-one talents,’’ Polymer Chemistry **5**, 25-36 (2014).

[3] Wu, D. Y., Meure, S., and Solomon, D., ‘‘Self-healing polymeric materials: A review of recent developments,’’ Progress in Polymer Science **33**, 479-522 (2008).

[4] Jud, K., Kausch, H. H., and Williams, J. G., ‘‘Fracture-Mechanics Studies of Crack Healing and Welding of Polymers,’’ Journal of Materials Science **16**, 204-210 (1981).

[5] Blaiszik, B. J., Kramer, S. L. B., Olugebefola, S. C., Moore, J. S., Sottos, N. R., and White, S. R., ‘‘Self-Healing Polymers and Composites,’’ Annual Review of Materials Research, Vol 40 **40**, 179-211 (2010).

[6] White, S. R., Sottos, N. R., Geubelle, P. H., Moore, J. S., Kessler, M. R., Sriram, S. R., Brown, E. N., and Viswanathan, S., ‘‘Autonomic healing of polymer composites,’’ Nature **409**, 794-797 (2001).

[7] Toohey, K. S., Sottos, N. R., Lewis, J. A., Moore, J. S., and White, S. R., ‘‘Self-healing materials with microvascular networks,’’ Nature Materials **6**, 581-585 (2007).

[8] Kloxin, C. J., and Bowman, C. N., ‘‘Covalent adaptable networks: smart, reconfigurable and responsive network systems,’’ Chemical Society Reviews **42**, 7161-7173 (2013).

[9] Kloxin, C. J., Scott, T. F., Adzima, B. J., and Bowman, C. N., ‘‘Covalent Adaptable Networks (CANS): A Unique Paradigm in Cross-Linked Polymers,’’ Macromolecules **43**, 2643-2653 (2010).

[10] Montarnal, D., Capelot, M., Tournilhac, F., and Leibler, L., ‘‘Silica-Like Malleable Materials from Permanent Organic Networks,’’ Science **334**, 965-968 (2011).

[11] Chen, X. X., Dam, M. A., Ono, K., Mal, A., Shen, H. B., Nutt, S. R., Sheran, K., and Wudl, F., ‘‘A thermally re-mendable cross-linked polymeric material,’’ Science **295**, 1698-1702 (2002).

[12] Habault, D., Zhang, H. J., and Zhao, Y., ‘‘Light-triggered self-healing and shape-memory polymers,’’ Chemical Society Reviews **42**, 7244-7256 (2013).

[13] Ling, J., Rong, M. Z., and Zhang, M. Q., ‘‘Coumarin imparts repeated photochemical remendability to polyurethane,’’ Journal of Materials Chemistry **21**, 18373-18380 (2011).

[14] Chung, C. M., Roh, Y. S., Cho, S. Y., and Kim, J. G., ‘‘Crack healing in polymeric materials via photochemical [2+2] cycloaddition,’’ Chemistry of Materials **16**, 3982-+ (2004).

[15] Amamoto, Y., Kamada, J., Otsuka, H., Takahara, A., and Matyjaszewski, K., ‘‘Repeatable Photoinduced Self-Healing of Covalently Cross-Linked Polymers through Reshuffling of Trithiocarbonate Units,’’ Angewandte Chemie-International Edition **50**, 1660-1663 (2011).

[16] Amamoto, Y., Otsuka, H., Takahara, A., and Matyjaszewski, K., ‘‘Self-Healing of Covalently Cross-Linked Polymers by Reshuffling Thiuram Disulfide Moieties in Air under Visible Light,’’ Advanced Materials **24**, 3975-3980 (2012).

[17] Scott, T. F., Schneider, A. D., Cook, W. D., and Bowman, C. N., ‘‘Photoinduced plasticity in cross-linked polymers,’’ Science **308**, 1615-1617 (2005).

[18] Kloxin, C. J., Scott, T. F., Park, H. Y., and Bowman, C. N., ‘‘Mechanophotopatterning on a Photoresponsive Elastomer,’’ Advanced Materials **23**, 1977-1981 (2011).

[19] Caruso, M. M., Davis, D. A., Shen, Q., Odom, S. A., Sottos, N. R., White, S. R., and Moore, J. S., ‘‘Mechanically-Induced Chemical Changes in Polymeric Materials,’’ Chemical Reviews **109**, 5755-5798 (2009).

[20] Black, A. L., Lenhardt, J. M., and Craig, S. L., ‘‘From molecular mechanochemistry to stress-responsive materials,’’ Journal of Materials Chemistry **21**, 1655-1663 (2011).

[21] Hickenboth, C. R., Moore, J. S., White, S. R., Sottos, N. R., Baudry, J., and Wilson, S. R., ‘‘Biasing reaction pathways with mechanical force,’’ Nature **446**, 423-427 (2007).

[22] Davis, D. A., Hamilton, A., Yang, J. L., Cremar, L. D., Van Gough, D., Potisek, S. L., Ong, M. T., Braun, P. V., Martinez, T. J., White, S. R., Moore, J. S., and Sottos, N. R., ‘‘Force-induced activation of covalent bonds in mechanoresponsive polymeric materials,’’ Nature **459**, 68-72 (2009).

[23] Ramirez, A. L. B., Kean, Z. S., Orlicki, J. A., Champhekar, M., Elsakr, S. M., Krause, W. E., and Craig, S. L., ‘‘Mechanochemical strengthening of a synthetic polymer in response to typically destructive shear forces,’’ Nature Chemistry **5**, 757-761 (2013).

[24] Ramachandran, D., Liu, F., and Urban, M. W., ‘‘Self-repairable copolymers that change color,’’ Rsc Advances **2**, 135-143 (2012).

[25] Leunissen, M. E., Christova, C. G., Hynninen, A. P., Royall, C. P., Campbell, A. I., Imhof, A., Dijkstra, M., van Roij, R., and van Blaaderen, A., ‘‘Ionic colloidal crystals of oppositely charged particles,’’ Nature **437**, 235-240 (2005).

[26] Yethiraj, A., and van Blaaderen, A., ‘‘A colloidal model system with an interaction tunable from hard sphere to soft and dipolar,’’ Nature **421**, 513-517 (2003).

[27] Eberle, A. P. R., Castaneda-Priego, R., Kim, J. M., and Wagner, N. J., ‘‘Dynamical Arrest, Percolation, Gelation, and Glass Formation in Model Nanoparticle Dispersions with Thermoreversible Adhesive Interactions,’’ Langmuir **28**, 1866-1878 (2012).

[28] Vanhelden, A. K., Jansen, J. W., and Vrij, A., ‘‘Preparation and Characterization of Spherical Monodisperse Silica Dispersions in Non-Aqueous Solvents,’’ Journal of Colloid and Interface Science **81**, 354-368 (1981).

[29] Chen, M., and Russel, W. B., ‘‘Characteristics of Flocculated Silica Dispersions,’’ Journal of Colloid and Interface Science **141**, 564-577 (1991).

[30] Woutersen, A. T. J. M., and Dekruif, C. G., ‘‘The Rheology of Adhesive Hard-Sphere Dispersions,’’ Journal of Chemical Physics **94**, 5739-5750 (1991).

[31] Grant, M. C., and Russel, W. B., ‘‘Volume-Fraction Dependence of Elastic-Moduli and Transition-Temperatures for Colloidal Silica-Gels,’’ Physical Review E **47**, 2606-2614 (1993).

[32] Rueb, C. J., and Zukoski, C. F., ‘‘Viscoelastic properties of colloidal gels,’’ Journal of Rheology **41**, 197-218 (1997).

[33] Rueb, C. J., and Zukoski, C. F., ‘‘Rheology of suspensions of weakly attractive particles: Approach to gelation,’’ Journal of Rheology **42**, 1451-1476 (1998).

[34] Rouw, P. W., and Dekruif, C. G., ‘‘Adhesive Hard-Sphere Colloidal Dispersions .1. Diffusion-Coefficient as a Function of Well Depth,’’ Journal of Chemical Physics **88**, 7799-7806 (1988).

[35] Eberle, A. P. R., Wagner, N. J., and Castaneda-Priego, R., ‘‘Dynamical Arrest Transition in Nanoparticle Dispersions with Short-Range Interactions,’’ Physical Review Letters **106** (2011).

[36] Kim, J. M., Eberle, A. P. R., Gurnon, A. K., Porcar, L., and Wagner, N. J., ‘‘The microstructure and rheology of a model, thixotropic nanoparticle gel under steady shear and large amplitude oscillatory shear (LAOS),’’ Journal of Rheology **58**, 1301-1328 (2014).

[37] Ramakrishnan, S., and Zukoski, C. F., ‘‘Microstructure and rheology of thermoreversible nanoparticle gels,’’ Langmuir **22**, 7833-7842 (2006).

[38] Solomon, M. J., and Varadan, P., ‘‘Dynamic structure of thermoreversible colloidal gels of adhesive spheres,’’ Physical Review E **63** (2001).

[39] Eberle, A. P. R., Wagner, N. J., Akgun, B., and Satija, S. K., ‘‘Temperature-Dependent Nanostructure of an End-Tethered Octadecane Brush in Tetradecane and Nanoparticle Phase Behavior,’’ Langmuir **26**, 3003-3007 (2010).

[40] Cipelletti, L., and Ramos, L., ‘‘Slow dynamics in glasses, gels and foams,’’ Current Opinion in Colloid & Interface Science **7**, 228-234 (2002).

[41] Guo, H. Y., Ramakrishnan, S., Harden, J. L., and Leheny, R. L., ‘‘Gel formation and aging in weakly attractive nanocolloid suspensions at intermediate concentrations,’’ Journal of Chemical Physics **135** (2011).

[42] Petekidis, G., ‘‘Rheology of colloidal gels,’’ Journal of Rheology **58**, 1085-1087 (2014).

[43] Royall, C. P., Williams, S. R., Ohtsuka, T., and Tanaka, H., ‘‘Direct observation of a local structural mechanism for dynamic arrest,’’ Nature Materials **7**, 556-561 (2008).

[44] Zia, R. N., Landrum, B. J., and Russel, W. B., ‘‘A micro-mechanical study of coarsening and rheology of colloidal gels: Cage building, cage hopping, and Smoluchowski's ratchet,’’ Journal of Rheology **58**, 1121-1157 (2014).

[45] Gordon, M. B., French, J. M., Wagner, N. J., and Kloxin, C. J., ‘‘Dynamic Bonds in Covalently Crosslinked Polymer Networks for Photoactivated Strengthening and Healing,’’ Adv Mater **27**, 8007-10 (2015).

[46] Fiore, G. L., Rowan, S. J., and Weder, C., ‘‘Optically healable polymers,’’ Chemical Society Reviews **42**, 7278-7288 (2013).

[47] Urban, A. M., and Urban, M. W., ‘‘Stimuli-responsive macromolecules and polymeric coatings,’’ Stimuli-Responsive Polymeric Films and Coatings **912**, 1-25 (2005).

[48] Liu, C., Qin, H., and Mather, P. T., ‘‘Review of progress in shape-memory polymers,’’ Journal of Materials Chemistry **17**, 1543-1558 (2007).

[49] Lendlein, A., and Kelch, S., ‘‘Shape-memory polymers,’’ Angewandte Chemie-International Edition **41**, 2034-2057 (2002).

[50] Wojtecki, R. J., Meador, M. A., and Rowan, S. J., ‘‘Using the dynamic bond to access macroscopically responsive structurally dynamic polymers,’’ Nature Materials **10**, 14-27 (2011).

[51] Chatani, S., Kloxin, C. J., and Bowman, C. N., ‘‘The power of light in polymer science: photochemical processes to manipulate polymer formation, structure, and properties,’’ Polym. Chem. **5**, 2187-2201 (2014).

[52] Lendlein, A., Jiang, H. Y., Junger, O., and Langer, R., ‘‘Light-induced shape-memory polymers,’’ Nature **434**, 879-882 (2005).

[53] Zheng, Y. J., Andreopoulos, F. M., Micic, M., Huo, Q., Pham, S. M., and Leblanc, R. M., ‘‘A novel photoscissile poly(ethylene glycol)-based hydrogel,’’ Advanced Functional Materials **11**, 37-40 (2001).

[54] Ling, J., Rong, M. Z., and Zhang, M. Q., ‘‘Photo-stimulated self-healing polyurethane containing dihydroxyl coumarin derivatives,’’ Polymer **53**, 2691-2698 (2012).

[55] Froimowicz, P., Frey, H., and Landfester, K., ‘‘Towards the Generation of Self-Healing Materials by Means of a Reversible Photo-induced Approach,’’ Macromolecular Rapid Communications **32**, 468-473 (2011).

[56] Connal, L. A., Vestberg, R., Hawker, C. J., and Qiao, G. G., ‘‘Fabrication of Reversibly Crosslinkable, 3-Dimensionally Conformal Polymeric Microstructures,’’ Advanced Functional Materials **18**, 3315-3322 (2008).

[57] Yildiz, U., Hazer, B., and Tauer, K., ‘‘Tailoring polymer architectures with macromonomer azoinitiators,’’ Polym. Chem. **3**, 1107-1118 (2012).

[58] Otsu, T., ‘‘Iniferter concept and living radical polymerization,’’ Journal of Polymer Science Part a-Polymer Chemistry **38**, 2121-2136 (2000).

[59] Zhou, H. X., and Johnson, J. A., ‘‘Photo-controlled Growth of Telechelic Polymers and End-linked Polymer Gels,’’ Angew Chem Int Ed. **52**, 2235-2238 (2013).

[60] Nair, D. P., Cramer, N. B., Gaipa, J. C., McBride, M. K., Matherly, E. M., McLeod, R. R., Shandas, R., and Bowman, C. N., ‘‘Two-Stage Reactive Polymer Network Forming Systems,’’ Advanced Functional Materials **22**, 1502-1510 (2012).

[61] Ma, S. J., Mannino, S. J., Wagner, N. J., and Kloxin, C. J., ‘‘Photodirected Formation and Control of Wrinkles on a Thiol-ene Elastomer,’’ Acs Macro Letters **2**, 474-477 (2013).

[62] Tan, Y. S., Sudlow, A. L., Molloy, K. C., Morishima, Y., Fujisawa, K., Jackson, W. J., Henderson, W., Halim, S. N. B. A., Ng, S. W., and Tiekink, E. R. T., ‘‘Supramolecular Isomerism in a Cadmium Bis(N-Hydroxyethyl, N-isopropyldithiocarbamate) Compound: Physiochemical Characterization of Ball (n=2) and Chain (n = infinity) Forms of {Cd[S2CN(iPr)CH2CH2OH](2)center dot solvent}(n),’’ Crystal Growth & Design **13**, 3046-3056 (2013).

[63] Gillespie, P. G., and Walker, R. G., ‘‘Molecular basis of mechanosensory transduction,’’ Nature **413**, 194-202 (2001).

[64] French, A. S., ‘‘Mechanotransduction,’’ Annual Review of Physiology **54**, 135-152 (1992).

[65] Turner, C. H., and Pavalko, F. M., ‘‘Mechanotransduction and functional response of the skeleton to physical stress: the mechanisms and mechanics of bone adaptation,’’ J Orthop Sci **3**, 346-55 (1998).

[66] Flosdorf, E. W., and Chambers, L. A., ‘‘The chemical action of audible sound,’’ Journal of the American Chemical Society **55**, 3051-3052 (1933).

[67] Lavalle, P., Boulmedais, F., Schaaf, P., and Jierry, L., ‘‘Soft-Mechanochemistry: Mechanochemistry Inspired by Nature,’’ Langmuir **32**, 7265-76 (2016).

[68] Robb, M. J., and Moore, J. S., ‘‘A Retro-Staudinger Cycloaddition: Mechanochemical Cycloelimination of a beta-Lactam Mechanophore,’’ Journal of the American Chemical Society **137**, 10946-10949 (2015).

[69] Chen, Y. L., Spiering, A. J. H., Karthikeyan, S., Peters, G. W. M., Meijer, E. W., and Sijbesma, R. P., ‘‘Mechanically induced chemiluminescence from polymers incorporating a 1,2-dioxetane unit in the main chain,’’ Nature Chemistry **4**, 559-562 (2012).

[70] Kryger, M. J., Ong, M. T., Odom, S. A., Sottos, N. R., White, S. R., Martinez, T. J., and Moore, J. S., ‘‘Masked Cyanoacrylates Unveiled by Mechanical Force,’’ Journal of the American Chemical Society **132**, 4558-+ (2010).

[71] Kean, Z. S., Niu, Z. B., Hewage, G. B., Rheingold, A. L., and Craig, S. L., ‘‘Stress-Responsive Polymers Containing Cyclobutane Core Mechanophores: Reactivity and Mechanistic Insights,’’ Journal of the American Chemical Society **135**, 13598-13604 (2013).

[72] Potisek, S. L., Davis, D. A., Sottos, N. R., White, S. R., and Moore, J. S., ‘‘Mechanophore-linked addition polymers,’’ Journal of the American Chemical Society **129**, 13808-+ (2007).

[73] Lenhardt, J. M., Ong, M. T., Choe, R., Evenhuis, C. R., Martinez, T. J., and Craig, S. L., ‘‘Trapping a Diradical Transition State by Mechanochemical Polymer Extension,’’ Science **329**, 1057-1060 (2010).

[74] Lee, B., Niu, Z. B., Wang, J. P., Slebodnick, C., and Craig, S. L., ‘‘Relative Mechanical Strengths of Weak Bonds in Sonochemical Polymer Mechanochemistry,’’ Journal of the American Chemical Society **137**, 10826-10832 (2015).

[75] Gordon, M. B., Kloxin, C. J., and Wagner, N. J., ‘‘The rheology and microstructure of an aging thermoreversible colloidal gel,’’ Journal of Rheology, Accepted (2017).

[76] Jabbari-Farouji, S., Wegdam, G. H., and Bonn, D., ‘‘Gels and glasses in a single system: Evidence for an intricate free-energy landscape of glassy materials,’’ Physical Review Letters **99** (2007).

[77] Lacks, D. J., and Osborne, M. J., ‘‘Energy landscape picture of overaging and rejuvenation in a sheared glass,’’ Physical Review Letters **93** (2004).

[78] Eberle, A. P. R., and Porcar, L., ‘‘Flow-SANS and Rheo-SANS applied to soft matter,’’ Current Opinion in Colloid & Interface Science **17**, 33-43 (2012).

[79] Zaccarelli, E., ‘‘Colloidal gels: equilibrium and non-equilibrium routes,’’ Journal of Physics-Condensed Matter **19** (2007).

[80] Negi, A. S., Redmon, C. G., Ramakrishnan, S., and Osuji, C. O., ‘‘Viscoelasticity of a colloidal gel during dynamical arrest: Evolution through the critical gel and comparison with a soft colloidal glass,’’ Journal of Rheology **58**, 1557-1579 (2014).

[81] Asakura, S., and Oosawa, F., ‘‘Interaction between Particles Suspended in Solutions of Macromolecules,’’ Journal of Polymer Science **33**, 183-192 (1958).

[82] Poon, W. C. K., Starrs, L., Meeker, S. P., Moussaid, A., Evans, R. M. L., Pusey, P. N., and Robins, M. M., ‘‘Delayed sedimentation of transient gels in colloid-polymer mixtures: dark-field observation, rheology and dynamic light scattering studies,’’ Faraday Discussions **112**, 143-154 (1999).

[83] Buscall, R., Choudhury, T. H., Faers, M. A., Goodwin, J. W., Luckham, P. A., and Partridge, S. J., ‘‘Towards rationalising collapse times for the delayed sedimentation of weakly-aggregated colloidal gels,’’ Soft Matter **5**, 1345-1349 (2009).

[84] Lu, P. J., Zaccarelli, E., Ciulla, F., Schofield, A. B., Sciortino, F., and Weitz, D. A., ‘‘Gelation of particles with short-range attraction,’’ Nature **453**, 499-U4 (2008).

[85] Verhaegh, N. A. M., Asnaghi, D., Lekkerkerker, H. N. W., Giglio, M., and Cipelletti, L., ‘‘Transient gelation by spinodal decomposition in colloid-polymer mixtures,’’ Physica A **242**, 104-118 (1997).

[86] Zhang, I., Royall, C. P., Faers, M. A., and Bartlett, P., ‘‘Phase separation dynamics in colloid-polymer mixtures: the effect of interaction range,’’ Soft Matter **9**, 2076-2084 (2013).

[87] Koumakis, N., Moghimi, E., Besseling, R., Poon, W. C. K., Brady, J. F., and Petekidis, G., ‘‘Tuning colloidal gels by shear,’’ Soft Matter **11**, 4640-4648 (2015).

[88] Kim, J. M., Fang, J., Eberle, A. P. R., Castaneda-Priego, R., and Wagner, N. J., ‘‘Gel Transition in Adhesive Hard-Sphere Colloidal Dispersions: The Role of Gravitational Effects,’’ Physical Review Letters **110** (2013).

[89] Teece, L. J., Faers, M. A., and Bartlett, P., ‘‘Ageing and collapse in gels with long-range attractions,’’ Soft Matter **7**, 1341-1351 (2011).

[90] Dymond, J. H., and Oye, H. A., ‘‘Viscosity of Selected Liquid N-Alkanes,’’ Journal of Physical and Chemical Reference Data **23**, 41-53 (1994).

[91] Porcar, L., Pozzo, D., Langenbucher, G., Moyer, J., and Butler, P. D., ‘‘Rheo-small-angle neutron scattering at the National Institute of Standards and Technology Center for Neutron Research,’’ Review of Scientific Instruments **82** (2011).

[92] Kline, S. R., ‘‘Reduction and analysis of SANS and USANS data using IGOR Pro,’’ Journal of Applied Crystallography **39**, 895-900 (2006).

[93] Winter, H. H., and Chambon, F., ‘‘Analysis of Linear Viscoelasticity of a Cross-Linking Polymer at the Gel Point,’’ Journal of Rheology **30**, 367-382 (1986).

[94] Valadez-Perez, N. E., Liu, Y., Eberle, A. P. R., Wagner, N. J., and Castaneda-Priego, R., ‘‘Dynamical arrest in adhesive hard-sphere dispersions driven by rigidity percolation,’’ Physical Review E **88** (2013).

[95] Pusey, P. N., and Vanmegen, W., ‘‘Observation of a Glass-Transition in Suspensions of Spherical Colloidal Particles,’’ Physical Review Letters **59**, 2083-2086 (1987).

[96] Mason, T. G., and Weitz, D. A., ‘‘Linear Viscoelasticity of Colloidal Hard-Sphere Suspensions near the Glass-Transition,’’ Physical Review Letters **75**, 2770-2773 (1995).

[97] Helgeson, M. E., Wagner, N. J., and Vlassopoulos, D., ‘‘Viscoelasticity and shear melting of colloidal star polymer glasses,’’ Journal of Rheology **51**, 297-316 (2007).

[98] Gotze, W., and Sjogren, L., ‘‘Beta-Relaxation at the Glass-Transition of Hard-Spherical Colloids,’’ Physical Review A **43**, 5442-5448 (1991).

[99] Baravian, C., and Quemada, D., ‘‘Using instrumental inertia in controlled stress rheometry,’’ Rheologica Acta **37**, 223-233 (1998).

[100] McKenna, G. B., Narita, T., and Lequeux, F., ‘‘Soft colloidal matter: A phenomenological comparison of the aging and mechanical responses with those of molecular glasses,’’ Journal of Rheology **53**, 489-516 (2009).

[101] Kovacs, A. J., Stratton, R. A., and Ferry, J. D., ‘‘Dynamic Mechanical Properties of Polyvinyl Acetate in Shear in Glass Transition Temperature Range,’’ Journal of Physical Chemistry **67**, 152-& (1963).

[102] Chen, Y. L., and Schweizer, K. S., ‘‘Microscopic theory of gelation and elasticity in polymer-particle suspensions,’’ Journal of Chemical Physics **120**, 7212-7222 (2004).

[103] Ramakrishnan, S., Chen, Y. L., Schweizer, K. S., and Zukoski, C. F., ‘‘Elasticity and clustering in concentrated depletion gels,’’ Physical Review E **70** (2004).

[104] Eberle, A. P. R., Martys, N., Porcar, L., Kline, S. R., George, W. L., Kim, J. M., Butler, P. D., and Wagner, N. J., ‘‘Shear viscosity and structural scalings in model adhesive hard-sphere gels,’’ Physical Review E **89** (2014).

[105] Peng, X. G., and McKenna, G. B., ‘‘Comparison of the physical aging behavior of a colloidal glass after shear melting and concentration jumps,’’ Physical Review E **90** (2014).

[106] Siebenburger, M., Ballauff, M., and Voigtmann, T., ‘‘Creep in Colloidal Glasses,’’ Physical Review Letters **108** (2012).

[107] Giordano, V. M., and Ruta, B., ‘‘Unveiling the structural arrangements responsible for the atomic dynamics in metallic glasses during physical aging,’’ Nature Communications **7** (2016).

[108] ‘‘Directing Matter and Energy: Five Challenges for Science and the Imagination,’’ Basic Energy Sciences Advisory Committee Report, U.S. Department of Energy (2007).

[109] Joshi, Y. M., ‘‘Dynamics of Colloidal Glasses and Gels,’’ Annual Review of Chemical and Biomolecular Engineering, Vol 5 **5**, 181-202 (2014).

[110] Lu, P. J., and Weitz, D. A., ‘‘Colloidal Particles: Crystals, Glasses, and Gels,’’ Annual Review of Condensed Matter Physics, Vol 4 **4**, 217-233 (2013).

[111] Abou, B., Bonn, D., and Meunier, J., ‘‘Aging dynamics in a colloidal glass,’’ Physical Review E **64** (2001).

[112] Cipelletti, L., and Ramos, L., ‘‘Slow dynamics in glassy soft matter,’’ Journal of Physics-Condensed Matter **17**, R253-R285 (2005).

[113] Abou, B., and Gallet, F., ‘‘Probing a nonequilibrium Einstein relation in an aging colloidal glass,’’ Physical Review Letters **93** (2004).

[114] Bonn, D., Tanase, S., Abou, B., Tanaka, H., and Meunier, J., ‘‘Laponite: Aging and shear rejuvenation of a colloidal glass,’’ Physical Review Letters **89** (2002).

[115] Joshi, Y. M., and Reddy, G. R. K., ‘‘Aging in a colloidal glass in creep flow: Time-stress superposition,’’ Physical Review E **77** (2008).

[116] Bandyopadhyay, R., Mohan, P. H., and Joshi, Y. M., ‘‘Stress relaxation in aging soft colloidal glasses,’’ Soft Matter **6**, 1462-1466 (2010).

[117] Erwin, B. M., Vlassopoulos, D., and Cloitre, M., ‘‘Rheological fingerprinting of an aging soft colloidal glass,’’ Journal of Rheology **54**, 915-939 (2010).

[118] Rogers, S. A., Vlassopoulos, D., and Callaghan, P. T., ‘‘Aging, yielding, and shear banding in soft colloidal glasses,’’ Physical Review Letters **100** (2008).

[119] Pham, K. N., Egelhaaf, S. U., Pusey, P. N., and Poon, W. C. K., ‘‘Glasses in hard spheres with short-range attraction,’’ Physical Review E **69** (2004).

[120] Pham, K. N., Petekidis, G., Vlassopoulos, D., Egelhaaf, S. U., Poon, W. C. K., and Pusey, P. N., ‘‘Yielding behavior of repulsion- and attraction-dominated colloidal glasses,’’ Journal of Rheology **52**, 649-676 (2008).

[121] Koumakis, N., and Petekidis, G., ‘‘Two step yielding in attractive colloids: transition from gels to attractive glasses,’’ Soft Matter **7**, 2456-2470 (2011).

[122] Stiakakis, E., Wilk, A., Kohlbrecher, J., Vlassopoulos, D., and Petekidis, G., ‘‘Slow dynamics, aging, and crystallization of multiarm star glasses,’’ Physical Review E **81** (2010).

[123] Cianci, G. C., Courtland, R. E., and Weeks, E. R., ‘‘Correlations of structure and dynamics in an aging colloidal glass,’’ Solid State Communications **139**, 599-604 (2006).

[124] Puertas, A. M., Fuchs, M., and Cates, M. E., ‘‘Aging in attraction-driven colloidal glasses,’’ Physical Review E **75** (2007).

[125] Sollich, P., Lequeux, F., Hebraud, P., and Cates, M. E., ‘‘Rheology of soft glassy materials,’’ Physical Review Letters **78**, 2020-2023 (1997).

[126] Viasnoff, V., and Lequeux, F., ‘‘Rejuvenation and overaging in a colloidal glass under shear,’’ Physical Review Letters **89** (2002).

[127] McKenna, G. B., ‘‘Mechanical rejuvenation in polymer glasses: fact or fallacy?,’’ Journal of Physics-Condensed Matter **15**, S737-S763 (2003).

[128] Street, C. B., Yarovoy, Y., Wagner, N. J., Vethamuthu, M. S., Hermanson, K. D., and Ananthapadmanabhan, K. P., ‘‘TDNMR characterization of a model crystallizing surfactant system,’’ Colloids and Surfaces a-Physicochemical and Engineering Aspects **406**, 13-23 (2012).

[129] Ducrot, E., Chen, Y. L., Bulters, M., Sijbesma, R. P., and Creton, C., ‘‘Toughening Elastomers with Sacrificial Bonds and Watching Them Break,’’ Science **344**, 186-189 (2014).

[130] Mondal, K., ‘‘Olefin Metathesis in Carbohydrate and Norbornene Applications,’’ University of Florida Dissertation (2007).

[131] Larsen, M. B., and Boydston, A. J., ‘‘Successive Mechanochemical Activation and Small Molecule Release in an Elastomeric Material,’’ Journal of the American Chemical Society **136**, 1276-1279 (2014).

[132] Johnson, R. S., Washburn, C. M., Staton, A. W., Moorman, M. W., Manginell, R. P., Dugger, M. T., and Dirk, S. M., ‘‘Thermally-Activated Pentanol Delivery from Precursor Poly(p-phenylenevinylene)s for MEMS Lubrication,’’ Macromolecular Rapid Communications **33**, 1346-1350 (2012).

Appendix A

SUPPORTING INFORMATION FOR PHOTO-ACTIVE HEALING NETWORK

A.1 UV-Vis Spectrum for LBCL

As stated in Chapter 2, UV-Vis measurements of the LBCL diol (1 mg/mL) were conducted using a NanoDrop 2000 Spectrophotometer from Thermo Scientific. The UV-Vis spectrum shows that the LBCL strongly absorbs 320-380 nm light as shown in Figure A.1.

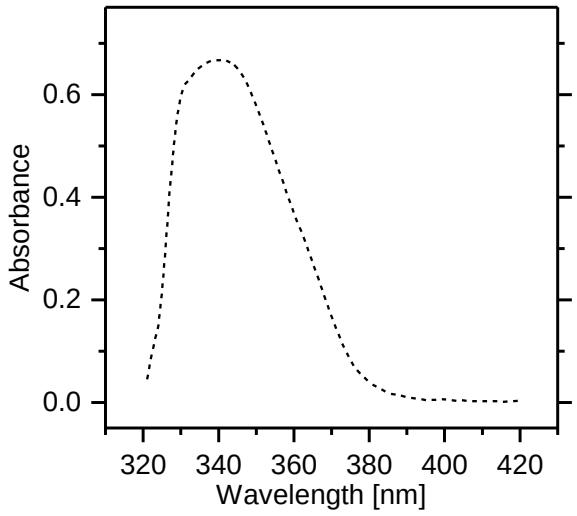

Figure A.1 UV-Vis spectrum of LBCL diol. The monomer absorbs 365 nm UV light.

A.2 NMR Spectra for LCBL

NMR spectra were obtained from a Bruker AV 400 NMR Spectrometer as shown in Figure A.2 and Figure A.3.

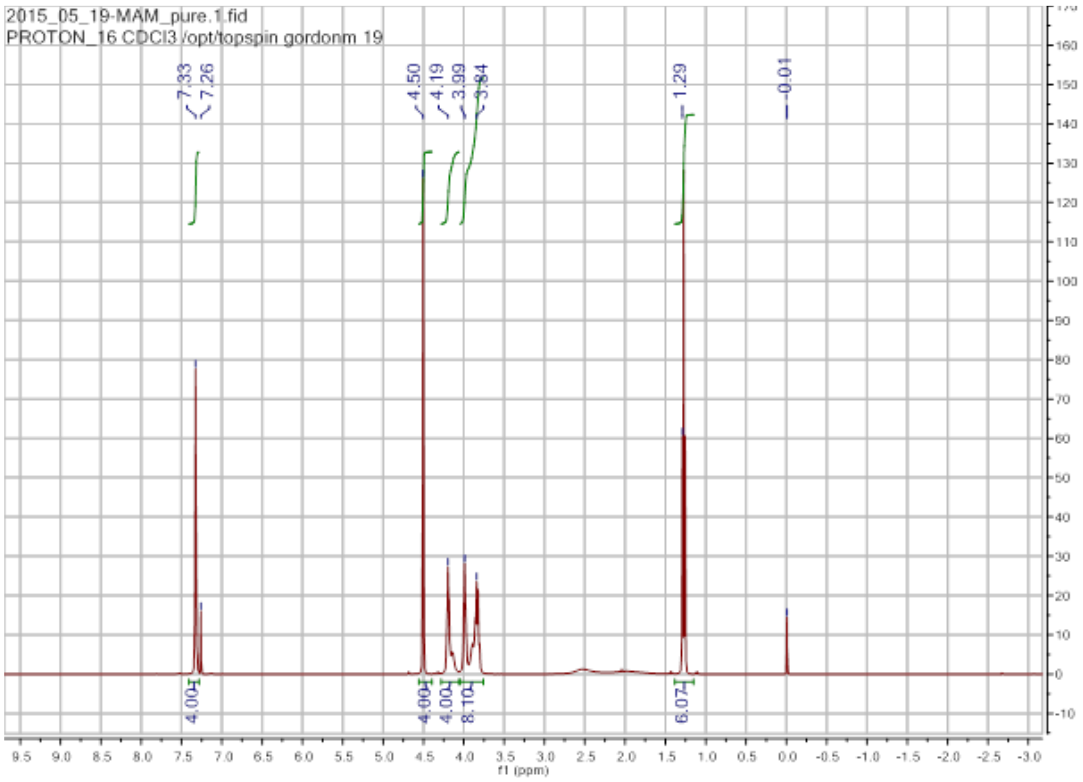

Figure A.2: ^{1}H NMR of LBCL.

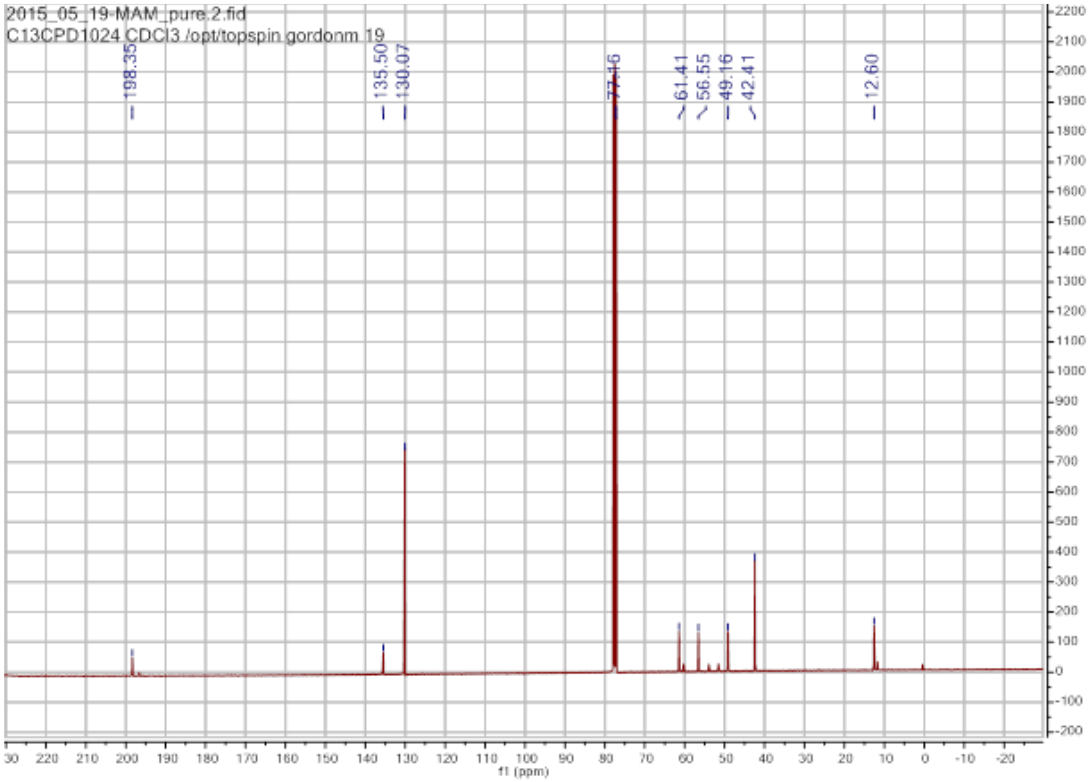

Figure A.3: ^{13}C NMR of LBCL.

A.3 FTIR Spectra

All samples went to nearly full conversion as shown in Figure A.4. The baseline in the spectra was corrected using the automatic correction in the Omnic Software for the range shown in Figure A.4.

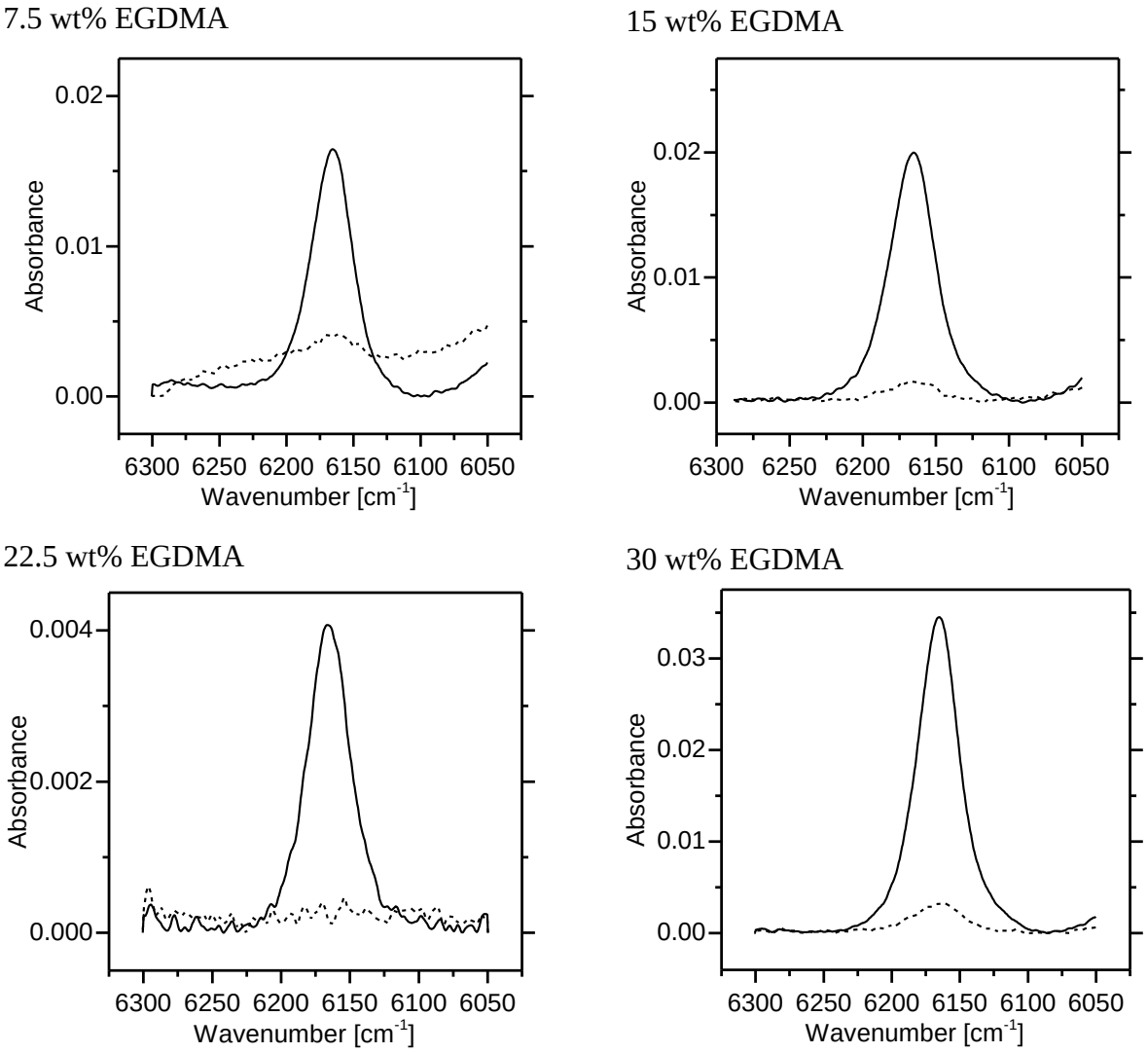

Figure A.4: FTIR spectra before (solid line) and after (dashed line) two hours of irradiation.

Appendix B

NORBORNENE-BASED PHOTO-ACTIVE HEALING MATERIAL

B.1 Introduction and Objectives

This chapter describes prior work that led to the development photo-active network presented in Chapter 2. The objective of this project was to develop a novel, light-active polymer system by employing a molecular-level design based on the incorporation of xanthate units which allow for rearrangement. We hypothesized that the dixanthogen unit would dissociate under UV light, leading to formation of S-based radicals, to enable bond rearrangement, stress relaxation and macroscopic healing. A schematic is shown in Figure B.1.

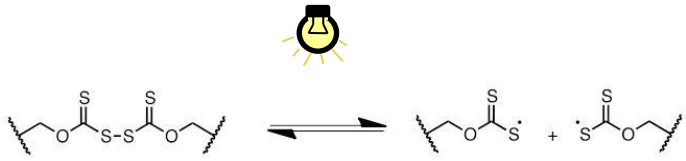

Figure B.1: We hypothesized that sulfur radicals would form under UV light causing bond rearrangement, stress relaxation and healing.

To accomplish this, the project was divided into 4 main stages: 1) monomer design, 2) monomer synthesis and purification, 3) polymerization and 4) material testing and characterization.

B.2 Monomer Design

The photo-active monomer structure contains a dixanthogen group (colored green in Figure B.2). These units are commonly used as chain transfer agents in reversible addition-fragmentation chain transfer (RAFT) polymerizations, which are capable of undergoing reversible chain transfer reactions. When incorporated into a polymer network, we hypothesize this group will allow for photo-activated bond rearrangements and healing. Norbornene rings (colored purple in Figure B.2) were chosen as the polymerizable end group since their reaction mechanism is chemically orthogonal to the radical-based rearrangement.

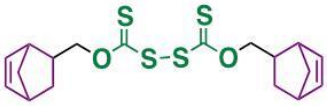

Figure B.2: Monomer design for photo-active healing network.

For more information on the decision to synthesize this monomer, see Attempt #1 through #4.

B.3 Monomer Synthesis and Purification

The synthesis steps are shown in Figure B.3.

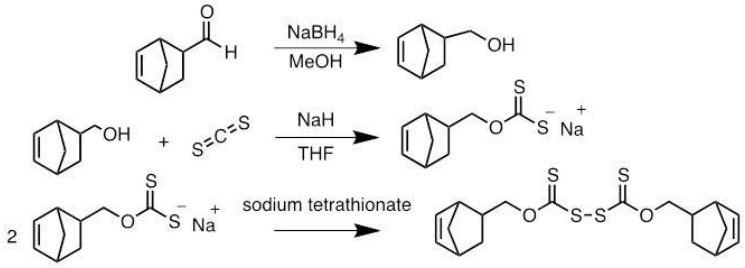

Figure B.3: Synthetic steps for the formation of the photo-active monomer described above.

To synthesize the norbornene alcohol, 7 g $NaBH_4$ (0.19 mol) was added to a solution of 6.64 g of NaOH (0.17 mol) in 80 mL water at 0°C under argon. A solution of norbornene-1-carboxaldehyde (47 g, 0.385 mol) in 232 mL methanol was added dropwise to the $NaBH_4$ suspension at 0°C. The reaction was warmed to room temperature as it reacted overnight. The solution was neutralized at 0°C with 30% H_2SO_4 before the methanol was removed. The remainder was dissolved in diethyl ether and washed with $NaHCO_3$ (3x) and brine (3x). The organic layer was dried with magnesium sulfate, filtered and concentrated resulting in a 72% yield of purified norbornene alcohol as a clear liquid. This procedure was from reference [130].

To synthesize the anion, NaH in mineral oil (8.00 g, 0.20 mol) was carefully transferred to a round bottom, dissolved in 300 mL n-hexane and mixed for several minutes to remove the mineral oil. After mixing, the pure NaH precipitated from the solution which was removed. This process was repeated twice. The pure NaH was then dissolved in 260 mL THF and 12.4 g of norbornene alcohol (0.10 mol) was subsequently added. The solution was put on ice and 12.09 mL of CS_2 (0.20 mol) was added dropwise and reacted for 4.5 hours. After this time, the solution became orange (pH=9). The solution was neutralized with 1M HCl, yielding a red solution and deep red precipitate, which was removed by filtration. The THF in the filtrate was subsequently evaporated resulting in a yellow-orange solid anion. The anion was dissolved in 50 mL of water. Sodium tetrathionate (15 g, 0.05 mol) was dissolved in 50 mL water and added dropwise to the aqueous anion solution. A yellow-orange precipitate immediately formed and the reaction continued for three hours. The precipitate was isolated, dissolved in DCM and washed with water (3x). The organic phase was dried with magnesium sulfate, filtered and concentrated to yield a yellow liquid product. The product was purified by column

chromatography (gradient from 0-5% ethyl acetate in hexanes) to afford the purified disulfide as a yellow liquid (44% yield). The liquid solidified within two days as the small amounts of solvent evaporated (mass spectrometry results: expected=398.05, observed=398.05).

For more information about the development of this procedure, see Attempt #2 through #7.

B.4 Polymerization and Network Formation

The network was formed using ring-opening metathesis polymerization (ROMP), which is driven by the relief of strain in ring structures and is chemically orthogonal to the radical-based rearrangement. (For more information about why a chemically orthogonal polymerization scheme was required, see Previous Attempt #1 where an orthogonal polymerization scheme was not used). The reaction was catalyzed using Grubbs second generation catalyst. To form the network, the disulfide was polymerized with cyclooctene, which also served as the solvent. (For more information regarding the incorporation of cyclooctene, see Attempt #8.)

First, 0.005 g Grubbs catalyst was dissolved in 5 mL cyclooctene. Then, 2 mL of this solution was rapidly mixed with the corresponding amount of disulfide (see Table B.1). The solution was quickly transferred by pipette and cast between two glass slides separated by a $1/16^{th}$ inch shim held by binder clips. The reaction continued overnight to yield films ranging in composition from 0 to 15 wt % disulfide (see Figure B.4).

Table B.1: Films ranging in disulfide composition produced.

Disulfide [wt %]	Amount of Disulfide [g]	Observation
0	0	Purple, opaque, very hard film
2	0.04	Opaque, dark tan film, very rigid
5	0.1	Transparent, yellow film
8	0.15	Transparent, yellow film
10	0.2	Transparent, yellow film
15	0.3	Yellow, ridges in film, pockets of liquid

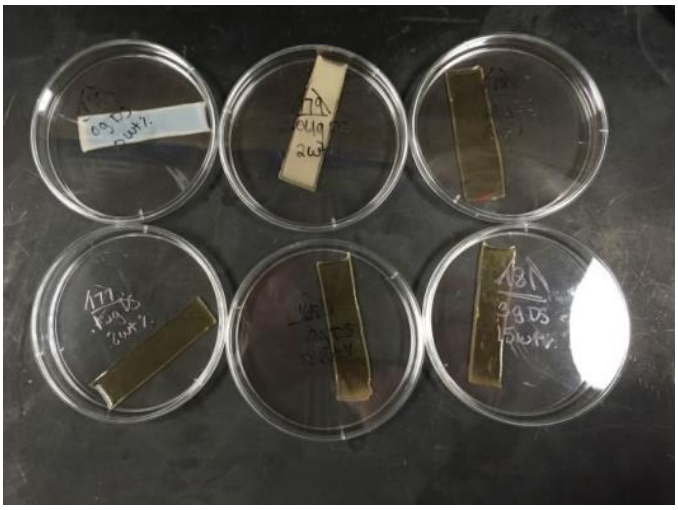

Figure B.4: Picture of the films ranging in composition from 0 to 15 wt % disulfide (top row, l-r: 0 wt%, 2 wt%, 5 wt%; bottom row, l-r: 8 wt%, 10 wt%, 15 wt%)

Fourier transform infrared spectroscopy (FTIR) was used to monitor the polymerization of a 5 wt% disulfide solution. A 5 wt% sample was prepared as described above and rapidly injected between two NaCl disks. The spectra before and after 450 minutes of polymerization are shown in Figure B.5 in addition to the

conversions calculated from peaks corresponding to alkene C-H and C=C stretches. The disappearance of these peaks in conjunction with the appearance of the peak at 967 cm^{-1} corresponding to C-H stretch on a disubstituted alkene indicate the opening of the ring and successful, yet incomplete polymerization. However, it was not clear from the spectra if the norbornene on the disulfide was polymerizing with the cyclooctene. To test this, the 0 wt% disulfide film was dissolved in toluene and heated until it dissolved completely indicating that it was not crosslinked. When subjected to the same conditions, the 5 wt% film did not dissolve suggesting that a crosslinked network was formed.

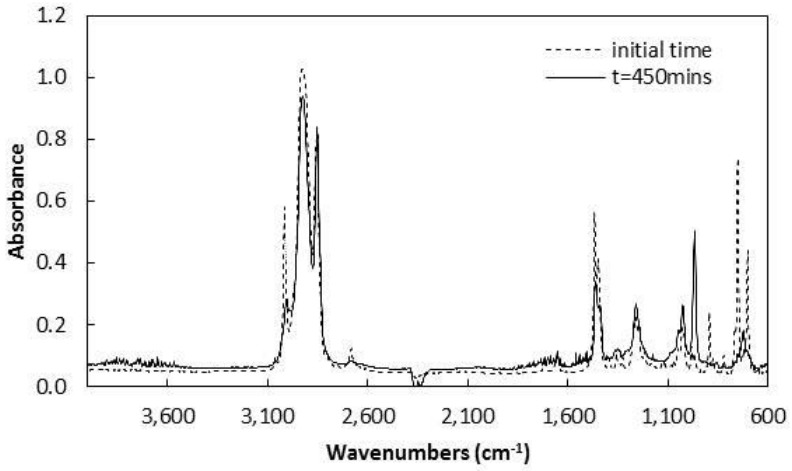

Figure B.5: FTIR spectra before and after (t=450 min) ROMP polymerization.

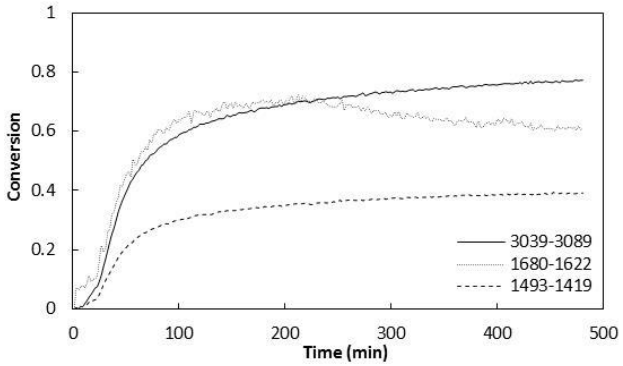

Figure B.6: Conversion plot calculated from peaks corresponding to alkene C-H and C=C stretches

B.5 Testing and Characterization

These materials were designed to heal under light. The films were sliced in half using a razor blade; the two halves were subsequently held together under 365 nm light (Exfo, Omnicure Series 2000 UV lamp). However, none of the films healed under UV light (see Table B.2).

Since the material did not heal, it was tested to determine if it could photopattern. A photomask with vertical lines was placed on top of the film and irradiated with 365 nm light. Results are shown in Table B.2. We hypothesized that the rearrangement of the photo-active disulfide caused the patterning.

Table B.2: None of the samples heal. The 5 wt% disulfide film photopatterns.

Disulfide [wt %]	Healing	Photopatterning
0	Did not heal	Did not photopattern
2	Did not heal	Did not photopattern
5	Did not heal	Photopatterns 
8	Did not heal	Slight pattern detected
10	Did not heal	Did not photopattern
15	Did not heal	Did not photopattern

Photo-induced stress relaxation experiments were conducted using a dynamic mechanical analyzer (TA Q800 DMA) and a UV lamp with a 365 nm filter. The material was strained to 5%, and stress was measured. Since the 5 wt% film photopatterned, it was selected for these experiments.

The stress-relaxation experiments revealed large changes in the material over time. For instance, when the material was strained at 5%, the initial stress measured was approximately an order of magnitude higher for a sample aged two weeks (Figure B.8) when compared to the initial properties of the same film (Figure B.7). Furthermore, the material became visibly cloudy and significantly stiffer over time. In the area where the sample was irradiated, it returned to its original, transparent state while the area under the clamps remained stiff and opaque. The material appeared to relax when irradiated in both cases, which we hypothesized was due to light-triggered disulfide rearrangement, yet the aging behavior described above was further investigated.

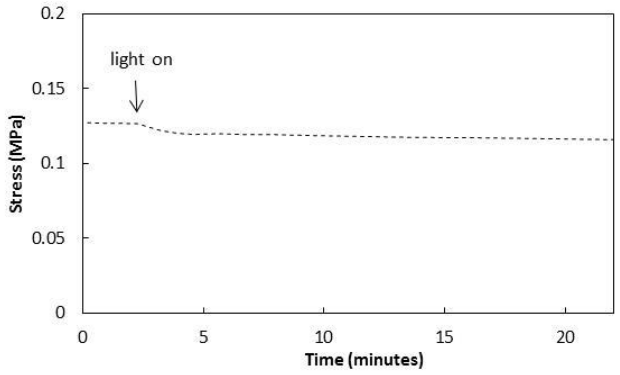

Figure B.7: Stress relaxation of a new sample and the same sample one week later (Figure B.8). The initial stress is approximately an order of magnitude higher in the older sample.

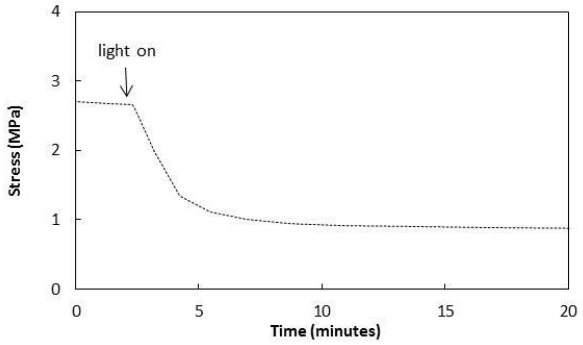

Figure B.8: Stress relaxation of the sample shown in Figure B.7 one week later. The initial stress is approximately an order of magnitude higher in the older sample.

The disulfide-containing cyclooctene films did not age consistently. For example, two separate samples were aged to one week and are shown in Figure B.9 and B.10. These are 5 wt% disulfide monomer samples, prepared identically and left in the same location for one week. However, the initial modulus of each sample differs by

more than an order of magnitude, which indicates that the aging process was not controlled or was extremely sensitive to environmental conditions.

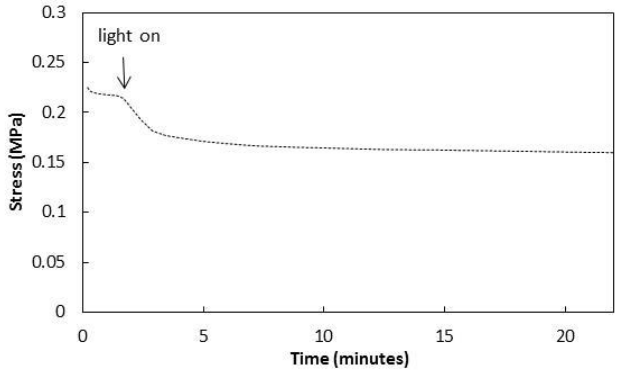

Figure B.9: Stress relaxation of a 5 wt% disulfide sample tested one week after polymerization. It was prepared identically and aged in the same location as the sample shown in Figure B.10. There is more than an order of magnitude difference between the two samples indicating that the aging process was not controlled.

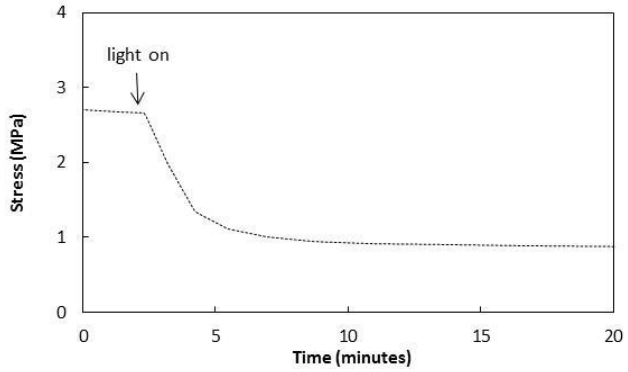

Figure B.10: Stress relaxation of a 5 wt% disulfide sample tested one week after polymerization. It was prepared identically and aged in the same location as the sample shown in Figure B.9. There is more than an order of magnitude difference between the two samples indicating that the aging process was not controlled.

To determine if the discrepancy arose due to inconsistencies while making or measuring the films, three different films were made independently from each other on the same day; two to three samples from each film were tested (Figure B.11). Within the same film, there was little to no variation between samples. Additionally, the three different films exhibited only slight variation between them, thus indicating that inconsistencies while making or measuring the films could not explain the large discrepancies between the films shown in Figure B.9 and Figure B.10. Therefore, it appears that the materials start with similar properties, which age differently over time.

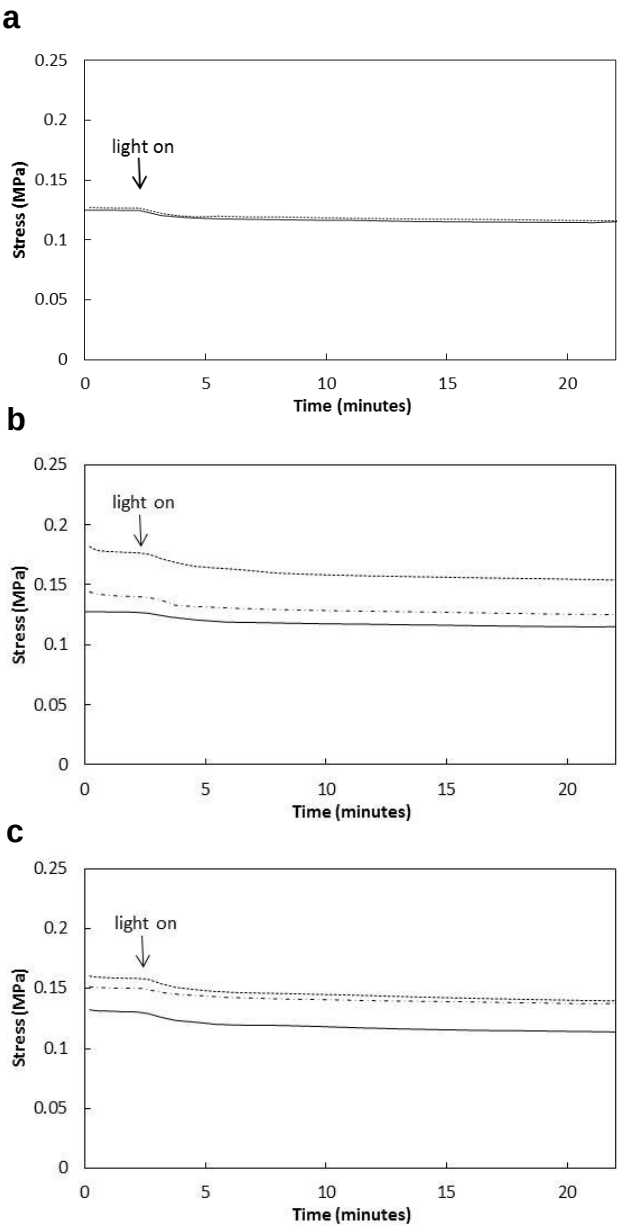

Figure B.11: Three different films (shown in a-c) were made independently from each other on the same day; 2 to 3 samples from each film were tested. Time axis was adjusted such that the light is turned on at the same time point.

The effect of temperature on the storage modulus and tan delta is shown in Figure B.12. At 50°C, the storage modulus becomes constant indicating no structure remains in the material. To eliminate the structure, an aged sample was heated in an oven overnight at 60°C. After heating, the aged material returned to its initial appearance; it became transparent and less stiff. The material was tested (Figure B.13) and is similar to the fresh sample shown in Figure B.7.

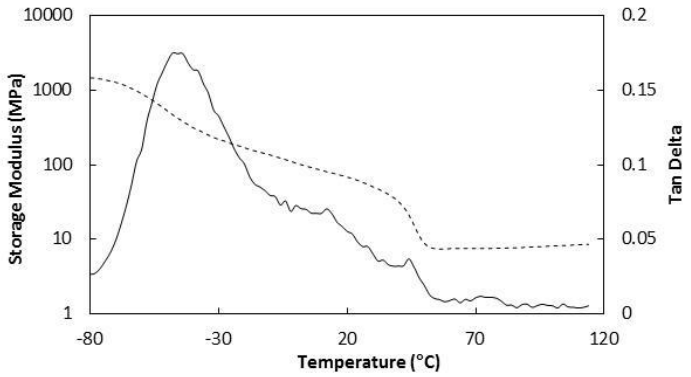

Figure B.12: Storage modulus (dashed line) and tan delta (solid line) as a function of temperature.

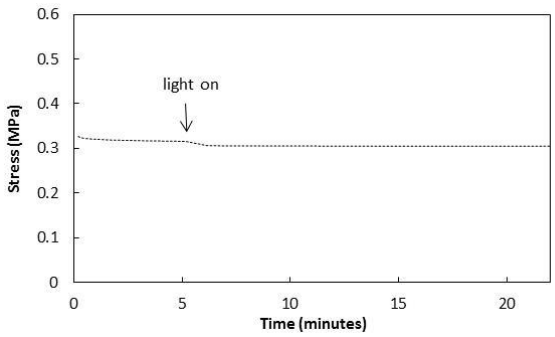

Figure B.13: Heated sample shows similar behavior to the fresh sample.

Based on these results, we hypothesized that the material was crystallizing. Diffraction patterns measured by wide angle x-ray scattering (Bruker D8 XRD) confirmed the presence of crystallinity in aged samples (Figure B.14). The five day old sample had sharp peaks, indicating that it had crystallized in contrast to the one day old film, which was amorphous.

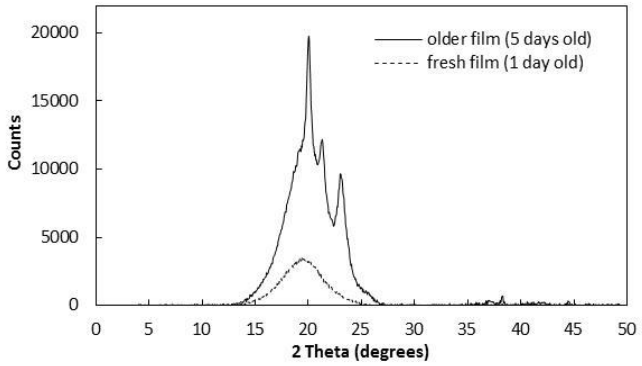

Figure B.14: Material crystallizes over time.

Since the material becomes crystalline, it is very likely that when the sample was irradiated, it transitioned from a crystalline to non-crystalline state, which resulted in the relaxation behavior measured above. This is consistent with the material becoming transparent in the irradiated areas and matching the behavior of samples that were heated in the oven. Further, under less intense light (30 mW/cm^2), no relaxation was observed suggesting that it was the heat from the lamp that was changing the material's properties rather than the light itself. Moreover, the same relaxation experiment was conducted using 470 nm light, which is not absorbed by the disulfide according to its UV-Vis spectrum. The same relaxation behavior occurred, further suggesting that the relaxation was temperature-driven as the material transitioned from a crystalline to non-crystalline state and that the disulfide played little to no role.

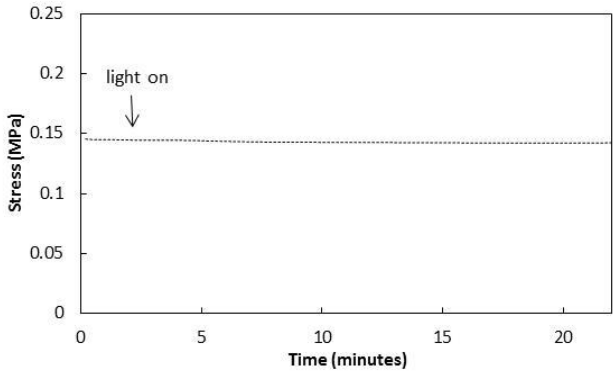

Figure B.15: No response under less intense light (30 mW/cm^2) is measured.

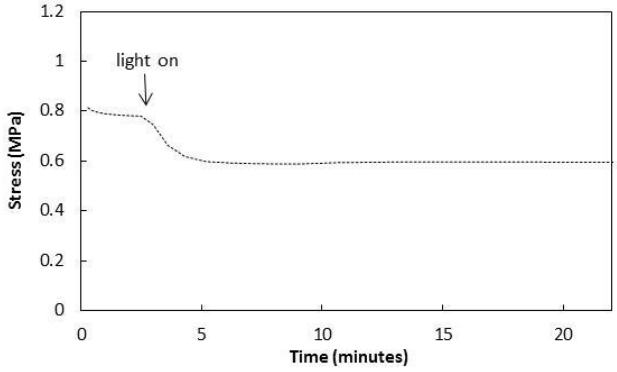

Figure B.16: Relaxation measured using 470 nm light, which is not absorbed by the disulfide.

To ensure no chemical changes were occurring during irradiation, FTIR spectra were obtained before and after 60 minutes of irradiation. No changes were observed, as shown in Figure B.17, which suggests that no reactions occurred during irradiation, although it is possible that the change is below the detection limit given the low concentration of disulfide in the films.

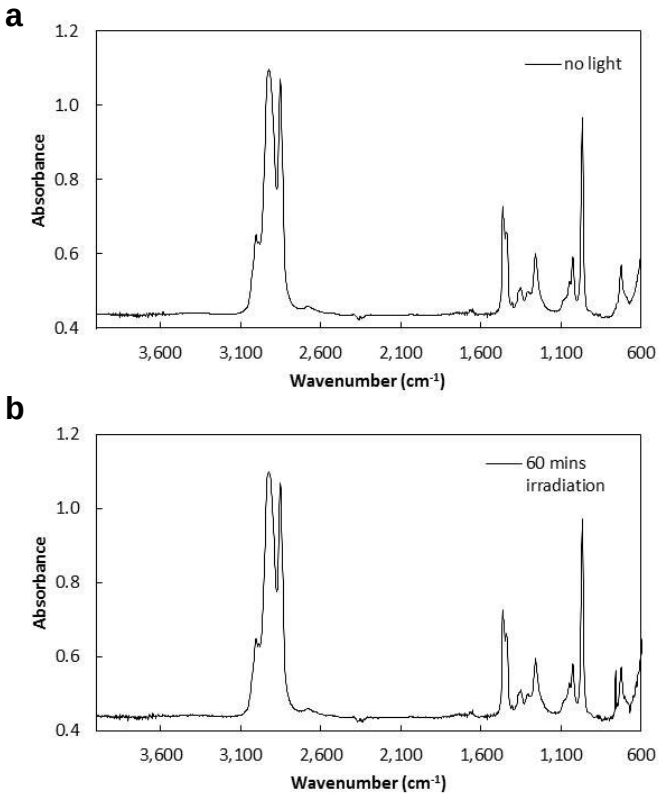

Figure B.17: FTIR spectra (a) before and (b) after 60 minutes of irradiation. No changes were observed.

B.6 Conclusions

In conclusion, the desired dixanthogen monomer with norbornene end groups was successfully synthesized and polymerized via ROMP, which is orthogonal to the radical-based rearrangements. The dixanthogen monomer was not completely polymerized as determined by FTIR and the material crystallized over time as measured by wide angle x-ray scattering. The resultant material did not heal when exposed to 365 nm UV light though the materials did exhibit stress relaxation and were capable of photopatterning. However, this behavior was likely temperature-driven as the material

transitioned from a crystalline to non-crystalline state since relaxation was observed using 470 nm light which is not absorbed by the disulfide according to its UV-Vis spectrum. Additionally, materials that were heated to a temperature sufficient to remove structure from the material prior to testing at room temperature did not significantly relax. Thus, the disulfide played little to no role in promoting healing, stress relaxation and photopatterning in the network.

From this work, it was apparent that a new network design was required. ROMP served as an orthogonal polymerization scheme, but the network polymerization did not go to full conversion, which led to undesired reactions as the unreacted norbornene and cyclooctene can interfere with the radical-based disulfide recombination. Additionally, the material crystallized over time. More importantly, incomplete polymerization was observed even after hours of irradiation, further reinforcing the need for an orthogonal polymerization strategy to the radical-based rearrangement. A new polymerization strategy was limited by the norbornene end group and this prompted the redesign of the monomer. The knowledge gained in this study was applied to the photoactive system described in Chapter 2, which differs from the disulfide monomer structure discussed here by the incorporation of a xylene group in the center of the molecule. Successful light-active, radical chemistry and mechanochemistry have been demonstrated in polyurethane networks [16, 131]. Based on these results, the best option moving forward was to redesign the mechano-monomer for incorporation into polyurethane networks, and the reactions used to make the monomer for the light-active system of Matyjaszewski were adapted to do so.

Attempt #1: Incomplete radical-based polymerization

One of the earliest systems tested involved synthesizing a new monomer that was capable of light-activated rearrangements when incorporated into a thiol-ene network. The synthesis steps are shown below and the synthetic procedure for the first step was adapted from reference [132].

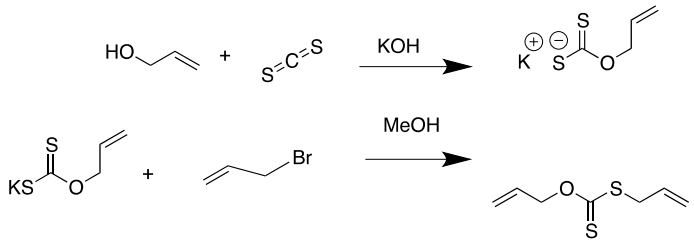

Figure B.18: Synthesis for light-active crosslinker in thiol-ene network

Synthesis procedure: Approximately 65 mL of allyl alcohol was mixed with 10.0 g of KOH. Following this, 13 mL (0.22 mol) of carbon disulfide was added slowly under argon and there was an instant change from green to yellow. The reaction proceeded for one hour until 60 mL of diethyl ether was added to reaction to precipitate the allyl alcohol anion. The product was washed in hexanes and isolated via filtration to yield a yellow solid (62% yield). Allyl bromide (1.5 mL, 0.178 mol) was mixed with 3.43 g (0.02 mol) of anion in 100 mL of methanol overnight. The methanol was then evaporated and the remainder was dissolved in chloroform and washed three times with water. The organic phased was dried with Na_2SO_4 and the solvent was evaporated to yield a yellow oil (20% yield). An allyl bromide impurity remained.

A control monomer with a similar molecular weight was developed for the system and the synthesis step is shown below:

Figure B.19: Synthesis of the control monomer

Synthesis procedure: Under argon, 5.8 mL of trimethylamine was dissolved in 70 mL of DCM. To this solution 3.5 mL of allyl bromide was added and mixed on ice. A solution containing 50 mL DCM and 1.8 mL ethanedithiol was added dropwise. The ice bath was removed when both solutions had mixed and the reaction proceeded for four hours. The product was washed with water three times and the DCM was evaporated. A white product remained; it was inconclusive if the desired product had formed and it was never separated from the remaining unreacted starting materials.

A radical thiol-ene polymerization was attempted with the synthesized monomer, TMPMP, a trithiol, and I-185, a photoinitiator. However, regardless of the light intensity, a network did not form. A network was formed when 50% of the synthesized monomer was replaced with tri(ethylene glycol) divinyl ether. The resultant network was sticky regardless of the irradiation time and dosage. Since the synthesized monomer was developed to enable rearrangement under light, the network was tested via photopatterning. The film successfully patterned when irradiated, although this may be due to a combination of continued polymerization and rearrangement. Likely, the films never fully polymerized; the film was simultaneously reorganizing and polymerizing throughout testing. This result underscored the need for a polymerization strategy that is chemically orthogonal to the rearrangement reaction.

Attempt #2-#4: Unsuccessful attachment of carbon disulfide

After Attempt #1, it was apparent that an orthogonal polymerization scheme was necessary and a norbornene ring was chosen for ROMP. The successful addition of carbon disulfide to a starting material with a norbornene ring was a major challenge. Furthermore, detection of this attachment was an additional challenge. Figure B.20 summarizes the starting materials to which carbon disulfide addition was attempted.

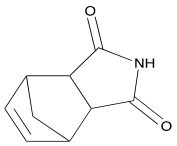

5-norbornene-2,3-dicarboximide

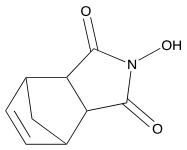

N-hydroxy-5-norbornene-2,3-dicarboximide

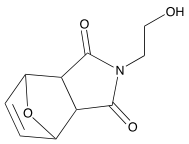

Hydroxyethyl-tetrahydro-expoxyisoindoledione

Figure B.20: Starting materials to which carbon disulfide addition was attempted.

Combination tables testing different starting materials, solvents and bases at varied temperature and times over a range of concentrations were developed. Examples are shown in Table B.3 and B.4. Ultimately, various experimental conditions were tested by modifying the solvent (e.g., DMSO, DMF, ethanol, CS_2), base (e.g., NaOH, KOH, NaH) and time, but formation of the desired product was unfavorable under the conditions we tested as determined by ^{1}H NMR. Typical results included only starting materials present at the conclusion of the reaction. Using the third starting material shown in Figure B.20, carbon disulfide successfully attached, but yields were less than 2%. However, ^{1}H NMR is not ideal for determining CS_2 incorporation and future studies with norbornene alcohol as the starting material used ^{13}C NMR and mass

spectrometry. A secondary reaction involving dibromoxylene addition was also tested by varying concentrations of dibromoxylene for a related project.

Table B.3: Example synthesis table testing different solvents

Starting Material	**CS_2**	**NaH**	**Solvent**	**Temperature**	**Time**
1 eqv.	2 eqv.	2 eqv.	DMSO	0°C	4 hr
1 eqv.	2 eqv.	2 eqv.	DMF	0°C	4 hr
1 eqv.	2 eqv.	2 eqv.	Ethanol	0°C	4 hr
1 eqv.	--	2 eqv.	CS_2	0°C	4 hr

Table B.4: Example synthesis table testing different reaction times

Starting Material	**CS_2**	**NaH**	**Solvent**	**Temperature**	**Time**
1 eqv.	2 eqv.	2 eqv.	Anhydrous THF	0°C	1 hr
1 eqv.	2 eqv.	2 eqv.	Anhydrous THF	0°C	2 hr
1 eqv.	2 eqv.	2 eqv.	Anhydrous THF	0°C	6 hr
1 eqv.	2 eqv.	2 eqv.	Anhydrous THF	0°C	overnight

Attempt #5-#7: Formation of disulfide bond

Disulfide formation was not successful using the reactions shown below. In all reactions, water was used as the solvent since it readily dissolved the anion and, ideally, the disulfide would precipitate out of solution. In the first reaction scheme, oxygen was bubbled through the sample for several days to promote disulfide formation, however no reaction took place. The anion was then acidified and the same reaction was re-attempted, yet disulfide formation was not favored. In the third reaction scheme shown, an excess of iodine was reacted with the anion; unfortunately the iodine reacted with the norbornene group instead and again no disulfide was formed.

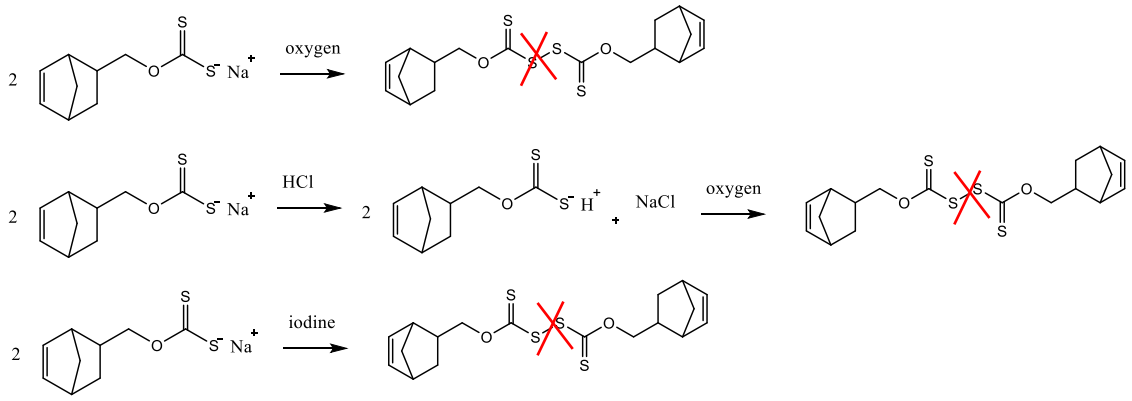

Figure B.21: Disulfide bond not formed using these schemes.

Attempt #8: Non-ideal film for testing

A solution of 10 wt% monomer (25% disulfide, 75% 2-norbornene) in DCM was polymerized in a scintillation vial to form a gel which could provide enough mobility to allow for rearrangement and healing. Specifically, a stock solution of 0.03 g of Grubbs catalyst was added to 5 mL anhydrous DCM. A solution consisting of 0.14 g of 2-norbornene in 0.5 mL anhydrous DCM was mixed with a solution consisting 0.2 g of the disulfide monomer in 0.5 mL anhydrous DCM. Argon was bubbled through the catalyst stock solution and the monomer solution prior to injecting 1.2 mL of the stock solution into the monomer solution. The solution was vigorously mixed in a scintillation vial for several minutes, the stir bar was removed and the solution was left to polymerize. The resultant gel was dark yellow and after washing it in DCM, became lighter yellow yet remained sticky. The gel was sliced in half, then joined together and held under 365 nm light. After a few minutes, the sample adhered to itself and could be held from one end without falling apart. As a control, no light was used and the material could not be held from one end without falling apart despite being sticky. However, the sample could not heal in the same place twice, indicating that the sulfur radical may be attacking unreacted norbornene rather than recombining with itself. To ensure that the catalyst was not continuing to react, the same procedure was followed but the gel was swelled in ethyl vinyl ether to inactivate the catalyst. The gel was sliced, held together under 365 nm light and healed.

The next challenge was casting the material into a film so it could be tested via DMA. The same solution was formed and instead of polymerizing in a scintillation vial, it was cast between two glass slides separated by a spacer. The DCM evaporated significantly during the polymerization, causing the film to form bubbles and significantly shrink. To prevent evaporation, the film was polymerized in DCM

chamber filled with DCM and towels soaked in DCM. This prevented some of the evaporation, but DCM was replaced with DMF since it would evaporate less. Unfortunately, the DMF caused phase separation during polymerization. DMF was replaced by toluene as the solvent; for this procedure, 0.005 g Grubbs catalyst was dissolved in 5 mL of toluene. A solution of 0.14 g of 2-norbornene in 0.5 mL anhydrous toluene and a solution of 0.2 g of the disulfide monomer in 0.5 mL anhydrous toluene was mixed together yielding transparent, clear films. Evaporation was significantly decreased compared to earlier formulations and no bubbles were formed. However, these gels did not heal and shriveled over time. The material did photopattern, yet significant evaporation occurred during the patterning under the heat of the lamp, which caused changes in the material's shape. Additionally, the material was very slippery and therefore could not be adequately stretched and held in place due to the high concentration of solvent. During stress relaxation experiments conducted using DMA, the material continually evaporated and never reached constant value. For these reasons, the solvent and 2-norbornene were replaced with cyclooctene.

Appendix C

COLLOIDAL GEL AGING DATA

This appendix provides the raw data set for the AHS thermoreversible gel (ϕ=0.28) shown in Figure 4.1. The temporal evolution of G′ and G″ are shown for a sample quenched from the liquid state at 40°C to the gel state at 28.6°C. The small amplitude oscillatory shear experiment (1 rad/s, 0.1% strain) was collected on the DHR rheometer. The data set can be obtained by following the link below:

https://drive.google.com/open?id=0B4FEvwFQZuzWUE9JSGFwbzlYQWs

Appendix D

MICROSTRUCTURAL BASIS OF AGING IN WEAK (ϕ=0.12) THERMOREVERSIBLE COLLOIDAL GELS

D.1 Introduction

This work investigates aging behavior in a low concentration (ϕ=0.12) thermoreversible colloidal gel.

D.2 Experimental Methods

Particle Synthesis and Gel Formation: Silica nanoparticles were functionalized with an octadecyl brush by following an established procedure [28, 39]. Specifically, 30 nm silica nanoparticles (Ludox TM-50, Sigma Aldrich) and reacted with 1-octadecanol (Alfa Aesar), as discussed in Chapters 4 and 5. The particles were purified by washing three times in a 60:40 cyclohexane/chloroform mixture in a Sorvall RC 6 Plus centrifuge. Solvent was removed from the particles by placing them under a nitrogen stream and then in a vacuum oven overnight. The particles were dispersed in tetradecane to form a 0.12 volume fraction colloidal gel.

Rheo-SANS Measurements: Concurrent rheological and small angle neutron scattering (Rheo-SANS) measurements were performed at the National Institute of Standards and Technology (NIST) Center for Neutron Research (NCNR) in Gaithersburg, MD. An Anton Paar MCR-501 stress-controlled rheometer was placed into the NGB30 beamline. The AHS sample was placed within titanium concentric cylinder geometry with an inner bob diameter of 28 mm and a 0.5 mm gap. Time-resolved SANS

experiments were conducted in the 1,3 plane at a detector distance of 13 m with a lens. The same sample was used for all tests; between tests the sample was fully rejuvenated by thermal cycling. The pre-shear protocol consisted of (1) shearing the sample in its liquid state at 10 s^{-1} for 10 minutes at 40°C and (2) holding the sample quiescently at 40°C for 2 minutes. Aging experiments were conducted at 28.4°C at 0.1% strain and a frequency of 1 Hz. SANS data was reduced using the SANS Data Reduction Macros in Igor Pro available from NIST [92]. Time-resolved scattering results were binned using event mode processing in Igor Pro. 1-D scattering patterns were fit to the sticky hard sphere (SHS) model to extract the Baxter parameter (τ) in SAS View. Fitting parameters are described elsewhere [39, 75]. The same scattering length density (SLD) of the shell reported in Chapter 4 was used (SLD shell = -3.9e-07 $Å^{-2}$) to data. The perturbation parameter was fixed as $\varepsilon = 0.01$ for all cases.

D.3 Results and Discussion

A frequency sweep at 28.4°C was conducted to determine that a soft gel capable of flowing homogeneously formed. The sweep shown in Figure D.1 was conducted at 0.1% strain at 28.4°C in the Couette geometry on the Anton Paar MCR-501 rheometer. The system was equilibrated at this temperature for 45 minutes before initiating the frequency sweep. All aging experiments were subsequently conducted at this temperature.

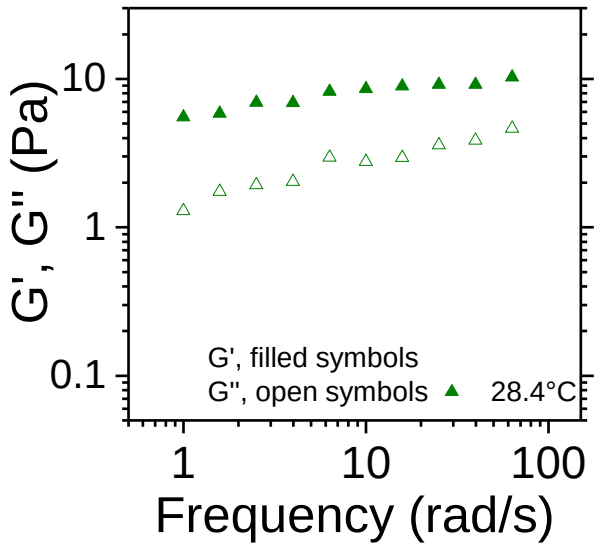

Figure D.1: Frequency sweep at 28.4°C. The sample forms a soft gel at this temperature.

Rheological aging of the colloidal gel at 28.4°C is shown in Figure D.2. Gel formation was induced by two distinct thermal pathways: (1) the cooling direction in which the sample was quenched from its liquid state at 40°C to 28.4°C and (2) the heating direction in which the sample was quenched from 40°C to 25°C and then to 28.4°C. Note that the gas-cooled Rheo-SANS Couette sample environment displayed imperfect temperature control, which caused overshoots in temperature during the quench. The temperature was steady during the aging shown in the figure. As expected, the ϕ=0.12 evolved to lower final storage modulus after the two hour aging experiment when compared with the ϕ=0.28 colloidal gel and the ϕ=0.46 colloidal glass.

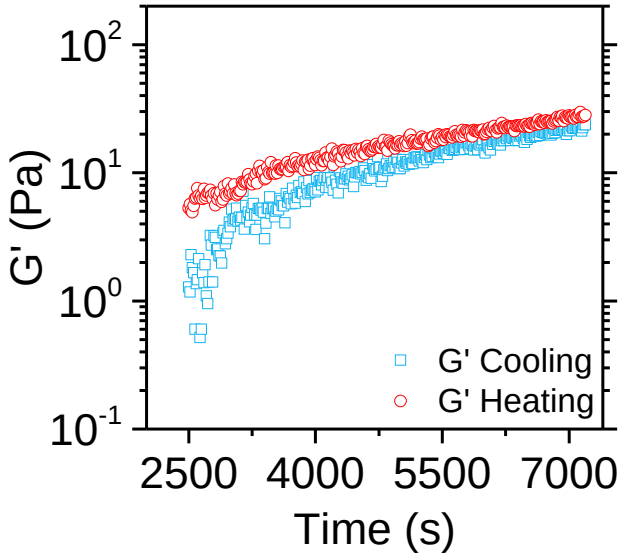

Figure D.2: Evolution of the storage moduli (G′) when the gel was quenched from the heating and cooling direction.

Time-resolved SANS experiments were conducted simultaneously with the aging experiment described above and the time-resolved data are shown in Figure D.3 and Figure D.4 for the cooling and heating profile, respectively. Specifically, two thermal profiles were investigated: (1) quenching from 40°C to 28.4°C (the cooling direction) or (2) quenching from 40°C to 25°C to 28.4°C (the heating direction). Samples were fully rejuvenated between aging experiments following the pre-shear protocol described in the methods section. The time-resolved measurements were divided into 20 bins, each 6 minutes in duration. The evolution in microstructure for samples formed from the heating direction are consistent with a more deeply quenched gel, in which the gel samples a reduced number of energy states as it evolves toward equilibrium compared to gels formed from the cooling direction. Gels quenched from the cooling direction show greater changes in microstructure during aging, which is

consistent with particles sampling lower energy states via thermal motion. These results are qualitatively similar to the structural evolution observed for AHS colloidal gels [75] and colloidal glasses in Chapter 4 and Chapter 5, respectively, where the thermal profile during gel and glass formation was also investigated. As expected, the nearest neighbor peak at $q \approx 0.02$ Å^{-1} for gels and glasses discussed earlier, which corresponds to a length scale of approximately 30 nm (diameter of the AHS), is not observed in the scattering data for the $\phi=0.12$ gel. Furthermore, due to its enhanced mobility, the $\phi=0.12$ gel exhibits greater changes during its structural evolution compared to the more concentrated suspensions over the two hour aging experiment. Overall, the microstructural measurements are consistent with the free energy landscape viewpoint of gel aging, where the gel ages by sampling lower energy states as it evolves toward the global minimum, or the equilibrium state.

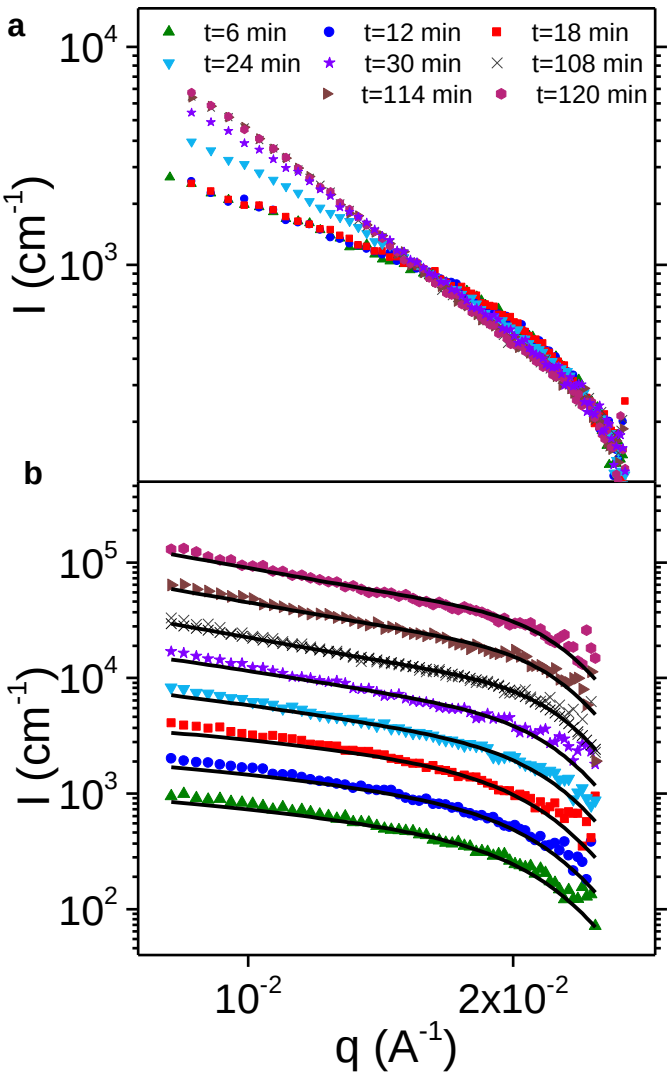

Figure D.3: **A.** Time-resolved small angle neutron scattering (SANS) data during a two-hour aging experiment. The gel was quenched from the cooling direction. **B.** The data was fit to the sticky hard sphere model for the cooling direction. All fitting parameters are fully described in the gel aging chapter. The intensity was doubled from the previous data set to clearly show the fits.

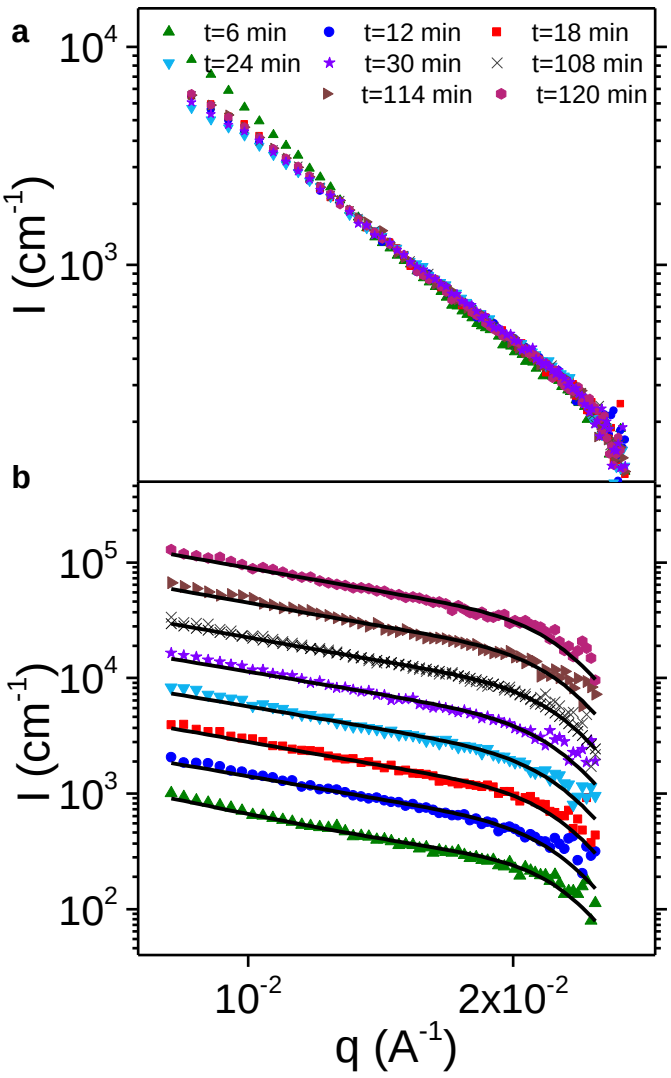

Figure D.4: **A.** Time-resolved small angle neutron scattering (SANS) data during a two-hour aging experiment. The gel was quenched from the heating direction. **B.** The data was fit to the sticky hard sphere model for the cooling direction. All fitting parameters are fully described in the gel aging chapter. The intensity was doubled from the previous data set to clearly show the fits.

To develop a relationship between the macroscopic bulk property changes and the evolving microstructure, the structural parameter λ was used to quantify the evolving microstructure, in accordance with the methods described in Chapter 4 and Chapter 5. In brief, the time-resolved microstructural data was first fit to the sticky hard sphere (SHS) model, which mathematically describes an attractive hard sphere system. In this representation, a single parameter, τ_β, known as the Baxter or "stickiness" parameter, characterizes the adhesive strength of the system. Thus, by fitting the SHS model to the microstructural measurements, the Baxter parameter at each time point was obtained, which tracked the structural evolution during colloidal gel aging. Following similar analysis to the gel aging and glass aging described earlier, we calculated a structural parameter λ as follows to quantify structural changes toward equilibrium:

$$\lambda = \frac{\tau_{40}^{eq} - \tau^{eff}}{\tau_{40}^{eq} - \tau_\infty} \tag{D.1}$$

where τ_{40}^{eq} is the value of the Baxter parameter in the liquid state at 40°C, τ^{eff} is the value of Baxter fit parameter during each time interval and τ_∞ is the equilibrium Baxter parameter. By fitting the SHS model to time-resolved SANS data, τ_{40}^{eq} = 0.270 and $\tau_\infty \approx 0.131$.

As shown in Figure D.5 A and B, there is a monotonic increase in both G′ and λ as the sample evolves towards its equilibrium state. The noise in the data is due to noise from SANS measurements and/or nonlinear model fitting. The bulk properties (G′) are plotted as a function of λ in Figure D.5 C, which shows a one-to-one relationship between storage modulus and microstructure that evolves in time as the sample ages. This result is consistent with the aging behavior observed for the colloidal gels and glass

studied earlier. The following equation was used to capture the relationship between log G′ and λ for times ≥ 18 minutes as the glass ages:

$$\log G' = 9.49\,\lambda - 8.14 \tag{D.2}$$

where $0.92<\lambda\leq 1.0$. This equation enables a quantitative, empirical relationship between colloidal glass microstructure and rheological properties during aging, which is independent of thermal history. This one-to-one correspondence between the evolution of G′ and λ is consistent with the free energy landscape viewpoint of aging, in which the gel evolves toward equilibrium by gradually sampling progressively lower energy states.

To elucidate the mechanistic origin of the aging process in the weak gel, we calculate a localization length based on predictions from mode coupling theory (MCT). As described in previous chapters, the localization length is the mean squared displacement of particle motion when trapped within a cage of nearest neighbors. The prediction from MCT is shown below:

$$\frac{G'a^3}{k_BT} = 0.29\frac{\phi a^2}{r_{loc}^2} \tag{D.3}$$

where a is the particle radius and r_{loc} is the localization. Using the final G′ value measured after two hours of aging during the small amplitude oscillatory shear measurement, a localization length of 20.4 nm was calculated. This result is indicative of cluster formation, which suggests that the diffusive motion of these clusters gives rise to the aging behavior. This differs from the calculation for the concentrated gel and glass sample studied earlier, where the localization length was on the order of the brush size, suggesting local particle motion as the mechanism of aging. The scattering data and localization length for the ϕ=0.12 sample do not suggest phase separation; for such phase-separating systems, a localization length corresponding to 3-4 particle diameters

was reported [103]. Instead, these results suggest local, cluster rearrangement the mechanism of aging in the homogeneous gel.

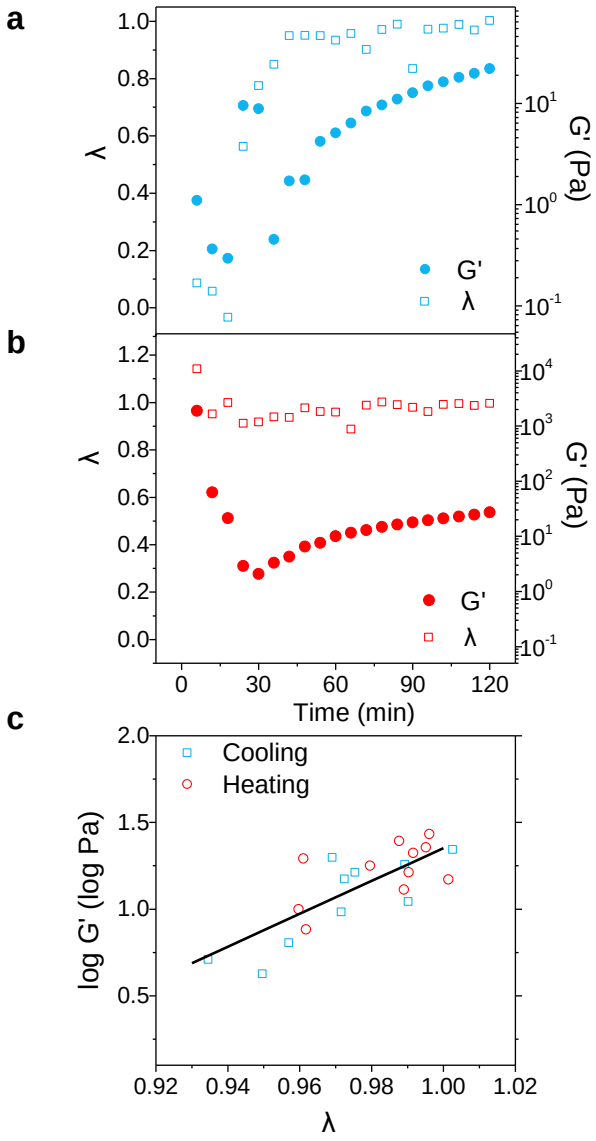

Figure D.5: Time-resolved Rheo-SANS and rheological measurements are shown. The evolution of G′ and λ as a function of time are shown from the **(A)** cooling direction and **(B)** heating direction. **(C)** The storage modulus is plotted as a function of the structural parameter, λ for times ≥ 18 minutes to develop the quantitative relationship: $\log G' = 9.49\,\lambda - 8.14$ where $0.92<\lambda\leq 1.0$.

Next, shear was applied to the aged sample to evaluate how processing conditions alter the aging process. To conduct these experiments, gels were formed from the cooling profile and aged to a reference state of 4250 s, which was selected for consistency to prior work [75]. The sample was subsequently tested at shear rates of 100 s^{-1} and 1000 s^{-1} for 20 minutes. The microstructure and corresponding viscosity during the application of shear are shown in Figure D.6A and Figure D.6B, respectively. Similar to the previous analysis described above, the microstructural measurements were fit to the SHS model, from which λ values were calculated. Structural parameters of 0.971 and 0.950 were calculated for shear rates of 100 s^{-1} and 1000 s^{-1}, respectively. While a shear rate of 1000 s^{-1} was applied to the sample, we observed a decrease in the fitted λ value, which indicates shear-induced destruction of the microstructure, consistent with the results presented in Chapter 5 and the work of Eberle and co-workers [104]. Similarly, overaging of the gel when subjected to the lowest shear rate tested (100 s^{-1}) was not observed, which is consistent with the results obtained for the colloidal glasses.

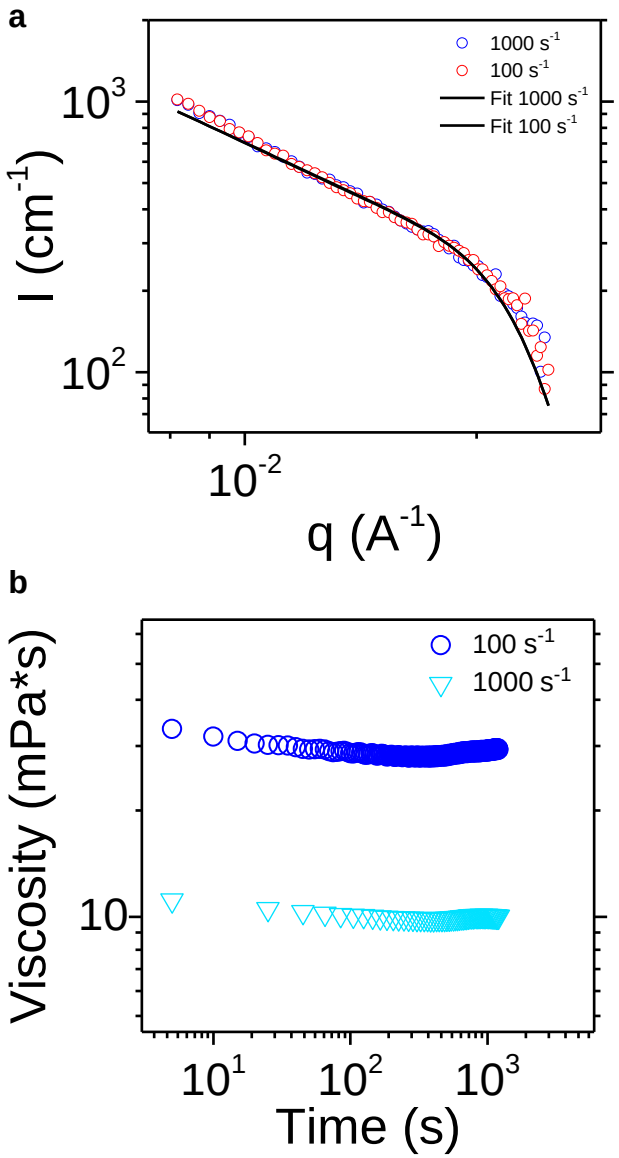

Figure D.6: **A.** Microstructural measurements of 0.12 volume fraction colloidal gel under shear rates of 100 s^{-1} and 1000 s^{-1} for 20 minutes are shown. The corresponding λ values are: $\lambda_{100s^{-1}}$=0.971 and $\lambda_{1000s^{-1}}$=0.950. **B.** The corresponding viscosity measurements during shear are also displayed.

The aging process following the application of shear was monitored to assess the effect of stress on the aging trajectory. Specifically, the continued aging of the specimen was monitored using small amplitude oscillatory shear measurements. The evolution of the microstructure is displayed in Figure D.7A after shearing at 1000 s^{-1}. An initial, intermediate and final structure is shown and the corresponding λ values increase from 0.978 to 0.994 by the conclusion of the 4250 s aging experiment. The increasing λ values signify the rebuilding of structure as the sample ages. Figure D.7B displays the corresponding mechanical property changes following shearing at the specified rate. As shown in the figure, the mechanical properties decrease by almost two orders of magnitude following shear and the sample subsequently ages following a similar trajectory as the unstressed sample by the conclusion of the 4250 s experiment. These rheological results indicate rejuvenation of the mechanical properties at shear rates of 100 s^{-1} and 1000 s^{-1}.

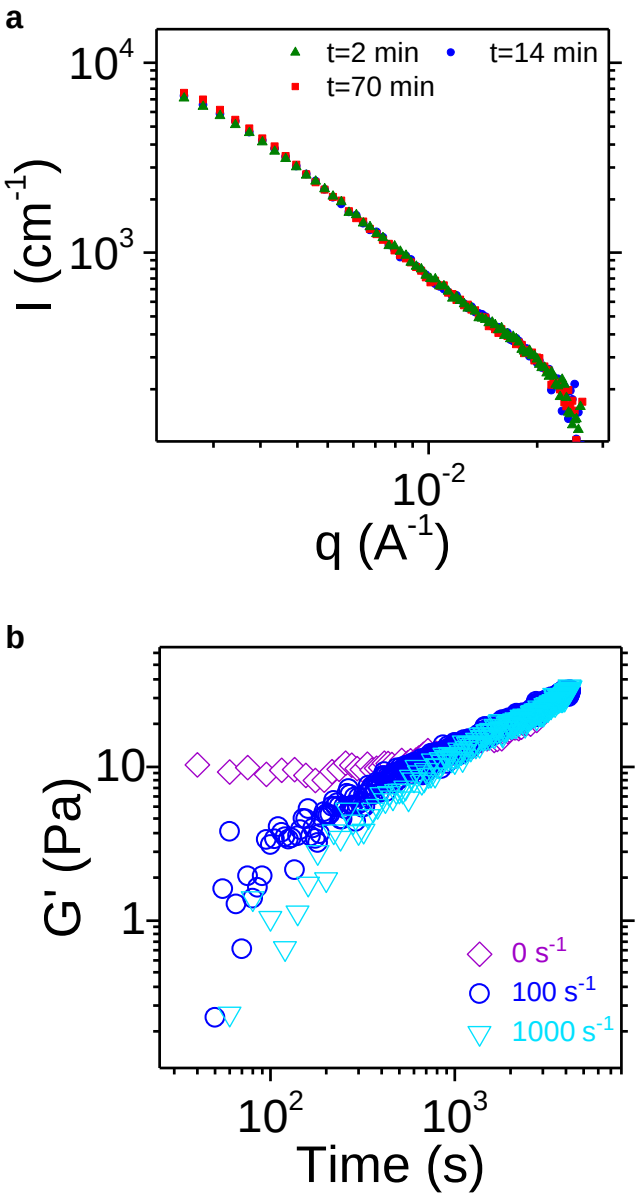

Figure D.7: **A.** Microstructural measurements of 0.12 volume fraction colloidal gel under SAOS following shearing at 1000 s^{-1}. **B.** Evolution of mechanical properties under SAOS after shearing for 20 minutes at the specified shear rate.

The experiment described above was further analyzed to evaluate the use of mechanical rejuvenation to restore the original microstructure and bulk properties in colloidal glasses. As the AHS system can be fully rejuvenated by thermal cycling, the bulk properties and microstructure following thermal and mechanical rejuvenation protocols were directly compared. Figure D.8 A and B compare the effects of thermal rejuvenation and mechanical rejuvenation on the evolution of mechanical properties and microstructure, respectively. Thermal rejuvenation consisted of shearing the sample at 10 s^{-1} in its liquid state at 40°C for 10 minutes followed by holding the sample quiescently at 40°C for 2 minutes. Mechanical rejuvenation consisted of shearing the sample at isothermally (at 28.4°C) at 1000 s^{-1} for 20 minutes. Following the cessation of shear, an immediate rise in the mechanical properties was observed, compared to the sample that was thermally rejuvenated. The evolution of mechanical properties progressed more rapidly following mechanical rejuvenation compared to the thermal rejuvenation. This indicates that either the gel structure was not completely erased by shear or that the microstructure continues to evolve under shear. Figure D.8 B shows that higher λ values immediately following shear were measured. However, despite differences in the trajectory during formation and early aging, the samples appear to tend toward a similar equilibrium state regardless of shear history. This behavior is qualitatively similar to behavior observed earlier for the ϕ=0.28 colloidal gel and ϕ=0.46 colloidal glass. Figure D.9 displays the relationship between G' and λ following thermal cycling and shearing 1000 s^{-1}. Notably, the same relationship between G' and λ that was developed for gel aging following a thermal quench (equation D.2, shown as a black line in Figure D.9) applies to gel aging following shear at 1000 s^{-1}, indicating that there is a one-to-one correspondence between the mechanical properties and underlying

microstructure under these experimental conditions. We note that at short times immediately following shear (corresponding to low λ values in the figure), the data deviates from the relationship, which indicates that immediately following shear, λ may not fully characterize the microstructure.

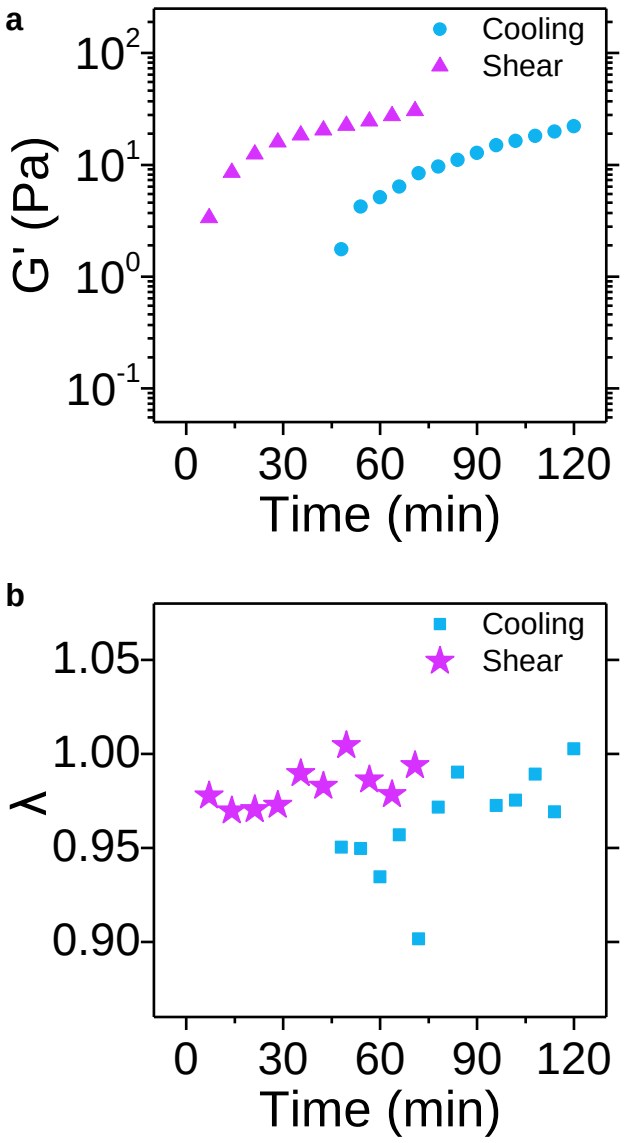

Figure D.8: The effects of thermal and mechanical rejuvenation on gel mechanical properties (G′) and microstructure (λ) are shown. Thermal rejuvenation consisted of shearing the sample at 10 s^{-1} in its liquid state at 40°C for 10 minutes followed by holding the sample quiescently at 40°C for 2 minutes. Mechanical rejuvenation consisted of shearing the sample at isothermally (at 28.4°C) at 1000 s^{-1} for 20 minutes. **A.** Evolution of storage modulus following thermal cycling and shear. **B.** Evolution of microstructure following thermal cycling and shear.

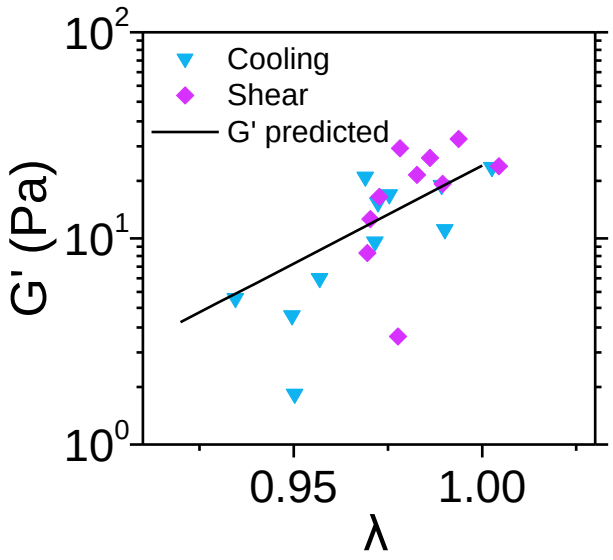

Figure D.9: The storage modulus is plotted as a function of its microstructure, which is described by the structural parameter λ, to directly relate the bulk properties to the underlying microstructure following shear. The same relationship between G' and λ that was developed for gel aging following a thermal quench (eqn D.3, black line) applies to gel aging following shearing the sample at 1000 s^{-1}, indicating that there is a one-to-one correspondence between the mechanical properties and underlying microstructure under these experimental conditions.

D.4 Summary and Conclusions

In conclusion, the weak themoreversible (ϕ=0.12) gel examined here demonstrates rheological and structural aging, which were related by an empirical relationship, analogously to the gel and glasses studied earlier in the dissertation. Interestingly, the localization length calculated for this gel was consistent with cluster formation, suggesting that the local motion of clusters underlies the macroscopic aging behavior. This result indicates a distinct mechanistic origin for the aging behavior in

comparison to the more concentrated gel and glass sample studied earlier, where the calculated localization length suggested local particle motion as the mechanism of aging. Similar to the behavior associated with the more concentrated samples, however, the microstructure was not completely erased by shear rejuvenation despite apparent rheological rejuvenation. Moreover, the aging behavior observed for this sample was consistent with the free energy viewpoint of colloidal gel aging.

Appendix E

PERMISSIONS

JOHN WILEY AND SONS LICENSE TERMS AND CONDITIONS

Nov 19, 2016

This Agreement between Melissa B Gordon ("You") and John Wiley and Sons ("John Wiley and Sons") consists of your license details and the terms and conditions provided by John Wiley and Sons and Copyright Clearance Center.

License Number	3992650105904
License date	Nov 19, 2016
Licensed Content Publisher	John Wiley and Sons
Licensed Content Publication	Advanced Materials
Licensed Content Title	Dynamic Bonds in Covalently Crosslinked Polymer Networks for Photoactivated Strengthening and Healing
Licensed Content Author	Melissa B. Gordon,Jonathan M. French,Norman J. Wagner,Christopher J. Kloxin
Licensed Content Date	Nov 2, 2015
Licensed Content Pages	4
Type of use	Dissertation/Thesis
Requestor type	Author of this Wiley article
Format	Print and electronic
Portion	Full article
Will you be translating?	No

Title of your thesis / dissertation	The Development and Characterization of Stimuli-Responsive Systems for Performance Materials
Expected completion date	Dec 2016
Expected size (number of pages)	200
Requestor Location	Melissa B Gordon 150 Academy Street NEWARK, DE 19716 United States Attn: Melissa B Gordon
Publisher Tax ID	EU826007151
Billing Type	Invoice
Billing Address	Melissa B Gordon 150 Academy Street NEWARK, DE 19716 United States Attn: Melissa B Gordon
Total	0.00 USD

Terms and Conditions

TERMS AND CONDITIONS

This copyrighted material is owned by or exclusively licensed to John Wiley & Sons, Inc. or one of its group companies (each a"Wiley Company") or handled on behalf of a society with which a Wiley Company has exclusive publishing rights in relation to a particular work (collectively "WILEY"). By clicking "accept" in connection with completing this licensing transaction, you agree that the following terms and conditions apply to this transaction (along with the billing and payment terms and conditions established by the Copyright Clearance Center Inc., ("CCC's Billing and Payment terms and conditions"), at the time that you opened your RightsLink account (these are available at any time at http://myaccount.copyright.com).

Terms and Conditions

- The materials you have requested permission to reproduce or reuse (the "Wiley Materials") are protected by copyright.

- You are hereby granted a personal, non-exclusive, non-sub licensable (on a stand-alone basis), non-transferable, worldwide, limited license to reproduce the Wiley Materials for the purpose specified in the licensing process. This license, **and any CONTENT (PDF or image file) purchased as part of your order,** is for a one-time use only and limited to any maximum distribution number specified in the license. The first instance of republication or reuse granted by this license must be completed within two years of the date of the grant of this license (although copies prepared before the end date may be distributed thereafter). The Wiley Materials shall not be used in any other manner or for any other purpose, beyond what is granted in the license. Permission is granted subject to an appropriate acknowledgement given to the author, title of the material/book/journal and the publisher. You shall also duplicate the copyright notice that appears in the Wiley publication in your use of the Wiley Material. Permission is also granted on the understanding that nowhere in the text is a previously published source acknowledged for all or part of this Wiley Material. Any third party content is expressly excluded from this permission.

- With respect to the Wiley Materials, all rights are reserved. Except as expressly granted by the terms of the license, no part of the Wiley Materials may be copied, modified, adapted (except for minor reformatting required by the new Publication), translated, reproduced, transferred or distributed, in any form or by any means, and no derivative works may be made based on the Wiley Materials without the prior permission of the respective copyright owner.**For STM Signatory Publishers clearing permission under the terms of the STM Permissions Guidelines only, the terms of the**

license are extended to include subsequent editions and for editions in other languages, provided such editions are for the work as a whole in situ and does not involve the separate exploitation of the permitted figures or extracts,You may not alter, remove or suppress in any manner any copyright, trademark or other notices displayed by the Wiley Materials. You may not license, rent, sell, loan, lease, pledge, offer as security, transfer or assign the Wiley Materials on a stand-alone basis, or any of the rights granted to you hereunder to any other person.

- The Wiley Materials and all of the intellectual property rights therein shall at all times remain the exclusive property of John Wiley & Sons Inc, the Wiley Companies, or their respective licensors, and your interest therein is only that of having possession of and the right to reproduce the Wiley Materials pursuant to Section 2 herein during the continuance of this Agreement. You agree that you own no right, title or interest in or to the Wiley Materials or any of the intellectual property rights therein. You shall have no rights hereunder other than the license as provided for above in Section 2. No right, license or interest to any trademark, trade name, service mark or other branding ("Marks") of WILEY or its licensors is granted hereunder, and you agree that you shall not assert any such right, license or interest with respect thereto

- NEITHER WILEY NOR ITS LICENSORS MAKES ANY WARRANTY OR REPRESENTATION OF ANY KIND TO YOU OR ANY THIRD PARTY, EXPRESS, IMPLIED OR STATUTORY, WITH RESPECT TO THE MATERIALS OR THE ACCURACY OF ANY INFORMATION CONTAINED IN THE MATERIALS, INCLUDING, WITHOUT LIMITATION, ANY IMPLIED WARRANTY OF MERCHANTABILITY, ACCURACY, SATISFACTORY QUALITY, FITNESS FOR A PARTICULAR PURPOSE, USABILITY,

INTEGRATION OR NON-INFRINGEMENT AND ALL SUCH WARRANTIES ARE HEREBY EXCLUDED BY WILEY AND ITS LICENSORS AND WAIVED BY YOU.

- WILEY shall have the right to terminate this Agreement immediately upon breach of this Agreement by you.

- You shall indemnify, defend and hold harmless WILEY, its Licensors and their respective directors, officers, agents and employees, from and against any actual or threatened claims, demands, causes of action or proceedings arising from any breach of this Agreement by you.

- IN NO EVENT SHALL WILEY OR ITS LICENSORS BE LIABLE TO YOU OR ANY OTHER PARTY OR ANY OTHER PERSON OR ENTITY FOR ANY SPECIAL, CONSEQUENTIAL, INCIDENTAL, INDIRECT, EXEMPLARY OR PUNITIVE DAMAGES, HOWEVER CAUSED, ARISING OUT OF OR IN CONNECTION WITH THE DOWNLOADING, PROVISIONING, VIEWING OR USE OF THE MATERIALS REGARDLESS OF THE FORM OF ACTION, WHETHER FOR BREACH OF CONTRACT, BREACH OF WARRANTY, TORT, NEGLIGENCE, INFRINGEMENT OR OTHERWISE (INCLUDING, WITHOUT LIMITATION, DAMAGES BASED ON LOSS OF PROFITS, DATA, FILES, USE, BUSINESS OPPORTUNITY OR CLAIMS OF THIRD PARTIES), AND WHETHER OR NOT THE PARTY HAS BEEN ADVISED OF THE POSSIBILITY OF SUCH DAMAGES. THIS LIMITATION SHALL APPLY NOTWITHSTANDING ANY FAILURE OF ESSENTIAL PURPOSE OF ANY LIMITED REMEDY PROVIDED HEREIN.

- Should any provision of this Agreement be held by a court of competent jurisdiction to be illegal, invalid,

or unenforceable, that provision shall be deemed amended to achieve as nearly as possible the same economic effect as the original provision, and the legality, validity and enforceability of the remaining provisions of this Agreement shall not be affected or impaired thereby.

- The failure of either party to enforce any term or condition of this Agreement shall not constitute a waiver of either party's right to enforce each and every term and condition of this Agreement. No breach under this agreement shall be deemed waived or excused by either party unless such waiver or consent is in writing signed by the party granting such waiver or consent. The waiver by or consent of a party to a breach of any provision of this Agreement shall not operate or be construed as a waiver of or consent to any other or subsequent breach by such other party.

- This Agreement may not be assigned (including by operation of law or otherwise) by you without WILEY's prior written consent.

- Any fee required for this permission shall be non-refundable after thirty (30) days from receipt by the CCC.

- These terms and conditions together with CCC's Billing and Payment terms and conditions (which are incorporated herein) form the entire agreement between you and WILEY concerning this licensing transaction and (in the absence of fraud) supersedes all prior agreements and representations of the parties, oral or written. This Agreement may not be amended except in writing signed by both parties. This Agreement shall be binding upon and inure to the benefit of the parties' successors, legal representatives, and authorized assigns.

- In the event of any conflict between your obligations established by these terms and conditions and those

established by CCC's Billing and Payment terms and conditions, these terms and conditions shall prevail.

- WILEY expressly reserves all rights not specifically granted in the combination of (i) the license details provided by you and accepted in the course of this licensing transaction, (ii) these terms and conditions and (iii) CCC's Billing and Payment terms and conditions.

- This Agreement will be void if the Type of Use, Format, Circulation, or Requestor Type was misrepresented during the licensing process.

- This Agreement shall be governed by and construed in accordance with the laws of the State of New York, USA, without regards to such state's conflict of law rules. Any legal action, suit or proceeding arising out of or relating to these Terms and Conditions or the breach thereof shall be instituted in a court of competent jurisdiction in New York County in the State of New York in the United States of America and each party hereby consents and submits to the personal jurisdiction of such court, waives any objection to venue in such court and consents to service of process by registered or certified mail, return receipt requested, at the last known address of such party.

WILEY OPEN ACCESS TERMS AND CONDITIONS

Wiley Publishes Open Access Articles in fully Open Access Journals and in Subscription journals offering Online Open. Although most of the fully Open Access journals publish open access articles under the terms of the Creative Commons Attribution (CC BY) License only, the subscription journals and a few of the Open Access Journals offer a choice of Creative Commons Licenses. The license type is clearly identified on the article.

The Creative Commons Attribution License

The Creative Commons Attribution License (CC-BY) allows users to copy, distribute and transmit an article, adapt the article and make commercial use of the article. The CC-BY license permits commercial and non-

AIP PUBLISHING LLC LICENSE
TERMS AND CONDITIONS
Nov 19, 2016

This Agreement between Melissa B Gordon ("You") and AIP Publishing LLC ("AIP Publishing LLC") consists of your license details and the terms and conditions provided by AIP Publishing LLC and Copyright Clearance Center.

License Number
3992650546084
License date
Nov 19, 2016
Licensed Content Publisher
AIP Publishing LLC
Licensed Content Publication
Journal of Rheology
Licensed Content Title
The rheology and microstructure of an aging thermoreversible colloidal gel
Licensed Content Author
Melissa B. Gordon,Christopher J. Kloxin,Norman J. Wagner
Licensed Content Date
Nov 11, 2016
Licensed Content Volume Number
61
Licensed Content Issue Number
1
Type of Use
Thesis/Dissertation
Requestor type
Author (original article)
Format
Print and electronic
Portion
Excerpt (> 800 words)
Will you be translating?
No
Title of your thesis / dissertation
The Development and Characterization of Stimuli-Responsive Systems for Performance Materials
Expected completion date
Dec 2016
Estimated size (number of pages)
200
Requestor Location
Melissa B Gordon
150 Academy Street

NEWARK, DE 19716
United States
Attn: Melissa B Gordon

Billing Type
Invoice
Billing Address
Melissa B Gordon
150 Academy Street

NEWARK, DE 19716
United States
Attn: Melissa B Gordon
Total
0.00 USD
Terms and Conditions
The Society of Rheology -- Terms and Conditions: Permissions Uses

The Society of Rheology ("SOR") hereby grants to you the non-exclusive right and license to use and/or distribute the Material according to the use specified in your order, on a one-time basis, for the specified term, with a maximum distribution equal to the number that you have ordered. Any links or other content accompanying the Material are not the subject of this license.

1. You agree to include the following copyright and permission notice with the reproduction of the Material:"Reprinted with permission from [FULL CITATION]. Copyright [PUBLICATION YEAR], The Society of Rheology." For an article, the copyright and permission notice must be printed on the first page of the article or book chapter. For photographs, covers, or tables, the copyright and permission notice may appear with the Material, in a footnote, or in the reference list.
2. If you have licensed reuse of a figure, photograph, cover, or table, it is your responsibility to ensure that the material is original to SOR and does not contain the copyright of another entity, and that the copyright notice of the figure, photograph, cover, or table does not indicate that it was reprinted by SOR, with permission, from another source. Under no circumstances does SOR, purport or intend to grant permission to reuse material to which it does not hold copyright.
3. You may not alter or modify the Material in any manner. You may translate the Material into another language only if you have licensed translation rights. You may not use the Material for promotional purposes. SOR reserves all rights not specifically granted herein.
4. The foregoing license shall not take effect unless and until SOR or its agent, Copyright Clearance Center, receives the Payment in accordance with Copyright Clearance Center Billing and Payment Terms and Conditions, which are incorporated herein by reference.
5. SOR or the Copyright Clearance Center may, within two business days of granting this license, revoke the license for any reason whatsoever, with a full refund payable to you. Should you violate the terms of this license at any time, SOR, The Society of Rheology, or Copyright Clearance Center may revoke the license with no refund to you. Notice of such revocation will be made using the contact information provided by you. Failure to receive such notice will not nullify the revocation.
6. SOR makes no representations or warranties with respect to the Material. You agree to indemnify and hold harmless SOR, The Society of Rheology, and their officers, directors, employees or agents from and against any and all claims arising out of your use of the Material other than as specifically authorized herein.
7. The permission granted herein is personal to you and is not transferable or assignable without the prior written permission of SOR. This license may not be amended except in a writing signed by the party to be charged.

8. If purchase orders, acknowledgments or check endorsements are issued on any forms containing terms and conditions which are inconsistent with these provisions, such inconsistent terms and conditions shall be of no force and effect. This document, including the CCC Billing and Payment Terms and Conditions, shall be the entire agreement between the parties relating to the subject matter hereof.

This Agreement shall be governed by and construed in accordance with the laws of the State of New York. Both parties hereby submit to the jurisdiction of the courts of New York County for purposes of resolving any disputes that may arise hereunder.
Questions? customercare@copyright.com or +1-855-239-3415 (toll free in the US) or +1-978-646-2777.

Title: Dynamical Arrest, Percolation, Gelation, and Glass Formation in Model Nanoparticle Dispersions with Thermoreversible Adhesive Interactions

Author: Aaron P. R. Eberle, Ramón Castañeda-Priego, Jung M. Kim, et al

Publication: Langmuir

Publisher: American Chemical Society

Date: Jan 1, 2012

PERMISSION/LICENSE IS GRANTED FOR YOUR ORDER AT NO CHARGE

This type of permission/license, instead of the standard Terms & Conditions, is sent to you because no fee is being charged for your order. Please note the following:

- Permission is granted for your request in both print and electronic formats, and translations.
- If figures and/or tables were requested, they may be adapted or used in part.
- Please print this page for your records and send a copy of it to your publisher/graduate school.
- Appropriate credit for the requested material should be given as follows: "Reprinted (adapted) with permission from (COMPLETE REFERENCE CITATION). Copyright (YEAR) American Chemical Society." Insert appropriate information in place of the capitalized words.

- One-time permission is granted only for the use specified in your request. No additional uses are granted (such as derivative works or other editions). For any other uses, please submit a new request.

If credit is given to another source for the material you requested, permission must be obtained from that source.

(such as derivative works or other editions). For any other uses, please submit a new request.

If credit is given to another source for the material you requested, permission must be obtained from that source.